TECHNICAL MEMORANDUM

X- 73

EFFECTS OF VARIATION IN BODY ORIENTATION AND WING AND

BODY GEOMETRY ON LIFT-DRAG CHARACTERISTICS OF

A SERIES OF WING-BODY COMBINATIONS

AT MACH NUMBERS FROM 3 TO 18

By William O. Armstrong and Charles L. Ladson

Langley Research Center
Langley Field, Va.

NATIONAL AERONAUTICS AND SPACE ADMINISTRATION

WASHINGTON   October 1959

UNCLASSIFIED

NATIONAL AERONAUTICS AND SPACE ADMINISTRATION

TECHNICAL MEMORANDUM X-73

EFFECTS OF VARIATION IN BODY ORIENTATION AND WING AND

BODY GEOMETRY ON LIFT-DRAG CHARACTERISTICS OF

A SERIES OF WING-BODY COMBINATIONS

AT MACH NUMBERS FROM 3 TO 18[*]

By William O. Armstrong and Charles L. Ladson

SUMMARY

An investigation was made in the Langley 11-inch hypersonic tunnel to study the effects of body orientation and variation in model geometry on the lift-drag characteristics of several generalized configurations at hypersonic speeds. Tests were conducted at Mach numbers of 6.86 and 9.6 in air and 10.5, 13.0, and 17.8 in helium. Some additional data were obtained in the Langley 9-inch supersonic tunnel at a Mach number of 2.91. Three-component force and moment data were obtained for angles of attack from $-3°$ to $16°$ at several Reynolds numbers. The extent to which some of these results may be predicted by use of several existing theories was assessed.

The results of this investigation indicate that reasonable predictions of the lift-drag characteristics of wing-body combinations at hypersonic speeds can be made by use of some theoretical methods. It was also shown that while the lift-drag ratio of many wing-body combinations can be improved at supersonic speeds by use of the flat-top configuration, this advantage rapidly diminishes with increasing Mach number and is virtually nonexistent at Mach numbers greater than about 10. Changes in wing and body geometry resulted in substantial variations in maximum lift-drag ratio.

INTRODUCTION

Considerable emphasis has been placed upon the determination of the feasibility of operating hypersonic vehicles over intercontinental and

global ranges. While the lift-drag ratio L/D has little significance in flight efficiency for the global mission, it is of major concern for the intermediate ranges, and the highest L/D consistent with reasonable structural weight is desirable. Some results of an investigation to determine the effect of L/D on range are presented in references 1 and 2. A number of studies have indicated that configurations which utilize body interference are capable of attaining high lift-drag ratios at supersonic speeds. (See refs. 3 to 7.) Experimental data on these configurations are available at Mach numbers up to about 6 (refs. 4 and 6). However, only limited information (e.g., ref. 8) is available for comparison of the lift-drag characteristics of flat-top vehicles (body beneath the wing) with those of different geometric designs such as midwing and flat-bottom configurations (body above the wing). At higher Mach numbers it would be anticipated that the advantage of the flat-top vehicle would decrease or even disappear as a result of the reduction of the beneficial body interference.

Additional studies were needed to investigate the effects of body orientation and variation in model geometry in the higher hypersonic speed range. Consequently an investigation was undertaken to study the performance characteristics of several generalized configurations at hypersonic speeds, with emphasis given to the effects of geometric variables. This investigation was carried out in the Langley 11-inch hypersonic tunnel at Mach numbers of 6.86 and 9.6 in air and 10.5, 13.0, and 17.8 in helium and in the Langley 9-inch supersonic tunnel at a Mach number of 2.91 in air. The extent to which some of these results may be predicted by use of several existing theoretical approaches has also been assessed.

The design and calibration of the helium nozzles are also included in this paper as an appendix by Donald L. Baradell and Thomas A. Blackstock.

L
2
4
7

SYMBOLS

Lift, drag, and pitching moment were referred to the body-axis system. The reference center of moments was located at $0.50\bar{c}$.

C_A axial-force coefficient

C_D drag coefficient

$C_{D,i}$ coefficient of drag due to lift

C_f skin-friction coefficient

C_L lift coefficient

C_{L_α} lift-curve slope

$C_{L,\alpha=0}$ lift coefficient at zero angle of attack

C_m pitching-moment coefficient about $0.50\bar{c}$

C_N normal-force coefficient

C_p pressure coefficient

$\bar{c}$ mean aerodynamic chord, in.

D diameter, in.

l body length, in.

M Mach number

p_t stagnation pressure in settling chamber, lb/sq in. abs

p_t' stagnation pressure behind a normal shock, lb/sq in. abs

r body radial ordinate, in.

R Reynolds number based on wing root chord

S total plan-form area of model, sq in.

x longitudinal station measured from fuselage vertex, in.

L/D lift-drag ratio, C_L/C_D

α angle of attack with reference to flat wing surface, deg

α_e effective angle of attack $\left(\alpha_e = 0 \text{ at } C_L = 0\right)$, deg

γ ratio of specific heats

δ_c body semiapex angle, deg

ϵ	wing semivertex angle, deg
Λ	wing leading-edge sweep angle, deg
θ_F	wingtip-flap deflection angle, deg

Subscripts:

b	body base
le	leading edge
max	maximum
∞	free stream

MODELS

Three-view drawings showing the dimensions of the various wing-body configurations are presented in figure 1. The wing sweep, wingtip deflection, body length, mean aerodynamic chord, and wing area are also tabulated in this figure. Photographs of the various models are shown in figure 2. The letter "a" after a model number refers to the flat-top configuration, while the letter "b" denotes the flat-bottom configuration.

Models 1, 3, and 5 incorporated a body with radius $r = r_b(x/l)^{3/4}$ and the wing shown in figure 1(a). The wing was formed from a simple wedge section with a wedge angle of 4.6° normal to the leading edge. The body was cut 1° above its axis and the wing was attached to the flat upper surface so formed. Wingtip droop was obtained by deflecting the wingtip about a line canted 3° from the streamwise direction. Slab flaps fixed at zero deflection were also incorporated in the models.

Models 2, 4, and 6 utilized the same wing plan form but incorporated a symmetrical body of revolution that had the same longitudinal distribution of cross-sectional area as the body used on models 1, 3, and 5; hence models 1 to 6 all had the same body volume. The ordinates for this body are given in table I.

Models 7 to 11, shown in figure 1(b), consisted of a semiconic body used in conjunction with a series of delta wings of varying leading-edge sweep. The body was constructed from a cone with a 5° semiapex angle, cut in a manner similar to that of the body used for models 1, 3, and 5. The wings were simple wedge-slab sections with a wedge angle of 4.5° normal to the leading edge.

Model 12, also shown in figure 1(b), was similar in design to models 7 to 11, except that the body semiapex angle was increased to 7.5°.

Model 13, shown in figure 1(c), was similar to model 10 except that the wing was changed to an arrow plan form with a wing sweep angle of 77.5°.

Model 14, also shown in figure 1(c), incorporated a semicone-cylinder body with a 5° semiapex angle and a delta wing with a leading-edge sweep angle of 77.5°. This model also had the semicone center line offset 1° from the adjacent wing section. The conic and cylindrical portions of the body were equal in length. When the wing tips of this model were clipped in a streamwise direction as shown on the model sketch, the resulting model was designated as model 15.

All wings had cylindrical leading edges with 0.002-inch radius. The wing surface adjacent to the body was flat for all models, and this surface was alined with the stream at an angle of attack of 0°. The noses of models 1 to 6 were blunted to a nose diameter of 0.040 inch. Half-scale models of configurations 1-a and 1-b were used in helium tests at $M = 13$.

APPARATUS, TESTS, AND PROCEDURES

Tests were conducted in the Langley 11-inch hypersonic tunnel at Mach numbers of 6.86 and 9.6 in air and 10.5, 13.0, and 17.8 in helium. Typical model installations may be seen in the schlieren photographs of figure 3. The design and calibration of the three helium nozzles are presented in appendix A. As shown in this appendix, uniform flow existed in the test region for both the $M = 10.5$ and 18.0 nozzles. However, the flow in the $M = 13.0$ nozzle was of considerably poorer quality. A flow angularity of about 2° was found to exist in the test region. Although this flow angularity might affect the lift at an angle of attack, it is believed that it would not have an appreciable effect on $(L/D)_{max}$ and C_{L_α}.

Lift, drag, and pitching moment were obtained with three-component external strain-gage balances attached to the model base. Additional lift and drag data at a Mach number of 2.91 were measured in the Langley 9-inch supersonic tunnel by use of a mechanical external balance.

In both tunnels the angles of attack of the models were measured optically by use of a light beam reflected from the model onto a calibrated scale. This method gives the true angles of attack of the model irrespective of the deflection of the balance and sting under load.

Tests were made at several Reynolds numbers by varying the tunnel operating stagnation pressure. The Reynolds number was calculated on the basis of the wing root chord. Base pressure was measured for all tests, and axial force was adjusted to a condition where base presssure was equal to free-stream static pressure.

Schlieren photographs of the flow pattern were taken during each test run. Several representative schlieren photographs are shown in figure 3. Leakage of helium from the tunnel into the path of the schlieren beam caused the distortions in figure 3(a) of the helium tests at a Mach number of 10.5.

Since the usable test-section area of the $M = 13$ helium nozzle was smaller than that of the other nozzles used, half-scale models of configuration 1-a and 1-b were used for the $M = 13$ tests.

ACCURACY OF DATA

For data from either tunnel, the maximum probable errors in the individual test points due to the force balance system and variations in the dynamic pressure and angle of attack did not exceed the following:

c_N . . . . ±0.0070

c_A . . . . ±0.0012

c_L . . . . ±0.0080

c_D . . . . ±0.0020

c_m . . . . ±0.0050

However, repeatability of the test data indicates that the errors in the force coefficients were never this great.

The errors in the angles of attack were never greater than ±0.10°. Mach number was determined to an accuracy of ±0.01 for the tests in air. For all the helium tests the Mach number at the test-section center line was determined to within ±0.3. The Reynolds number was maintained within ±0.07 × 10^6 of the nominal values.

PRESENTATION OF RESULTS

An analysis of the results of this investigation is presented in figures 4 to 16 in the following order:

Investigation	Model	Mach number	Reynolds number	Figure
Comparison of theoretical and experimental force coefficients	9, 13	6.86, 9.6	0.36×10^6 to 3.0×10^6	4 to 7
Reynolds number effects	1, 2, 13	6.86	0.36×10^6 to 3.0×10^6	8
Effects of Mach number and body orientation	1 to 6, 10, 13, 14	3 to 18	Various	9 to 13
Effects of leading-edge sweep	7 to 11	6.86	1.3×10^6	14, 15
Effects of wingtip deflection	1 to 6	6.86	0.7×10^6 and 2.1×10^6	16(a)
Effects of model geometry	9, 10, 12, 14, 15	6.86	1.3×10^6	16(b)

The basic data obtained on all the configurations are shown in figures 17 to 26 as plots of C_L, C_D, C_m, and L/D against angle of attack at the various Mach numbers and Reynolds numbers. The data are presented in the following order:

Gas	Model	Mach number	Reynolds number	Figure
Air	13	2.91	0.7×10^6	17(a)
	→	→	5.6	17(b)
	1	6.86	.36	18(a)
	→		.7	18(b)
	→		1.4	18(c)
	→		2.1	18(d)
	→		2.6	18(e)
	2		.36	19(a)
	→		.7	19(b)
	→		1.4	19(c)
	→		2.1	19(d)
	→		2.6	19(e)
	3		.7 →	20(a)
	4			20(b)
	5			20(c)
	6		2.1 →	20(d)
	3			21(a)
	4			21(b)
	5		.36 →	21(c)
	6			21(d)
	9		1.3	22
	7			23(a)
	8			23(b)
	9		.36	23(c)
	10			23(d)
	11			23(e)
	12			23(f)
	14			23(g)
	15			23(h)
	13	9.6 →	.36	24(a)
	→		.7	24(b)
	→		1.4	24(c)
	1	10.5	2.2	24(d)
	9	13.0	3.0	24(e)
	13	17.8	.7 →	25(a)
				25(b)
				25(c)
Helium	1 →		1.6	26(a)
	→		2.8	26(b)
	→		3.4	26(c)

8

L
2
4
7

DISCUSSION

While a detailed analysis of the lift-drag characteristics of the models is presented, no analysis of the longitudinal-stability characteristics is included in this paper. The curves for the variation of C_m with angle of attack show that models 1 to 6 were longitudinally unstable while models 7 to 15 had neutral stability about a moment reference center located at $0.50\bar{c}$. The static margin in models 1 to 6 varied from about $0.20\bar{c}$ to about $0.29\bar{c}$.

Comparison of Theoretical and Experimental

Force Coefficients

Theoretical methods.- An effort has been made to determine the capability of several theoretical methods of predicting the aerodynamic forces on flat-top and flat-bottom wing-body combinations at supersonic and hypersonic speeds. Theoretical estimates made by these methods were compared with experimental results for model 13 (a semicone with arrow wing) and model 9 (a semicone with delta wing) at Mach numbers of 6.86 and 9.6. The methods used were:

(1) Local flow

(2) Modified local flow

(3) Method of Savin (ref. 7)

(4) Modified Newtonian

(5) Newtonian-shock expansion

Although it was recognized that the theories utilizing the Newtonian concept were based on an overly simplified flow-field pattern, these theories were included because they are generally recognized approaches for calculating integrated forces at hypersonic speeds and offer a relatively simple means of estimating the longitudinal characteristics of these configurations.

A more detailed description of the assumptions and methods of calculation is presented in appendix B.

Normal force.- The normal-force coefficients obtained by these various methods are presented, along with experimental values, as a function of angle of attack in figure 4.

From this figure it can be seen that modified local-flow theory gives good agreement with the experimental data for both the arrow-wing and delta-wing configurations throughout the angle-of-attack range of the investigation at Mach numbers of 6.86 and 9.6. Since Newtonian-shock-expansion theory neglects the interference effects of the body and under-estimates the pressures on the slender body, this theory underpredicts the slope of the normal-force curve. As seen from figure 4, this theory shows poor agreement with experimental data for the flat-top orientation. For the flat-bottom orientation at the higher angles of attack, where the body and its region of influence is negligible, this theory gives very good agreement with experiment.

The method of reference 7 gives reasonable estimates of the magnitude of C_N for the arrow-wing configuration at a Mach number of 6.86 (the only combination of Mach number and geometry for which this method is applicable) but underestimates the slope of the normal-force curve. Modified Newtonian theory gives poor results for both the flat-top and flat-bottom orientations because the pressures on the wing were under-predicted as a result of the use of the normal-shock relations to determine $C_{p,max}$. For application to wings in this angle-of-attack range, the relation $C_p = (\gamma + 1)\sin^2\delta$ should be used. (See ref. 9.) Results obtained from this relation for the wing contribution agree closely with results obtained from the oblique-shock relations, as in the Newtonian-shock-expansion method, and therefore are not presented.

Axial force.- The theories that were used to predict the normal-force coefficient were also used to predict the inviscid axial-force coefficients. Calculations of skin friction were needed for the determination of total axial force and were computed with the assumption of a laminar boundary layer. The laminar skin-friction coefficient was calculated by use of the T' method described in reference 10 and corrected for effects of boundary-layer displacement by the method of reference 11. Flow characteristics used for evaluating the skin-friction coefficient were determined by use of the local flow theory. Flow characteristics evaluated by the theories utilizing the Newtonian concept would result in somewhat lower Reynolds numbers on the under surface of the flat-top configuration since the interference effects would be neglected. However, a qualitative assessment of this approach indicated that these theories would give only slightly higher estimates of the skin friction than the local-flow theory. In the case of the flat-bottom configuration, where the body is shielded from flow, the interference effects of the body are very small and the difference in the estimates of skin friction would be negligible.

Since the leading edges of the wings were blunted to a cylindrical edge of 0.002-inch radius, it was also necessary to obtain the

leading-edge drag. This was accomplished by determining the appropriate cross-flow Mach number at the leading edge and obtaining the corresponding drag coefficient from the data of reference 12. The leading-edge axial forces thus obtained were of negligible magnitude $(C_{A,le} = 0.0001)$ and did not significantly alter the axial-force coefficients of the configuration. Base pressures were assumed equal to free-stream static pressure to permit comparison of the calculated axial-force coefficients with the measured axial-force coefficients which were corrected to free-stream conditions.

The axial-force coefficients obtained by use of the various theories are presented, together with experimental results, as a function of angle of attack for several Reynolds numbers in figure 5. While some differences between predicted and measured axial-force coefficients are indicated, these are believed to be largely the result of the scatter in experimental data, the assumption of inviscid flow conditions, and the neglect of the effect of boundary-layer displacement on the predicted pressure distribution at the low Reynolds number conditions. In addition to these factors, underpredictions of axial-force coefficients would be expected at the higher Reynolds numbers since laminar flow conditions were assumed for these calculations and at these higher Reynolds numbers the flow is partially or fully turbulent. These underpredictions at the higher Reynolds numbers are apparent in figure 5. It should also be pointed out that both the modified Newtonian theory and the Newtonian-shock-expansion theory give about the same estimate of axial-force coefficient, since the wing contributes a small axial pressure force and the body contribution to axial pressure force was calculated in the same manner for both theories. The axial-force coefficient increases more rapidly with increasing angle of attack for the flat-top orientation than for the flat-bottom orientation.

In general, for the angle-of-attack range considered, better predictions of C_A were obtained for the flat-bottom configurations by using the Newtonian-shock-expansion theory and for the flat-top configurations by using local-flow theory. However, for the delta-wing model (model 9), axial force was predicted more accurately by Newtonian-shock-expansion theory for the flat-top orientation at angles of attack greater than $3°$.

Lift-drag ratio.- Since this investigation was principally concerned with determination of the lift-drag ratios of the various configurations, a comparison of experimental and theoretical results for the lower Reynolds numbers is presented in figure 6 as a function of angle of attack. This comparison was made for both the arrow- and delta-wing models at Mach numbers of 6.86 and 9.6. Since the best agreement between experimental data and theoretical calculations was obtained by use of the modified local-flow and Newtonian-shock-expansion

theories, these were the only theories used for estimating the lift-drag ratio. Figure 6 indicates that reasonable predictions of lift-drag ratio could be made by means of these two theories throughout the angle-of-attack range of the investigation for both models at both Mach numbers. At the higher Reynolds numbers, where turbulent flow conditions exist, the ability to make reasonably accurate predictions of L/D depends upon the accuracy with which the skin friction can be estimated.

Although reasonable estimates of the lift-drag ratios could be made throughout the angle-of-attack range, the estimates were not accurate enough to predict the effects of body orientation on maximum lift-drag ratios. Figure 6 shows that both theories predict higher values of $(L/D)_{max}$ for the flat-bottom orientation than for the flat-top orientation. Experimental results show that the opposite is true at a Mach number of 6.86 and that no appreciable difference exists at a Mach number of 9.6.

Reynolds Number Effects

As mentioned in the discussion of figure 5, the axial-force coefficient was underpredicted at higher Reynolds numbers because the boundary-layer transition occurred farther forward on the model, which subjected a larger area to a turbulent boundary layer with increased skin friction. Experimental axial-force coefficients for the arrow-wing configuration are presented as a function of Reynolds number in figure 7 and are compared with theoretical estimates based on the assumption of a fully laminar boundary layer. The angles of attack shown in the figure (other than zero) represent the approximate angles for $(L/D)_{max}$ for both the flat-top and flat-bottom orientations. From this figure it appears that laminar flow conditions prevailed up to a Reynolds number of about 0.7×10^6, and above this value there was a rapid forward movement of the point of transition with increase in Reynolds number.

In figure 4(a), there is a noticeable increase in the value of C_N as the Reynolds number is increased from 0.36×10^6 to 3.0×10^6. This variation is more clearly shown in figures 8(a) and 8(c), which present experimental values of C_{L_α} at $\alpha = 0^\circ$ as a function of Reynolds number at a Mach number of 6.86 for several wing-body configurations. The lift-curve slope shows a slight increase with increasing Reynolds number in the lower range, but at the higher Reynolds numbers it remains more nearly constant. This same trend is evident at all angles of attack up to that for $(L/D)_{max}$. Comparison of experimental data with that determined by use of local-flow theory showed that C_{L_α} could be predicted

fairly accurately by this theory over a wide Reynolds number range (fig. 8(c)).

The variation in $(L/D)_{max}$ with Reynolds number for several body orientations is shown in figures 8(b) and 8(d). In general, $(L/D)_{max}$ increased with increasing Reynolds number for all the configurations; however this increase was most pronounced in the lower Reynolds number range. The flat-top orientation showed a somewhat higher $(L/D)_{max}$ than the flat-bottom orientation throughout the Reynolds number range of the investigation. Figure 8(b) shows that the midwing orientation had a slightly higher $(L/D)_{max}$ than the flat-top case only at the lowest Reynolds numbers.

L
2
4
7

<center>Effects of Mach Number and Body Orientation</center>

Maximum lift-drag ratios for both the flat-top and flat-bottom orientations of model 1 (clipped arrow wing and 3/4-power body) and model 13 (arrow wing and semicone body) are presented in figure 9 as a function of Mach number. These data were obtained from tests in air at Mach numbers of 6.86 and 9.6 and in helium at Mach numbers of 10.5, 13.0, and 17.8. Also included are data for a similar model obtained from reference 6. At a Mach number of 6.86 the flat-top orientation had the highest $(L/D)_{max}$, but at Mach numbers of 9.6 and greater the values of $(L/D)_{max}$ were the same (within experimental accuracy) for both body orientations. The higher values of $(L/D)_{max}$ at Mach numbers of 10.5, 13.0, and 17.8 (as compared with the values at $M = 9.6$) were the result of the higher Reynolds numbers, and consequently, lower skin friction. Figure 9(b) presents results for model 13 at several Mach numbers. Results presented in reference 4 for a model of similar design are also included. This figure also shows that the effects of body orientation diminished with increasing Mach number and became almost negligible at Mach numbers above 9.6.

The results of an investigation which evaluated the effects of body orientation on $(L/D)_{max}$ for a similar wing-body combination at supersonic and hypersonic speeds are presented in reference 8. Data from this reference obtained by using the hypersonic similarity rule and corrected to flight conditions also showed that the difference in $(L/D)_{max}$ due to body orientation decreased with increasing hypersonic speed. However, the results obtained in the present investigation indicate that this difference in $(L/D)_{max}$ for different body orientations diminishes more rapidly with increasing hypersonic speed than was indicated by the data for a similar model presented in reference 8.

Predictions of $(L/D)_{max}$ based on the modified local-flow theory for model 13 are presented in figure 9(b) for the higher Mach number range. This figure shows reasonable agreement between predicted and experimental values of $(L/D)_{max}$. However, the variation in $(L/D)_{max}$ due to body orientation was not accurately assessed since the theory predicts a higher $(L/D)_{max}$ for the flat-bottom orientation in the lower hypersonic speed range, whereas experimental data show a higher $(L/D)_{max}$ for the flat-top configuration. Since it has been shown in figure 6 that Newtonian-shock-expansion theory best predicts the characteristics of the flat-bottom configuration at angles of attack near $(L/D)_{max}$, this theory is also presented for comparison purposes in figure 9(b) for the flat-bottom case. From the experimental data shown in figure 9 it can be surmised that the flat-top orientation has the highest $(L/D)_{max}$ at supersonic and low hypersonic Mach numbers. However, both experiment and theory show that the variation in $(L/D)_{max}$ due to body orientation diminished with increasing Mach number and became negligible at Mach numbers above about 10.

Examination of the basic data showed that the maximum lift-drag ratio occurred at very nearly the same lift coefficient, though not the same angle of attack, for both the flat-top and flat-bottom orientations. The minimum-drag coefficient was the same for both body orientations, since the flat-top is simply the flat-bottom configuration rolled 180°. Since the lift coefficient for $(L/D)_{max}$ and the minimum-drag coefficient were the same for both configurations, any difference in $(L/D)_{max}$ between the flat-top and flat-bottom orientation results from a difference in the drag due to lift of the two.

Figure 10 presents the variation in the drag-due-to-lift parameter $C_{D,i}/C_L^2$ with Mach number at approximately the lift coefficient for $(L/D)_{max}$ for the two configurations discussed in figure 9. It may be seen that the flat-bottom configuration had higher drag due to lift than the flat-top configuration at the lower Mach numbers, but this difference decreased with increasing Mach number. This result explains the trends in $(L/D)_{max}$ with Mach number observed in figure 9.

To determine the accuracy with which the drag due to lift $C_{D,i}$ may be predicted, faired experimental results are compared in figure 11 with theoretical predictions obtained by assuming $C_{D,i} = C_L \tan \alpha_e$ where $\alpha_e = \alpha - (\alpha)_{C_L=0}$. Although this simplified approach ignores the variation in C_A with angle of attack, good agreement is shown in this

figure between experimental and estimated values of drag due to lift. No difference is seen in the drag due to lift for the flat-top and flat-bottom orientation as calculated by the modified local-flow theory, since C_{L_α} is essentially constant with angle of attack through the range of lift coefficients presented. These results indicated that fairly accurate predictions of the total-drag coefficient can be made if the minimum drag and the lift coefficient are reasonably predicted.

Figure 12 presents the experimental variation of lift-curve slope at $\alpha = 0^\circ$ with Mach number for the same configurations (models 1 and 13). It should be noted that C_{L_α} generally decreases with increasing Mach number, approximately as expected from inviscid flat-plate theory, up to a Mach number of about 13. However, between Mach numbers of 13 and 18 (fig. 12(a)), the experimental value of C_{L_α} decreases less rapidly than predicted because of the increasing influence of boundary-layer displacement which tends to increase the lift-curve slope. (See refs. 13 and 14.) Because of the thickness effects of the configuration, the experimental lift-curve slopes are somewhat higher than those predicted by the flat-plate theory. The value of C_{L_α} obtained by the local-flow theory compares quite well with experimental data for model 13 (fig. 12(b)).

The effects of body orientation on $(L/D)_{max}$ and C_{L_α} for several configurations are presented in figure 13 for a Mach number of 6.86 and Reynolds numbers of 0.7×10^6 and 2.1×10^6. As previously mentioned in the discussion of figure 8, some variation in the magnitude of $(L/D)_{max}$ was noted with changing Reynolds number; however, in general, the variations in $(L/D)_{max}$ resulting from changes in body orientation were similar for the different Reynolds numbers. It is evident from the results presented in figure 13 that for all the configurations shown the flat-top orientation had a higher value of $(L/D)_{max}$ than the flat-bottom orientation. Also, except for the flat-top configuration with an upward deflection of the wingtips (model 5-a), the values of $(L/D)_{max}$ for the flat-top and midwing orientations were essentially the same (within 0.1). Data presented in reference 8 for a configuration with conic body and arrow wing at a Mach number of 8.0 show the difference in $(L/D)_{max}$ between the flat-top and midwing configurations to be somewhat greater than indicated in the present investigation.

Effects of Leading-Edge Sweep

In an effort to evaluate the effect of wing sweep on the longitudinal characteristics of the flat-top and flat-bottom configurations, a series of models having a conic body with a 5° semiapex angle and a delta wing were tested at a Mach number of 6.86 for several sweep angles (models 7 to 11). Sweep angles were chosen to vary from that of a wing with the leading edge just behind the theoretical cone shock wave (model 11) to that of a wing with a leading edge well ahead of this conic shock (model 7). Figure 14(a) shows that the absolute value of C_L at $\alpha = 0^{\circ}$ was reduced with decreasing sweep until $C_L = 0$ at a sweep angle of 60°. From figure 1(b) it can be seen that reducing wing sweep reduces the ratio of body volume to wing area and increases the streamwise wedge angle of the upper surface of the wing. Therefore, as wing sweep was reduced, the contribution of the body to lift, in comparison with that of the wing, was reduced and the wedge effectiveness was increased, and tended to offset the lift of the body. These results would be somewhat altered, however, if an angle-of-attack reference plane other than the wing surface adjacent to the body had been chosen.

Comparison of the experimental lift coefficient at $\alpha = 0^{\circ}$ with that predicted by local-flow theory showed that this theory predicted the lift characteristics fairly well (fig. 14(a)) since the flow conditions are fairly well defined. However, at angles of attack the flow conditions are not as well defined and, as shown by the plot of lift-curve slope in figure 14(b), the theory was not as effective for predicting the lift characteristics at angle of attack. As previously shown in figure 12(a), use of inviscid flat-plate theory gave a lift-curve slope of approximately 0.01 at a Mach number of 6.86. This flat-plate approximation, as expected, was somewhat lower than that shown for the configurations presented in figure 14(b); however, for the configuration with the lowest wing sweep ($\Lambda = 60^{\circ}$) where the body volume was relatively small compared with the wing area, the increment in C_{L_α} above that predicted by flat-plate theory can be largely accounted for by the effect of the wing wedge on lift-curve slope. Although an increase in wing sweep reduced the streamwise wedge angle, and hence the wedge effect on lift-curve slope, the ratio of body to wing area increased. The increase in body effect on C_{L_α} more than offsets the loss caused by reduced wedge effectiveness, as shown by the general increase in the calculated lift-curve slope with increasing sweep angle (fig. 14(b)). This predicted increase in C_{L_α} did not materialize experimentally, however, and at the higher sweep angles ($\Lambda = 81^{\circ}$) the measured lift-curve slope was only slightly higher than that given by inviscid flat-plate theory in figure 12(a).

DECLASSIFIED

In figure 14(c) the variation of $(L/D)_{max}$ with leading-edge sweep is shown. The maximum values and maximum difference in the curves occurs at a wing sweep of about 67°, where the value of $(L/D)_{max}$ is approximately 15 percent greater for the flat-top orientation than for the flat-bottom orientation. However, the effect of sweep on $(L/D)_{max}$ was not nearly so pronounced for the flat-bottom models as for the flat-top models. As seen in figures 23(a) to 23(e), increasing sweep had little effect on the minimum drag coefficient. Increasing the wing sweep increased the body effect on C_L at $\alpha = 0^\circ$ (fig. 14(a)) and increased the value of the drag-due-to-lift parameter $C_{D,i}/C_L^2$ for the flat-top models but in general had little effect on the value of $C_{D,i}/C_L^2$ for the flat-bottom models. Trends in $(L/D)_{max}$ followed the trends in C_{L_α} as sweep angle was varied, since the change in C_L at $\alpha = 0^\circ$ and the change in $C_{D,i}/C_L^2$ tend to cancel each other.

Data from reference 6 showed trends in the lift-drag characteristics at the higher sweep angles which were similar to those discussed herein.

At a given angle of attack, it might be anticipated that a flat-top configuration would have higher axial force than its flat-bottom counterpart, since the pressure force on the body would be greater for the flat-top model. Such was the case for model 11, which had 81° of sweep. (See fig. 15.) However, a reduction in sweep angle increased the streamwise wedge angle of the wing and caused a rapid increase in the wing axial force for the flat-bottom configurations. This increased wing axial force exceeded the body axial force for the flat-top configuration and thus gave the flat-bottom configurations higher axial forces at the low leading-edge sweep angles, as shown for model 7 (60° of sweep) in figure 15.

Effects of Wingtip Deflection

A series of models with clipped arrow wings were tested at a Mach number of 6.86 and Reynolds numbers of 0.7×10^6 and 2.1×10^6 with several body locations and wingtip deflections of 0° and $\pm 45^\circ$. Some of the results of these tests are shown in figure 16(a). These results show that a wingtip deflection of 45° caused a loss in maximum lift-drag ratio regardless of body orientation. It should be noted, however, that deflection of the wingtips reduced the projected plan-form area. The loss in $(L/D)_{max}$ was generally greater for an upward deflection of the wingtips than for a downward deflection. A loss in lift-curve slope was also incurred when the wing tips were deflected.

Although deflection of the wingtips reduces $(L/D)_{max}$, it provides one means of increasing directional stability. A drag penalty would be incurred by use of a device capable of producing the same increment in directional stability. Therefore, the reduction in $(L/D)_{max}$ resulting from tip deflection must be weighed against the directional stability provided in each application. Additional data for models with deflected tips are presented in references 4, 6, and 8.

Effects of Body Geometry

Two delta-wing models with a leading-edge sweep of about 72° in combination with $7\frac{1}{2}^{\circ}$ and 5° semicones (models 12 and 9, respectively), and two delta-wing models with a leading-edge sweep of $77\frac{1}{2}^{\circ}$ in combination with a 5° semicone and a 5° semicone cylinder (models 10 and 14) were tested at $M = 6.86$ for both flat-top and flat-bottom orientations to assess the effects of body geometry. The results presented in figure 16(b) show that as body fineness ratio was increased, $(L/D)_{max}$ increased for both configurations. In fact, changing the body from the $7\frac{1}{2}^{\circ}$ cone to the 5° cone increased $(L/D)_{max}$ from 3.8 to 5.1 for the flat-top orientation, and changing from the 5° semicone to the 5° semicone cylinder increased $(L/D)_{max}$ from 4.8 to 5.4. The improvement in $(L/D)_{max}$ obtained by increasing the body fineness ratio was much greater than any increase obtained through use of favorable body interference at this Mach number. These relatively large improvements in L/D due to fineness ratio would be expected to extend to higher Mach numbers, whereas the use of favorable body interference has previously been shown to be ineffective at the higher hypersonic Mach numbers.

When the wingtips of the flat-top model 14-a were clipped to form model 15-a, the elimination of the low Reynolds number tip region caused some improvement in $(L/D)_{max}$. (See fig. 16(b).) However, clipping the wingtips of the flat-bottom model 14-b to form model 15-b had no effect on $(L/D)_{max}$.

SUMMARY OF RESULTS

An investigation has been conducted in the Langley 11-inch hypersonic tunnel to study the effects of body and wing plan-form geometry, body orientation, and wingtip deflection on the lift-drag characteristics of several wing-body combinations at hypersonic Mach numbers.

Within the restrictions of this investigation an analysis of these results has lead to the following conclusions:

1. Reasonable predictions of the lift-drag characteristics of wing-body combinations at hypersonic speeds can be made by use of several existing theoretical approaches. However, some effects of body orientation and wing leading-edge sweep were not accurately predicted.

2. Throughout the supersonic and low hypersonic speed range, the flat-top configurations exhibited higher maximum lift-drag ratios than their flat-bottom counterparts because of favorable body interference. However, the difference in maximum lift-drag ratio diminished with increasing hypersonic speeds and became essentially zero at a Mach number of about 10. At a Mach number of 6.86 a midwing configuration generally had about the same maximum lift-drag ratio as the flat-top configuration of equal body volume.

3. For a given body in combination with a series of delta wings, a variation in wing sweep, and hence in exposed wing area, resulted in approximately a 15-percent variation in maximum lift-drag ratio for the flat-top configurations, with the peak at a sweep of about 67°. The flat-bottom configurations showed the same trends but the variation was not nearly as pronounced.

4. Deflecting the wingtip, which has been proposed as a means for providing directional stability, resulted in a loss in maximum lift-drag ratio regardless of body position for a tip deflection of 45°. Upward deflection of the wingtips, however, resulted in a greater loss in lift-drag ratio than downward deflection.

Langley Research Center,
    National Aeronautics and Space Administration,
        Langley Field, Va., June 25, 1959.

APPENDIX A

DESIGN AND CALIBRATION OF THREE HELIUM NOZZLES IN THE

LANGLEY 11-INCH HYPERSONIC TUNNEL

By Donald L. Baradell and Thomas A. Blackstock

The extreme temperature and pressure requirements encountered in the use of air in wind-tunnel testing at Mach numbers greater than 10, coupled with the urgent need for information on aerodynamic phenomena at these Mach numbers, have led to the use of helium as a testing medium in hypersonic wind tunnels. Accordingly, three helium nozzles have been constructed and are presently in use in the Langley 11-inch hypersonic tunnel. These nozzles enable tests to be made at Mach numbers of 10.5, 13, and 18, to supplement data at Mach numbers of 6.9 and 9.6 from existing air nozzles. (See refs. 11 and 15.)

The Mach 10.5 and Mach 18 nozzles are contoured axisymmetric nozzles, designed by the method of characteristics (ref. 16) and corrected for boundary-layer displacement effects by the method presented by Persh and Lee in reference 17. The boundary-layer calculations as well as the computations of the nozzle characteristics net were performed on an IBM type 704 electronic data processing machine at the Langley Research Center.

The Mach 13 helium nozzle is two dimensional with flat parallel side walls. The contoured surfaces were designed by Foelsch's method (ref. 18) and a linear correction for boundary-layer displacement effects was applied to these surfaces.

Physical dimensions of the three nozzles are as follows:

Mach number of nozzle	Shape	Throat dimensions, in.	Test-section dimensions, in.	Length from throat to center of test section, in.
10.5	Circular	0.913 diam.	10.518 diam.	63.750
13	Rectangular	0.0131 by 9.950	10.514 by 9.950	56.844
18	Circular	0.368 diam.	10.518 diam.	68.438

Calibration of the nozzles consisted of a survey with an impact-pressure rake placed at several stations along the nozzle axis. Static pressures were obtained from orifices along the nozzle wall and with a static-pressure probe. The measured impact pressures agreed well with the expected pressures and indicated that the flow is steady in each of the three nozzles. At the Mach numbers encountered in these nozzles the boundary layer on the static-pressure probe is of the order of the radius of the probe or greater. The true stream static pressure is therefore difficult to evaluate accurately. When adjusted by an approximate method, however, the pressures obtained with the static probe as well as the static pressures measured on the nozzle wall were found to be consistent with the results of the impact-pressure survey for all the nozzles considered here. The following discussion of the results of the pressure survey is limited to impact pressures.

No survey of flow angularity was conducted, but schlieren photographs obtained during the calibration runs showed that flow angularity in the test region is less than 1° for each of the axisymmetric nozzles.

For the Mach 10.5 helium nozzle the impact-pressure survey indicated that the average Mach number in the center of the test region is 10.5 for a stagnation pressure p_t of 190 lb/sq in., 10.8 for p_t = 300 lb/sq in., and 11.0 for p_t = 400 lb/sq in. Although no survey was conducted at design stagnation pressure $\left(p_t = 100 \text{ lb/sq in.}\right)$ an extrapolation of the experimental results indicates that the design Mach number of 10 would be obtained if the nozzle were operated at design pressure.

As seen in figure 27, the core of good flow is more than 6 inches in diameter and the longitudinal Mach number gradient in the test region along the nozzle axis is only 0.01 per inch.

The average length of the calibration runs in the Mach 10.5 helium nozzle was 14 seconds.

For the Mach 18 helium nozzle the impact-pressure survey shown in figure 28 indicates that the core of good flow is slightly more than 4 inches in diameter. The average Mach number in the core at the test-section center line for design stagnation pressure $\left(p_t = 1,000 \text{ lb/sq in.}\right)$ is 17.8; with a longitudinal Mach number gradient along the nozzle axis of about 0.05 per inch. For p_t = 1,600 lb/sq in., the average Mach number in the core at the test-section center line is 18.4.

The average length of the calibration runs in the Mach 18 helium nozzle was 16 seconds.

The Mach 13 helium nozzle was constructed by remachining a set of blocks from a discarded air nozzle. This procedure limited the physical dimensions, necessitated two dimensionality, and allowed no correction for boundary layer on the side walls. The flow field was designed by Foelsch's method (ref. 18) to produce flow at a Mach number of 17.5 in the test region. A linear correction for boundary-layer displacement effects was applied to the contoured surfaces. The presence of boundary layer on the side walls, however, reduced the effective flow area of the test section and the Mach number obtained in the test region was reduced to 13 for a stagnation pressure p_t of 1,000 lb/sq in. The flow in the test region contains some angularity, which was determined to be less than 2° for a region in the center of the test section measuring 2 inches horizontally and 4 inches vertically. Because of the methods of design and construction of the Mach 13 nozzle, the flow is understandably of a poorer quality than the flow in the other nozzles considered here. For this reason, the nozzle is destined for only limited use, and no detailed calibration results are presented.

L
2
4
7

APPENDIX B

DESCRIPTION OF THEORETICAL METHODS

Local Flow

To determine the forces on a combination of wing and semicone body, a theoretical approach was considered, based on a nonviscous flow field of the two-shock type as shown in the following sketch:
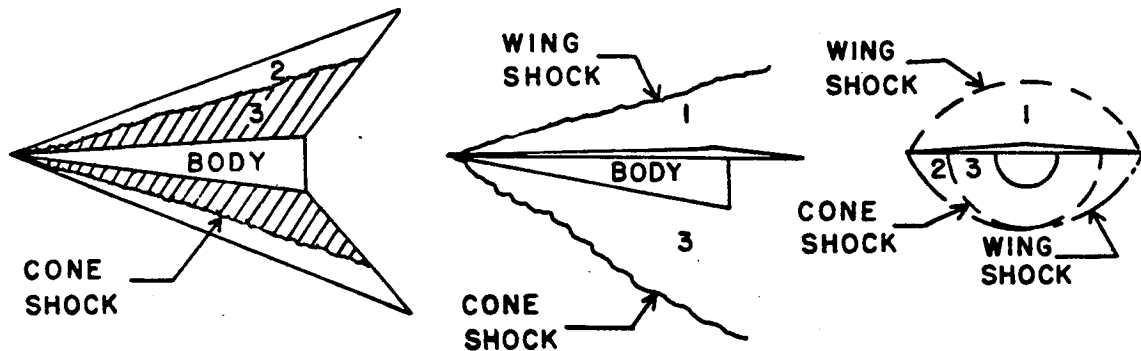
A brief description of this method is included in reference 19. The body was assumed to operate in the region of local flow behind the wing leading edge, and the region between the body and the intersection of the body shock with the wing is assumed to be the region of body interference. Two-dimensional flow was assumed to exist on the portion of the wing outboard of the body shock. Recent unpublished surveys of the flow about wing-body combinations of the type considered in this investigation indicate that the flow field of such configurations may more generally form a single shock pattern falling at or near the wing leading edge. However, reasonable predictions of the lift-drag characteristics can be made by use of the simplifying assumption of a two-shock flow field.

The flow fields over the wing were divided into the regions shown in the sketch. Regions 1 and 2 were considered to be regions of two-dimensional flow, and the local pressure was determined by two-dimensional shock-expansion theory. The cone was assumed to operate at an angle of attack of 0° in the local flow behind the wing throughout the angle-of-attack range. The surface pressure for the unyawed cone was determined from tables of reference 20. The interference region is shown as region 3 and is shaded in the sketch. The pressure

in this region was assumed to be an average of the cone surface pressure and the pressure behind the body shock wave. If the conditions existing in each of these regions are known, the ratio of local static pressure p to free-stream static pressure p_∞ may be obtained and the pressure coefficient of each region can then be determined from the equation

$C_p = \dfrac{2}{\gamma M_\infty^2} \left(\dfrac{p}{p_\infty} - 1 \right)$. The normal and axial-force coefficients for this

type of body-wing configuration may then be obtained by determining the force contribution of each region based on the reference area.

Modified Local Flow

To account for the effects of leading-edge-shock detachment and induced effects on the calculated normal-force coefficient, an analysis was made of the experimental data for some delta wings presented in reference 21. The ratios of experimental to calculated normal-force coefficient (computed by means of the shock-expansion theory) were obtained for several of these wings throughout the angle-of-attack range. By means of the hypersonic similarity parameters, these ratios could be obtained for wings of the present investigation. The resulting ratios were then used to correct the predicted normal-force coefficient for shock detachment and other induced effects.

Method of Reference 7

A method of predicting forces on flat-top wing-body conbinations is presented in reference 7. This theory assumes the existence of a single shock attached to the wing leading edge of the configuration and is applicable only to flat-top configurations. In any analysis utilizing this method, the flow field must satisfy the boundary conditions corresponding to the single-shock type of flow field with the shock attached to the leading edge. Since the shock pattern is a function of model geometry, Mach number, and angle of attack, these parameters must be of the proper magnitudes to satisfy these boundary conditions. At a Mach number of 6.86, model 13 could be treated by this method but the sweep of model 9 was not great enough to satisfy these boundary conditions. At a Mach number of 9.6 neither model could be analyzed.

Modified Newtonian

In using the modified Newtonian theory, the forces on the body and wing were claculated by the method of reference 22 modified so that

$C_p = C_{p,max} \sin^2 \delta$, where δ is the local flow-deflection angle and $C_{p,max}$ is taken equal to the stagnation-pressure coefficient behind a normal shock. This modified Newtonian theory has been used in the past to estimate forces on winged configurations at hypersonic speeds and is included in this paper solely for comparison purposes.

Newtonian-Shock-Expansion

In the Newtonian-shock-expansion method, the modified Newtonian theory was used to calculate forces over the body, but forces over the exposed wing area were determined by two-dimensional shock-expansion theory. Thus this theory neglects the effects of the body-interference region. Shock-detachment effects on normal force were accounted for when applicable.

REFERENCES

1. Eggers, Alfred J., Jr., Allen, H. Julian, and Neice, Stanford E.: A Comparative Analysis of the Performance of Long-Range Hypervelocity Vehicles. NACA TN 4046, 1957. (Supersedes NACA RM A54L10.)

2. Seiff, Alvin, and Allen, H. Julian: Some Aspects of the Design of Hypersonic Boost-Glide Aircraft. NACA RM A55E26, 1955.

3. Ferri, Antonio, Clarke, Joseph H., and Casaccio, Anthony: Drag Reduction in Lifting Systems by Advantageous Use of Interference. PIBAL Rep. No. 272 (Contract AF 18(600)-694), Polytechnic Inst. Brooklyn, May 1955.

4. Eggers, A. J., Jr., and Syvertson, Clarence A.: Aircraft Configurations Developing High Lift-Drag Ratios at High Supersonic Speeds. NACA RM A55L05, 1956.

5. Migotsky, Eugene, and Adams, Gaynor J.: Some Properties of Wing and Half-Body Arrangements at Supersonic Speeds. NACA RM A57E15, 1957.

6. Syvertson, Clarence A., Wong, Thomas J., and Gloria, Hermilo R.: Additional Experiments With Flat-Top Wing-Body Combinations at High Supersonic Speeds. NACA RM A56I11, 1957.

7. Savin, Raymond C.: Approximate Solutions for the Flow About Flat-Top Wing-Body Configurations at High Supersonic Airspeeds. NACA RM A58F02, 1958.

8. Syvertson, Clarence A., Gloria, Hermilo R., and Sarabia, Michael F.: Aerodynamic Performance and Static Stability and Control of Flat-Top Hypersonic Gliders at Mach Numbers From 0.6 to 18. NACA RM A58G17, 1958.

9. Love, Eugene S., Henderson, Arthur, Jr., and Bertram, Mitchel H.: Some Aspects of Air-Helium Simulation and Hypersonic Approximations. NASA TN D-49, 1959.

10. Shapiro, Ascher H.: The Dynamics and Thermodynamics of Compressible Fluid Flow. Vol. II. The Roland Press Co., c.1954.

11. Bertram, Mitchel H.: Boundary-Layer Displacement Effects in Air at Mach Numbers of 6.8 and 9.6. NACA TN 4133, 1958.

12. Penland, Jim A.: Aerodynamic Characteristics of a Circular Cylinder at Mach Number 6.86 and Angles of Attack Up to 90°. NACA TN 3861, 1957. (Supersedes NACA RM L54A14.)

L
2
4
7

13. Bertram, Mitchel H., and Henderson, Arthur, Jr.: Effects of Boundary-Layer Displacement and Leading-Edge Bluntness on Pressure Distributions, Skin Friction, and Heat Transfer of Bodies at Hypersonic Speeds. NACA TN 4301, 1958.

14. Tellep, D. M.: Lift on Flat Plates in Low Density Supersonic Flow. Rep. No. HE-150-131 (Ser. No. 20-104, Contract N7-onr-295-Task 3), Inst. Eng. Res., Univ. of California, Aug. 30, 1955.

15. Bertram, Mitchel H.: Exploratory Investigation of Boundary-Layer Transition on a Hollow Cylinder at a Mach Number of 6.9. NACA Rep. 1313, 1957. (Supersedes NACA TN 3546.)

16. Beckwith, Ivan E., Ridyard, Herbert W., and Cromer, Nancy: The Aerodynamic Design of High Mach Number Nozzles Utilizing Axisymmetric Flow With Application to a Nozzle of Square Test Section. NACA TN 2711, 1952.

17. Persh, Jerome, and Lee, Roland: A Method for Calculating Turbulent Boundary Layer Development in Supersonic and Hypersonic Nozzles Including the Effects of Heat Transfer. NAVORD Rep. 4200 (Aeroballistic Res. Rep. 320), U. S. Naval Ord. Lab. (White Oak, Md.), June 7, 1956.

18. Foelsch, Kuno: A New Method of Designing Two-Dimensional Laval Nozzles for a Parallel and Uniform Jet. Rep. No. NA-46-235-2, North American Aviation, Inc., May 27, 1946.

19. Rainey, Robert W.: Static Stability and Control of Hypersonic Gliders. NACA RM L58E12a, 1958.

20. Staff of the Computing Section, Center of Analysis (Under Direction of Zdenĕk Kopal): Tables of Supersonic Flow Around Cones, Tech. Rep. No. 1 (NOrd Contract No. 9169), M.I.T., 1947.

21. Bertram, Mitchel H., and McCauley, William D.: An Investigation of the Aerodynamic Characteristics of Thin Delta Wings With a Symmetrical Double-Wedge Section at a Mach Number of 6.9. NACA RM L55B14, 1955.

22. Grimminger, G., Williams, E. P., and Young, G. B. W.: Lift on Inclined Bodies of Revolution in Hypersonic Flow. Jour. Aero. Sci., vol. 17, no. 11, Nov. 1950, pp. 675-690.

L
2
4
7

TABLE I

ORDINATES OF BODY USED FOR MODELS 2, 4, and 6

x, in.	r, in.
0	0
.353	.05149
.706	.08811
1.059	.1209
1.412	.1513
1.765	.1802
2.118	.2078
2.471	.2345
2.824	.2605
3.177	.2858
3.530	.3105
3.883	.3347
4.236	.3585
4.589	.3818
4.942	.4048
5.295	.4275
5.648	.4499
6.001	.4720
6.354	.4938
6.707	.5154
7.060	.5367
7.929	.5367

0.040D

$r = r_b \left(\frac{x}{l}\right)^{3/4}$

Body A

0.040D

7.00

8.07

1.24

Body B

0.040D

Body C

Ordinates are presented in table I

77.4°

0.002
L.E. rad.

7.00

9.92

3°

1°

Model	Geometry	θ_F, deg	Body	S, sq in.	$\bar{c}$, in.
1-a		0	A	15.64	3.77
1-b		0	B	15.64	3.77
2		0	C	15.64	3.77
3-a		45	A	15.64	3.77
3-b		45	B	15.64	3.77
4		45	C	15.64	3.77
5-a		-45	A	15.64	3.77
5-b		-45	B	15.64	3.77
6		-45	C	15.64	3.77

θ_F

Section A-A

3.09

3.92

Wing plan form.
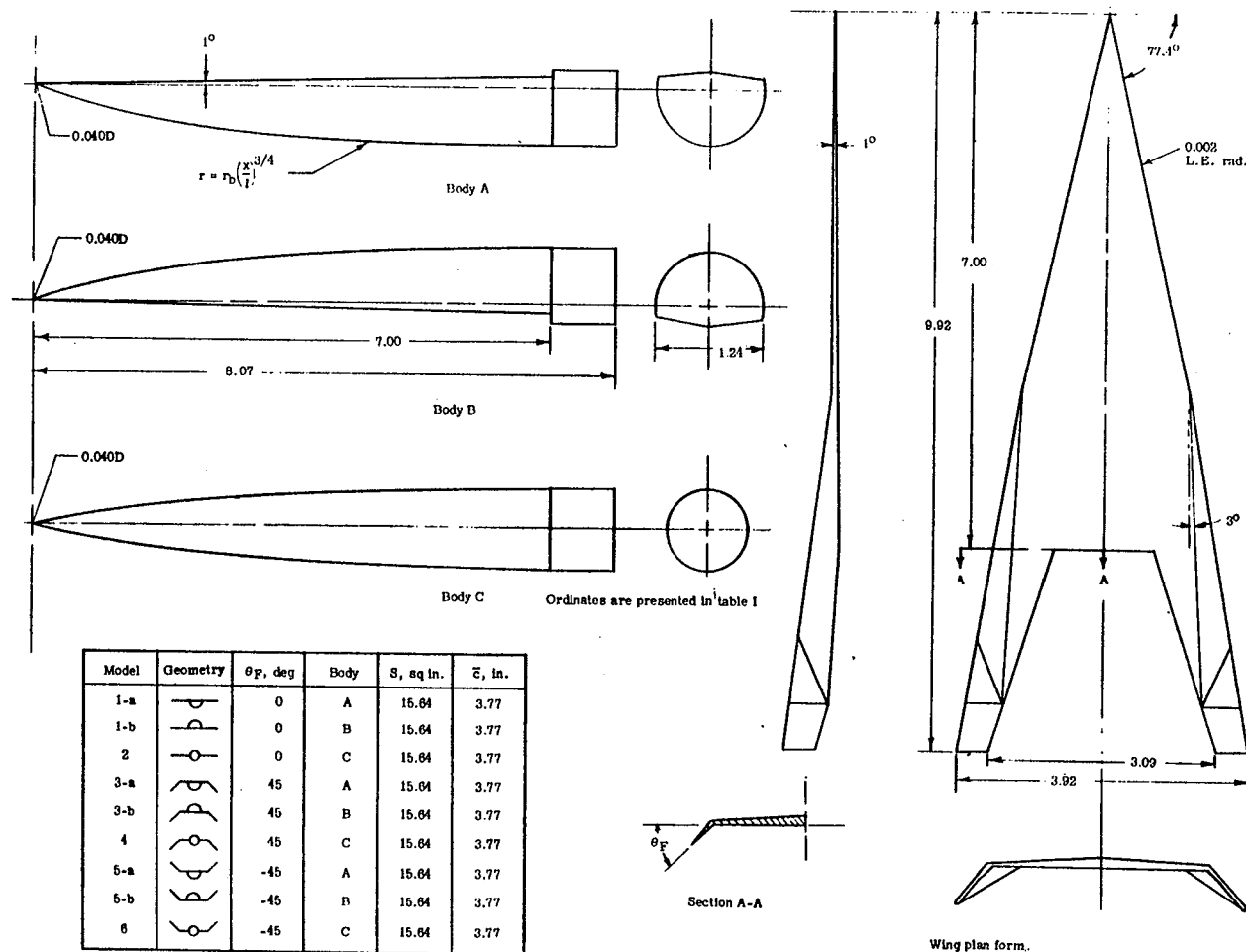
(a) Models 1 to 6.

Figure 1.- Three-view drawing of models. All linear dimensions are in inches.
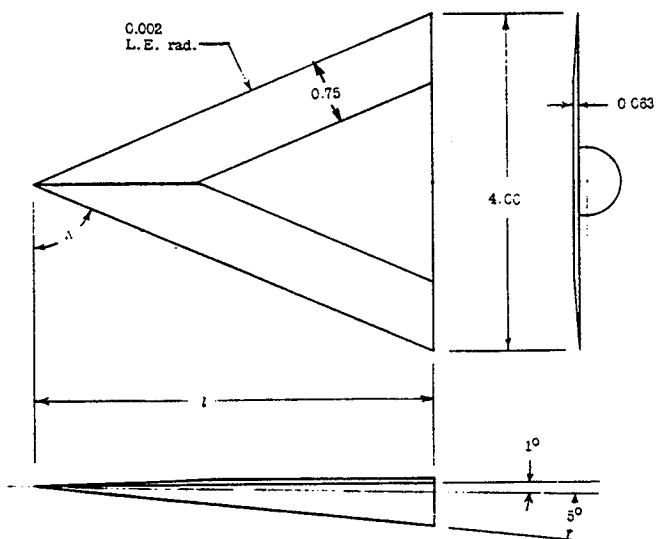
Model	Λ, deg	l, in.	S, sq in.	$\bar{c}$, in.
7	60	3.46	6.92	2.29
8	67	4.71	9.42	3.16
9	72	6.15	12.31	4.10
10	77.5	9.02	18.06	6.02
11	81	12.90	25.26	8.40

Models 7 to 11

Note:
Flat-top configuration denoted by suffix "a."

Flat-bottom configuration denoted by suffix "b."

S = 14.90 sq in.

$\bar{c}$ = 4.44 in.
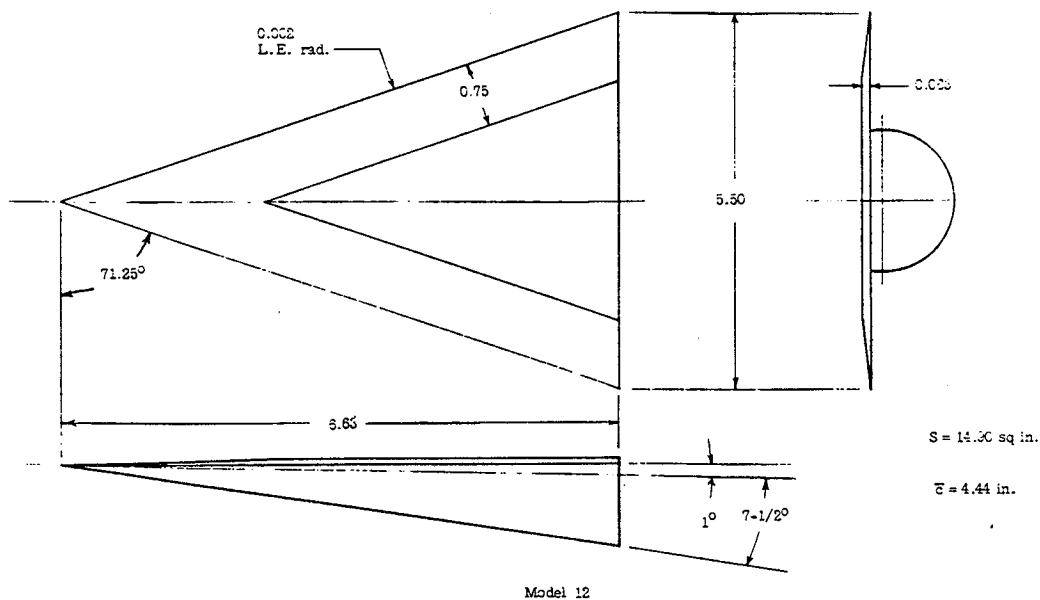
Model 12

(b) Models 7 to 12.

Figure 1.- Continued.

Model	Body	Plan form	S, sq in.	c̄, in.
13	5° cone	Arrow	13.16	4.23
14	5° cone cyl.	Delta	31.92	8.00
15	5° cone cyl.	Clipped delta	29.94	8.40
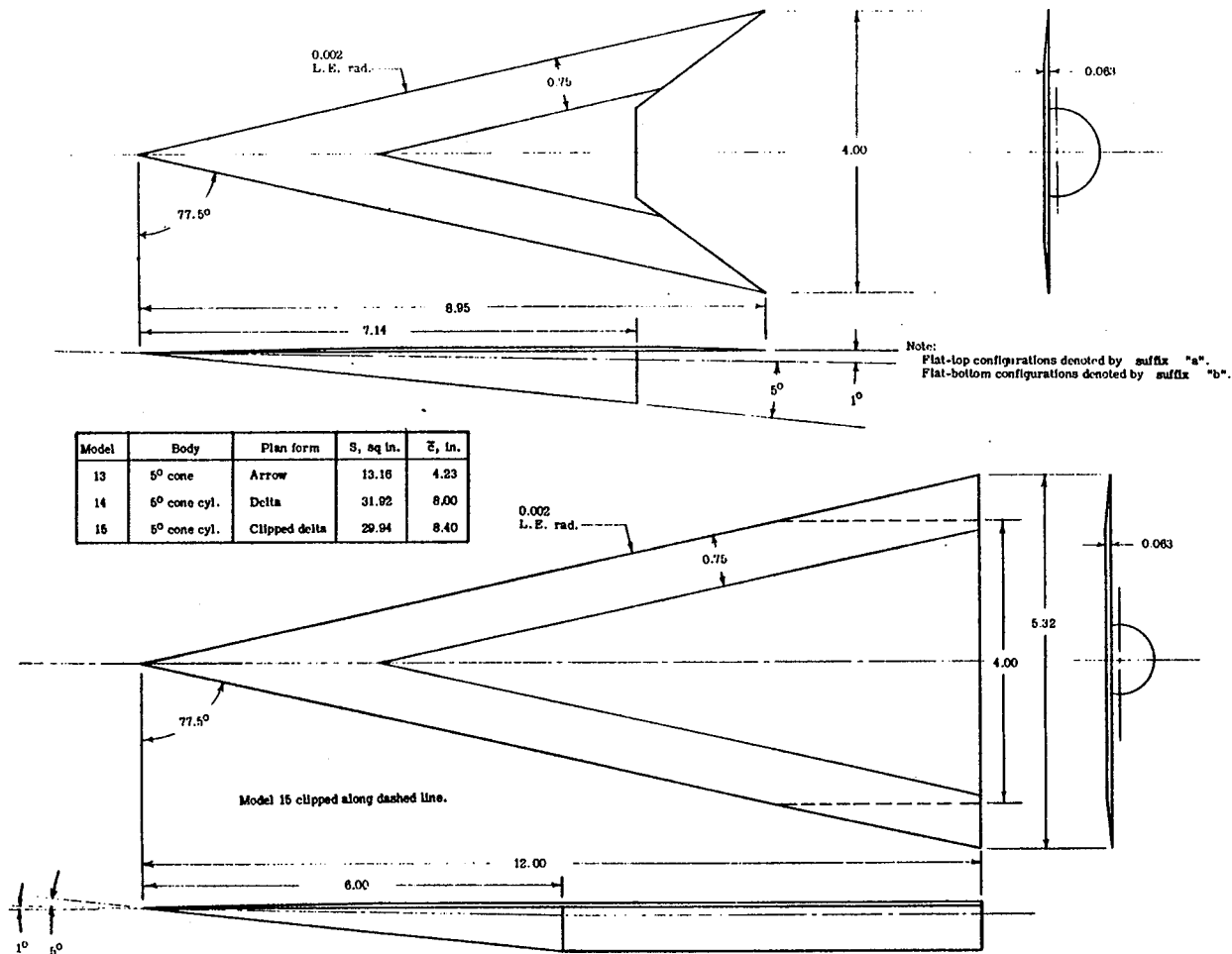
(c) Models 13 to 15.

Figure 1.- Concluded.
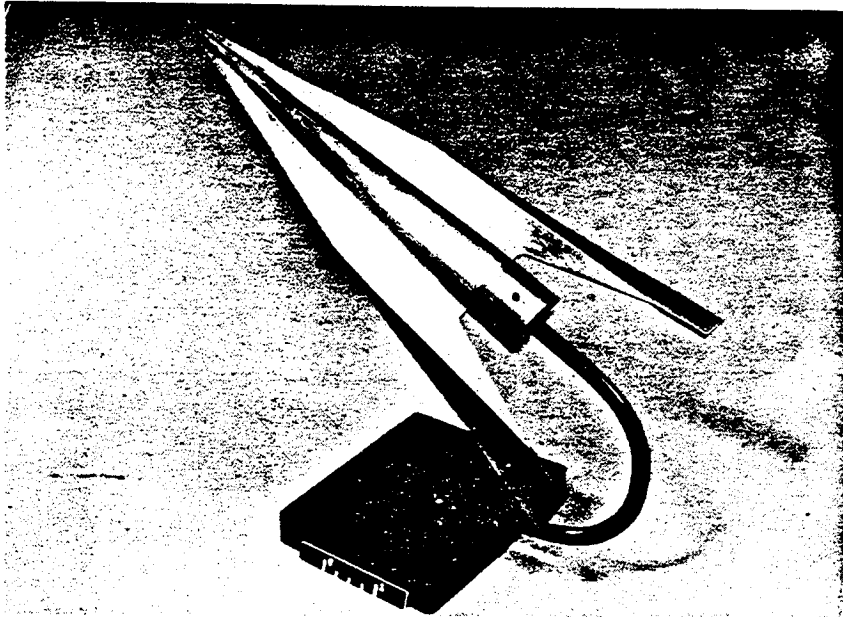
(a) Model 4.   L-58-2171
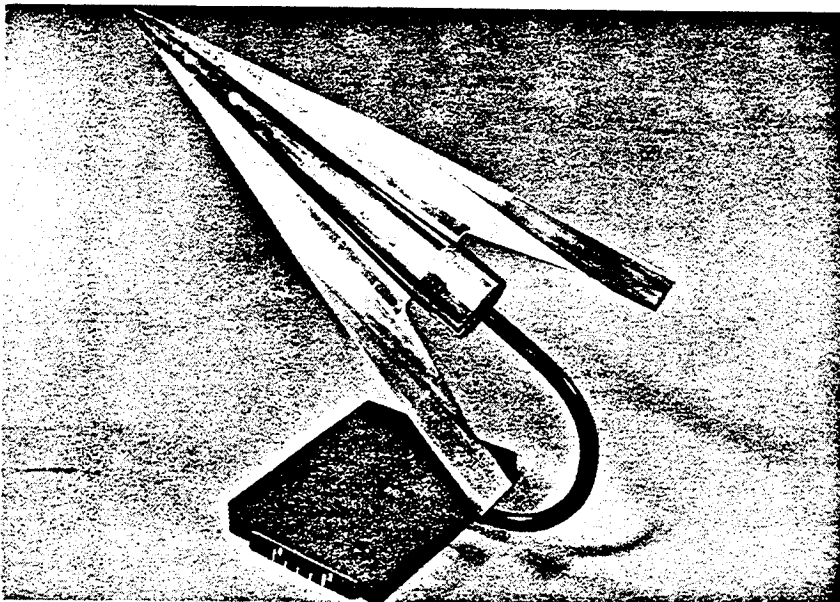
(b) Model 6.   L-58-2172

Figure 2.- Photographs of model configurations.

L-247
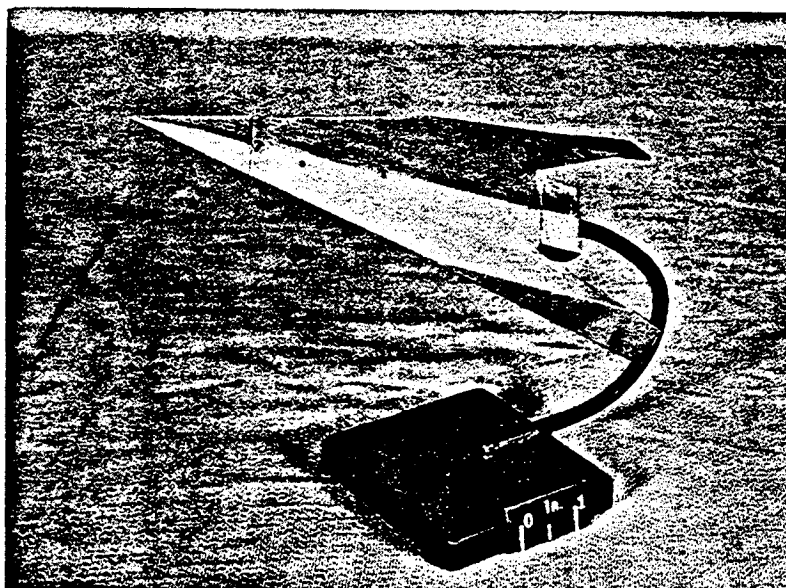
(c) Model 3-a.   L-57-4603
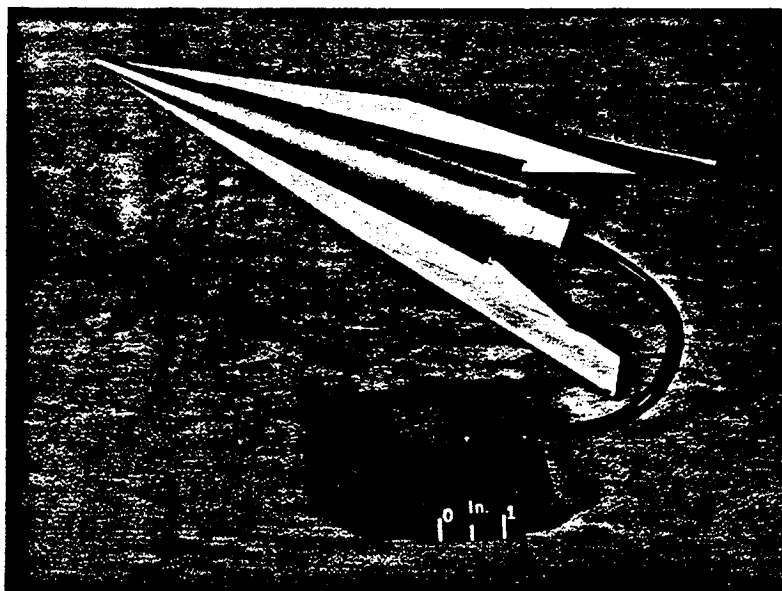
(d) Model 5-b.   L-57-4602

Figure 2.- Continued.
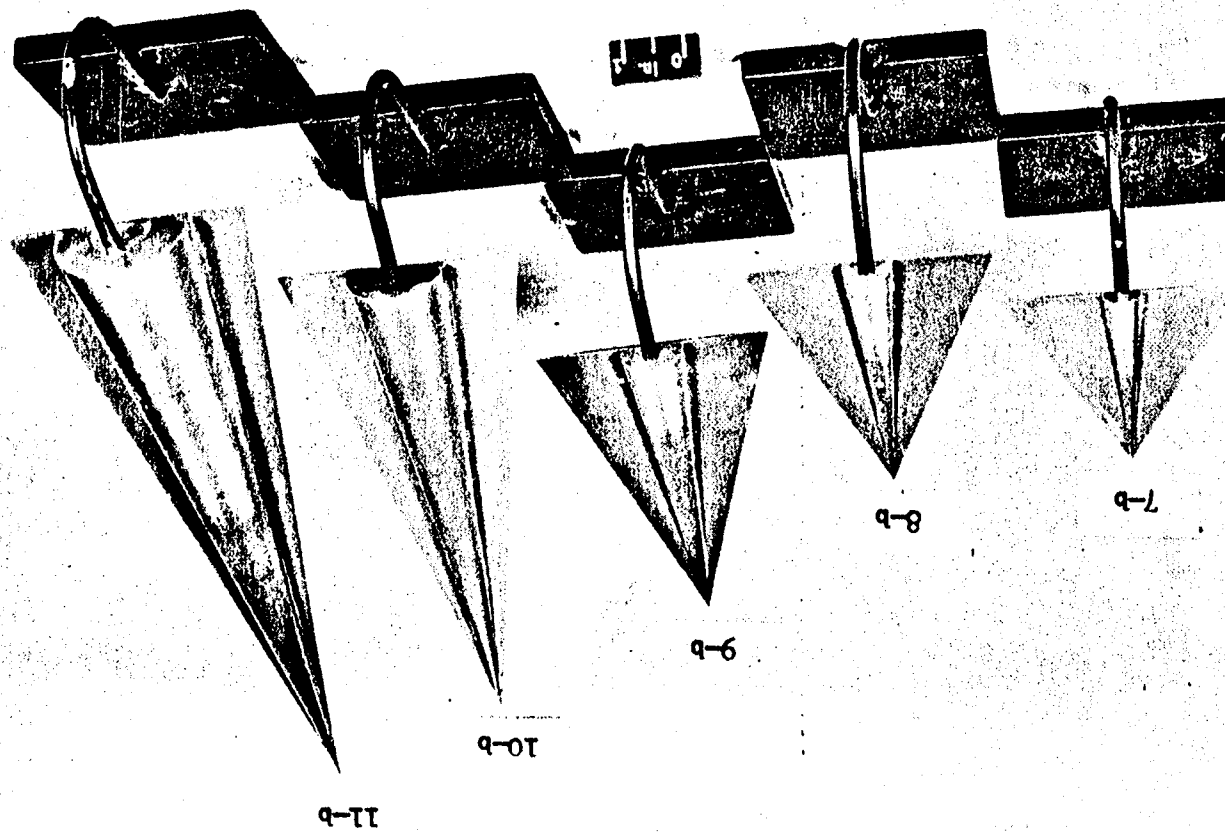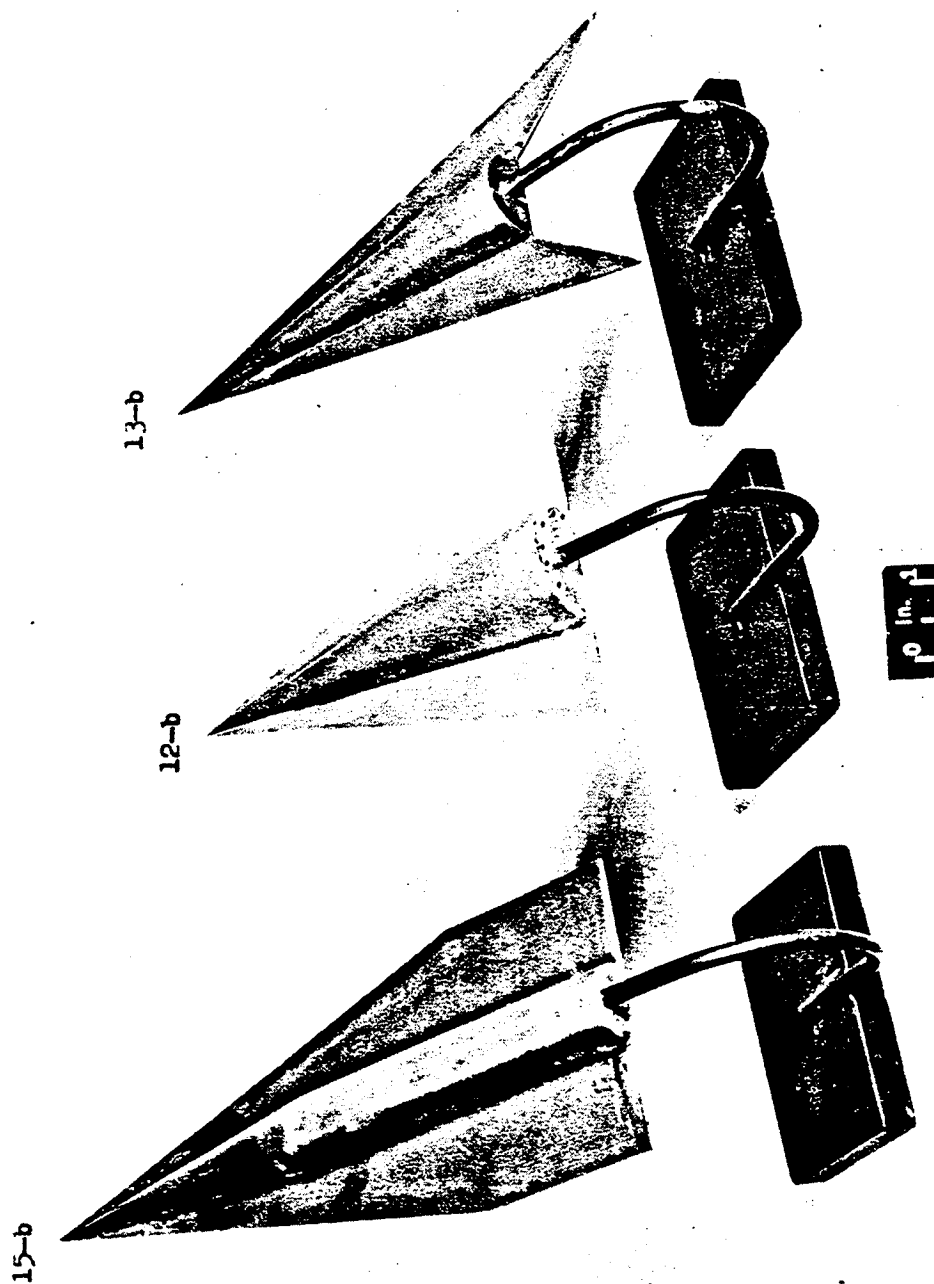
(f) Models 12, 13, and 15.   L-57-4614.1

Figure 2.- Concluded.
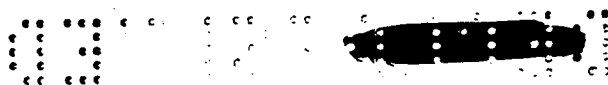
M = 6.86 in air
$\alpha = 7^\circ$, R = 2.1 × 10⁶

M = 9.6 in air
$\alpha = 10^\circ$, R = 0.7 × 10⁶
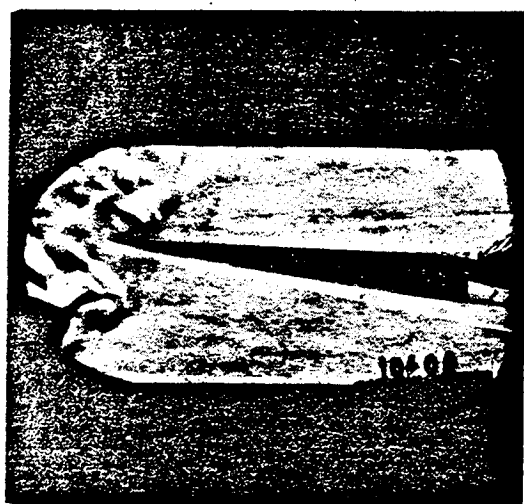
M = 10.5 in helium
$\alpha = 3^\circ$, R = 1.6 × 10⁶
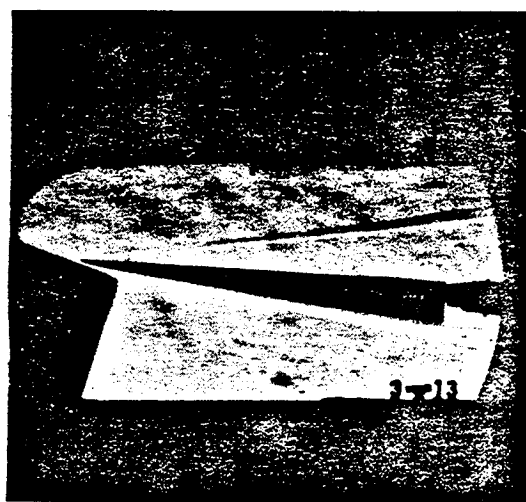
M = 17.8 in helium
$\alpha = 4^\circ$, R = 3.4 × 10⁶

(a) Model 1-a.   L-59-3073

Figure 3.- Schlieren photographs showing typical flow patterns of tests
made in both air and helium.
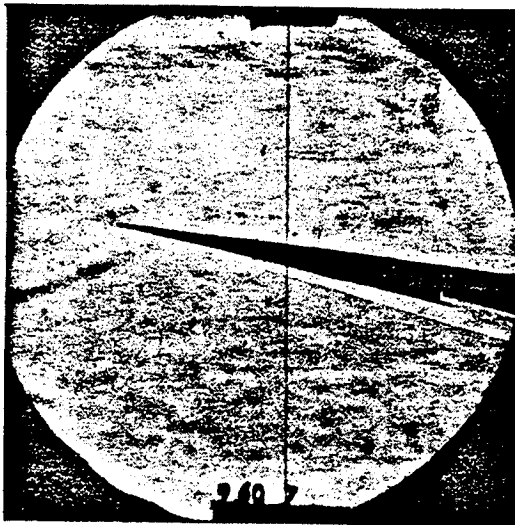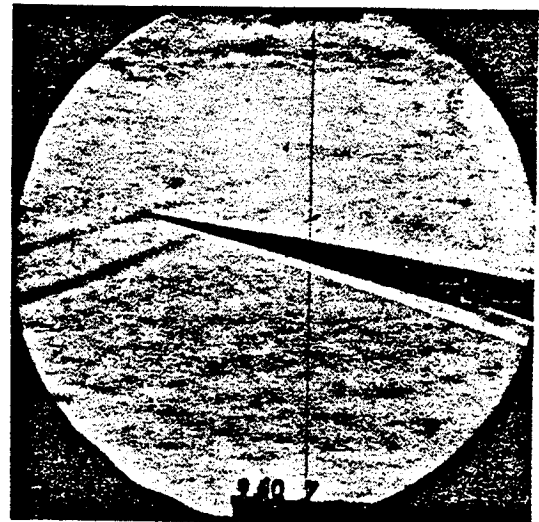
Model 13-a
$\alpha = 7^\circ$

Model 13-a
$\alpha = 9^\circ$
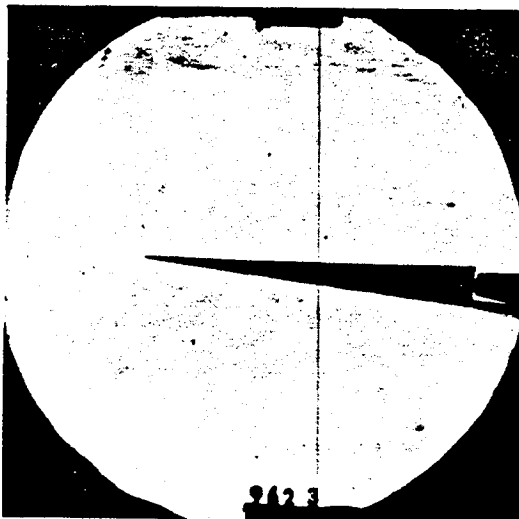
Model 13-b
$\alpha = 7^\circ$
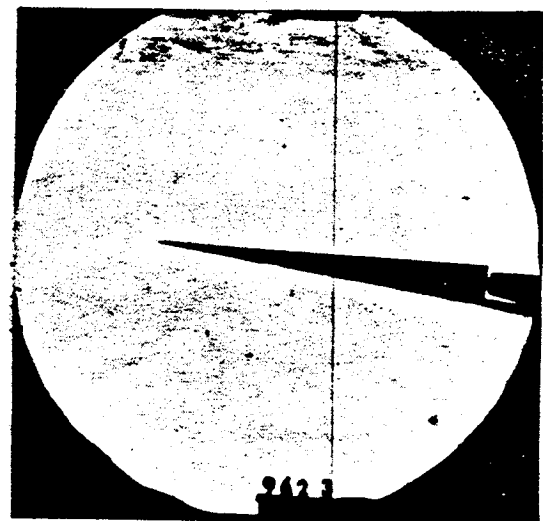
Model 13-b
$\alpha = 9^\circ$

(b) Models 13. $M = 6.86$ in air; $R = 1.3 \times 10^6$.

L-59-3074

Figure 3.- Continued.
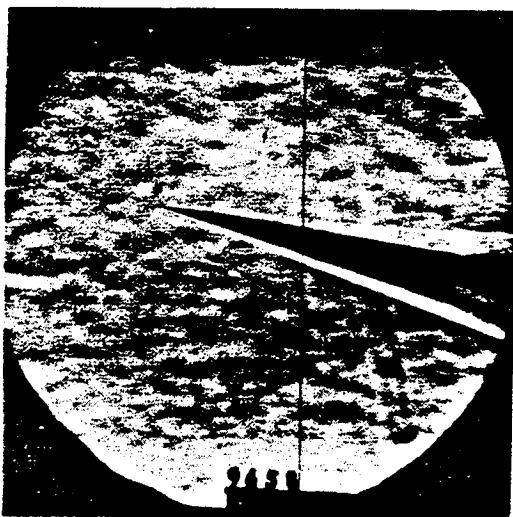
Model 12-a
α = 9°
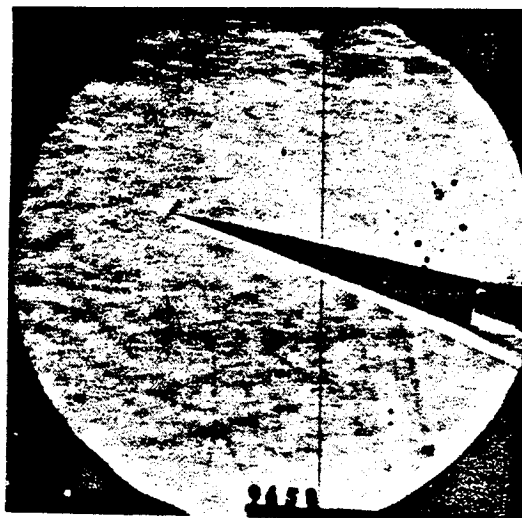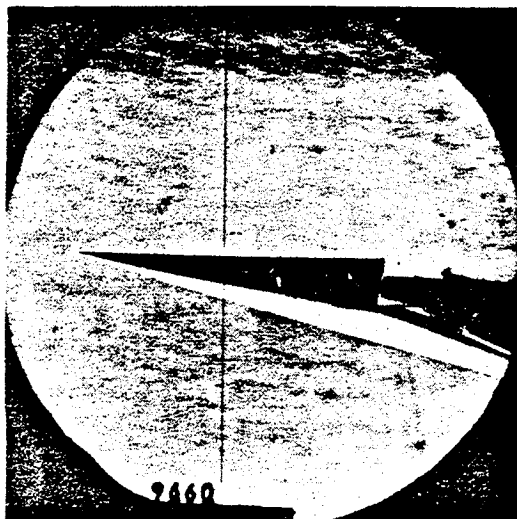
Model 12-a
α = 12°
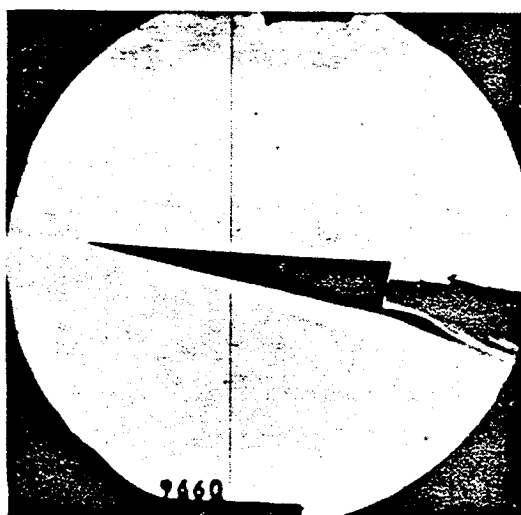
Model 12-b
α = 9°

Model 12-b
α = 12°

(c) Models 12.   M = 6.86 in air; R = 1.3 × 10^6.   L-59-3075

Figure 3.- Continued.
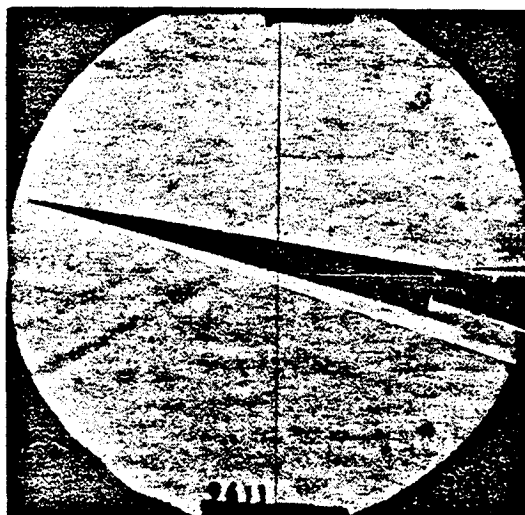
Model 10-a
5° conic body
α = 9°
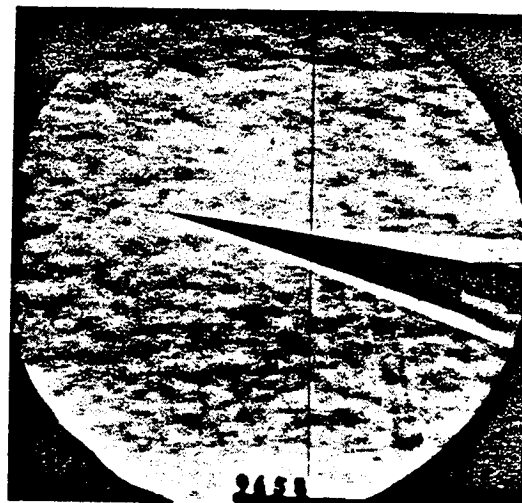
Model 12-a
7.5° conic body
α = 9°
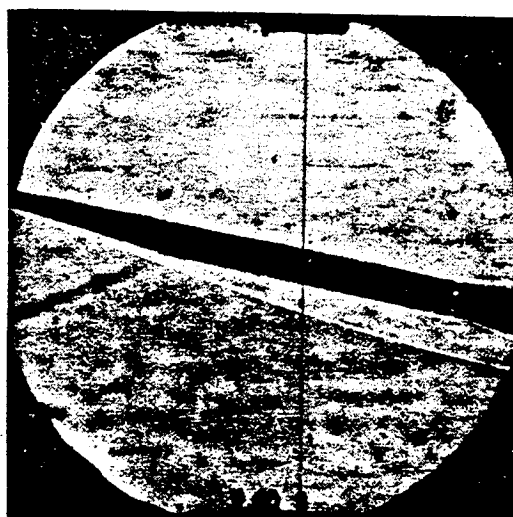
Model 14-a
5° cone-cylinder body
α = 11°

L-59-3076

(d) Several delta-wing models of differing body geometry. $\Lambda = 77.5°$; $M = 6.86$ in air; $R = 1.3 \times 10^6$.

Figure 3.- Concluded.
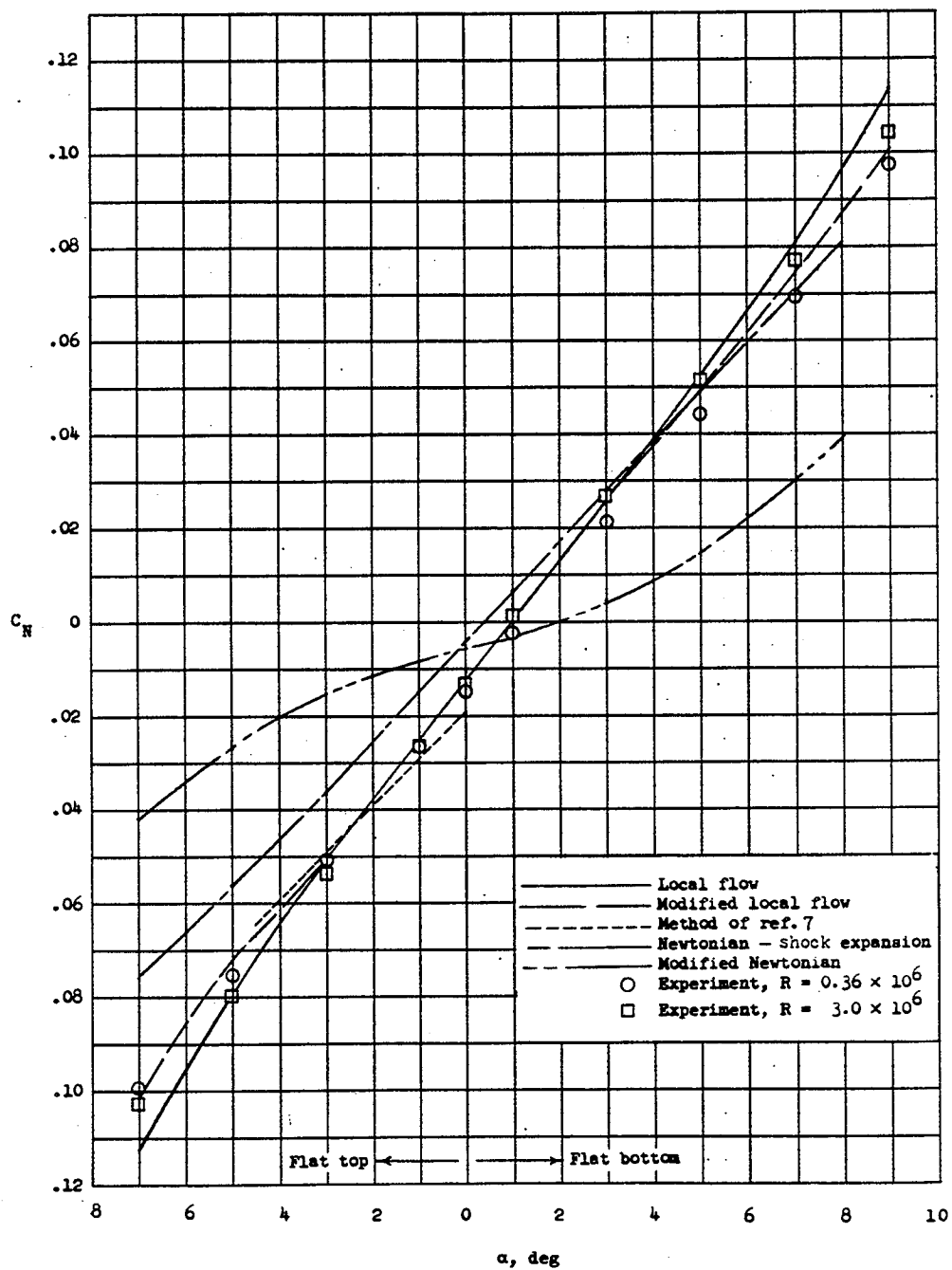
(a) Model 13 (semicone body, arrow wing). M = 6.86.

Figure 4.- Variation of experimental and theoretical normal-force
coefficients with angle of attack.
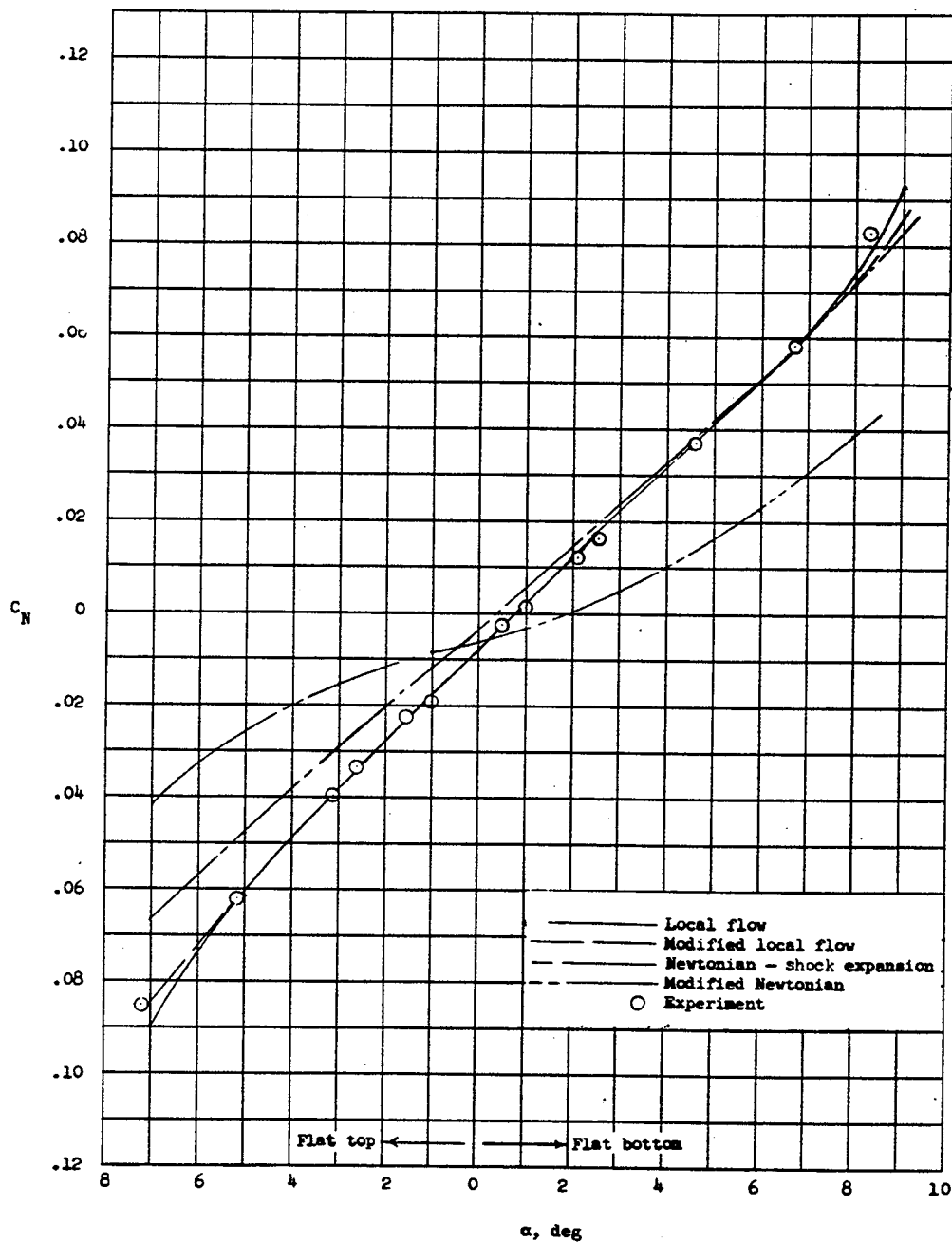
(b) Model 13 (semicone body, arrow wing). M = 9.6; R = 0.7 × 10^6.

Figure 4.- Continued.
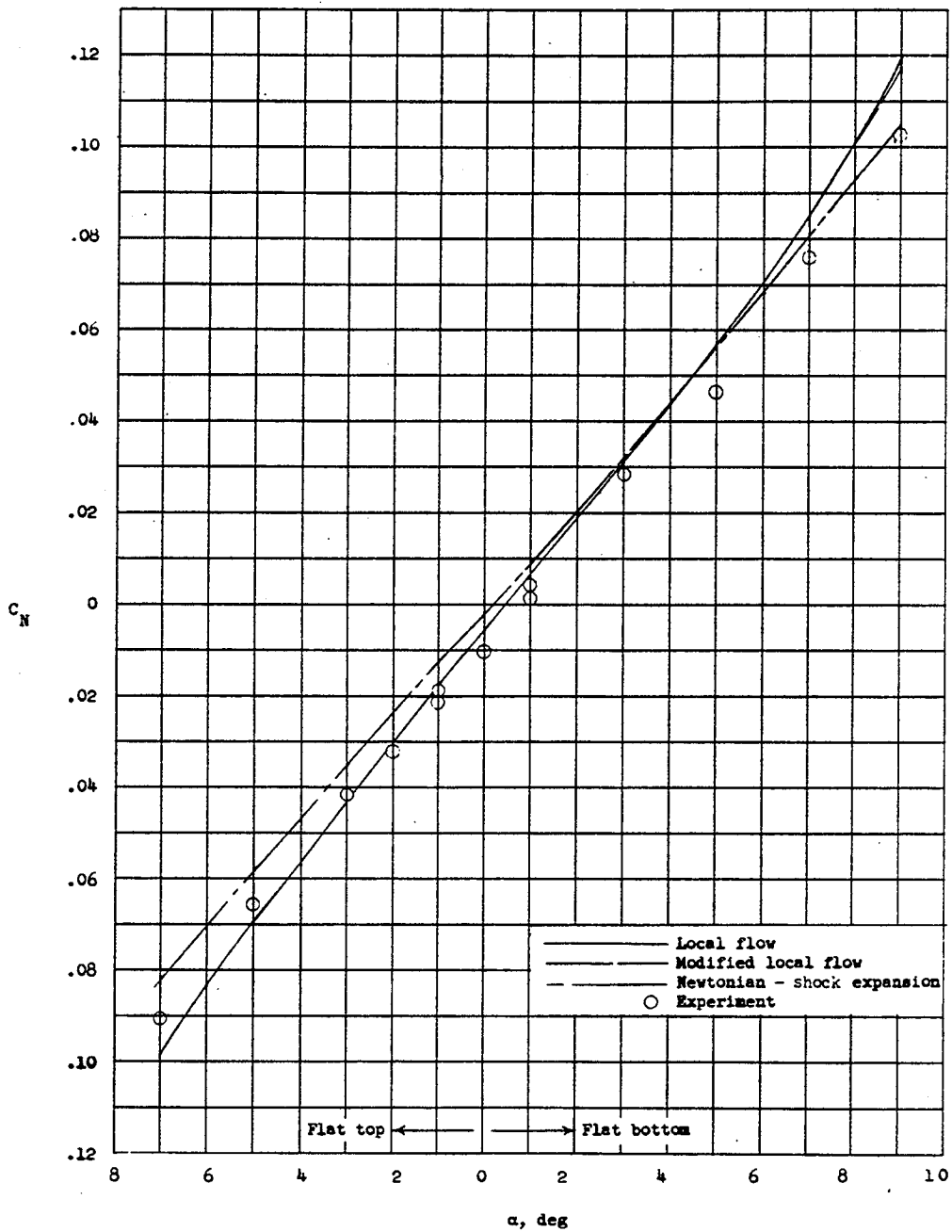
(c) Model 9 (semicone body, delta wing). M = 6.86; R = 0.36 × 10⁶.

Figure 4.- Continued.
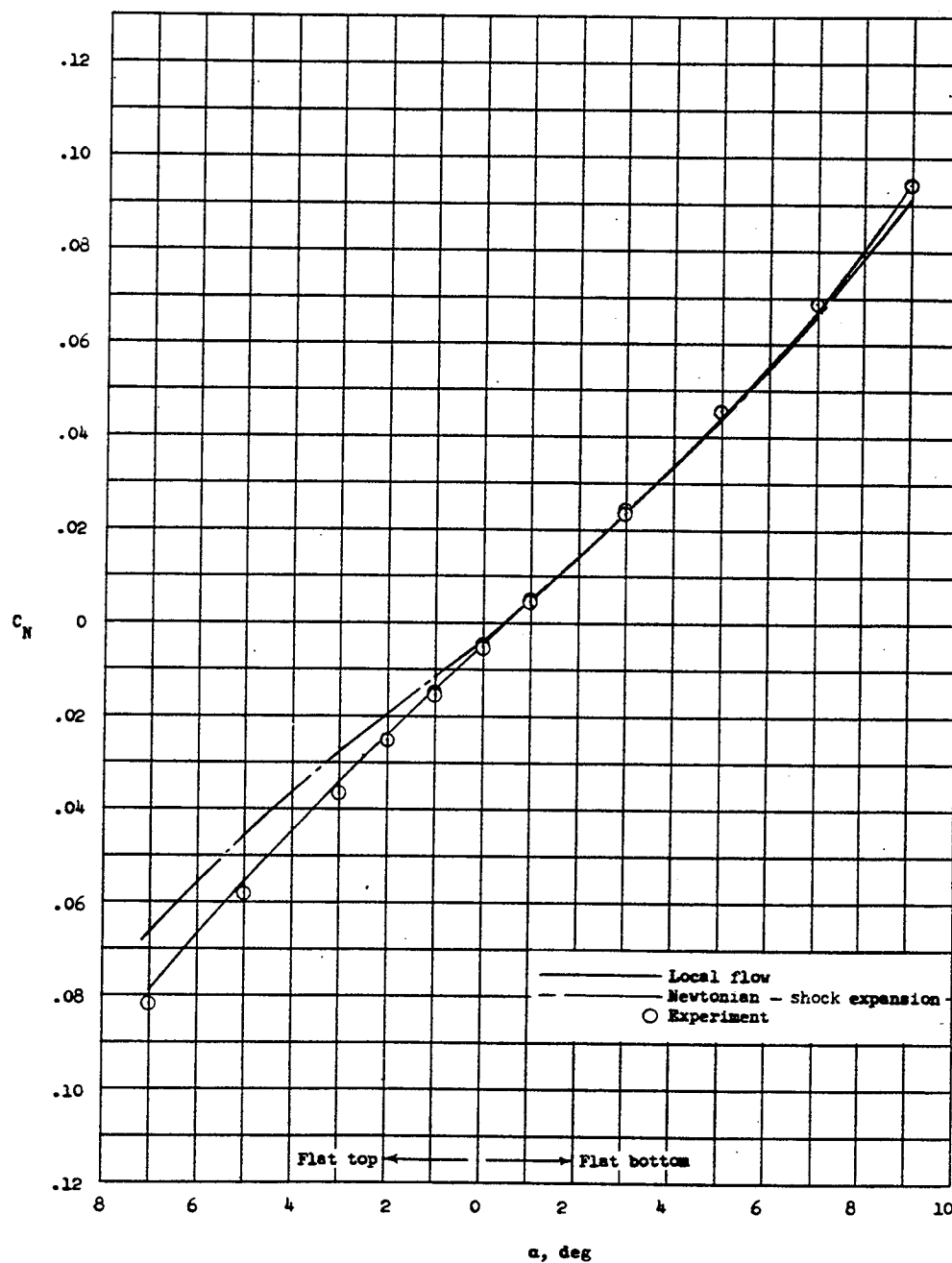
(d) Model 9 (semicone body, delta wing). M = 9.6; R = 0.7 × 10^6.

Figure 4.- Concluded.
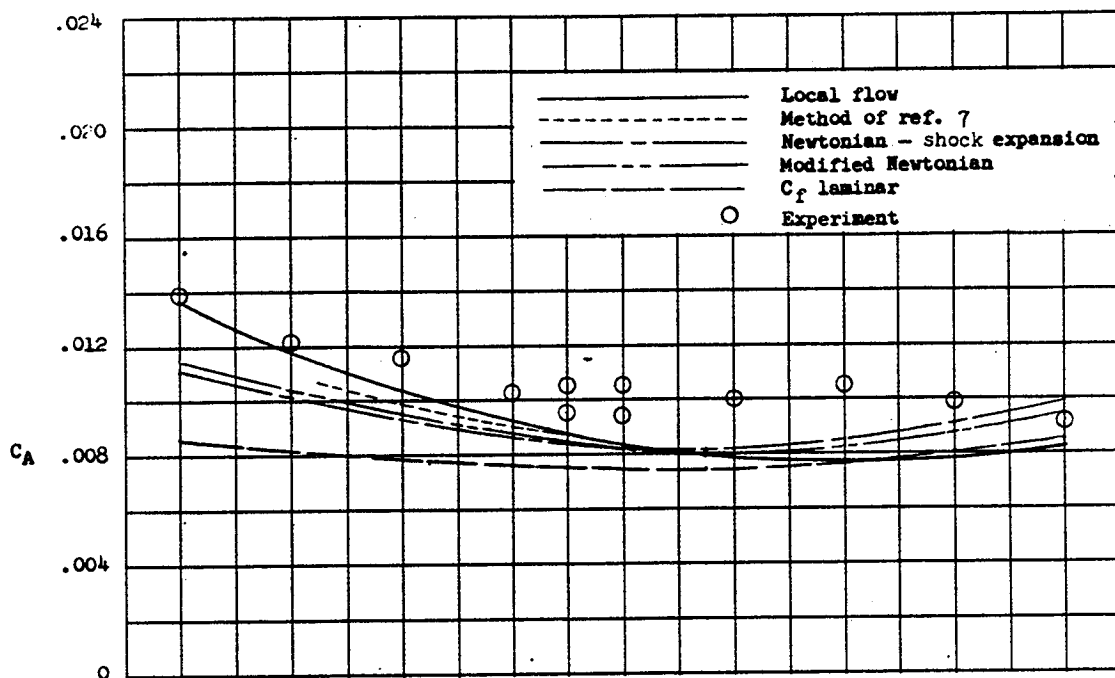
(a) Model 13 (semicone body, arrow wing). $M = 6.86$; $R = 0.36 \times 10^6$.
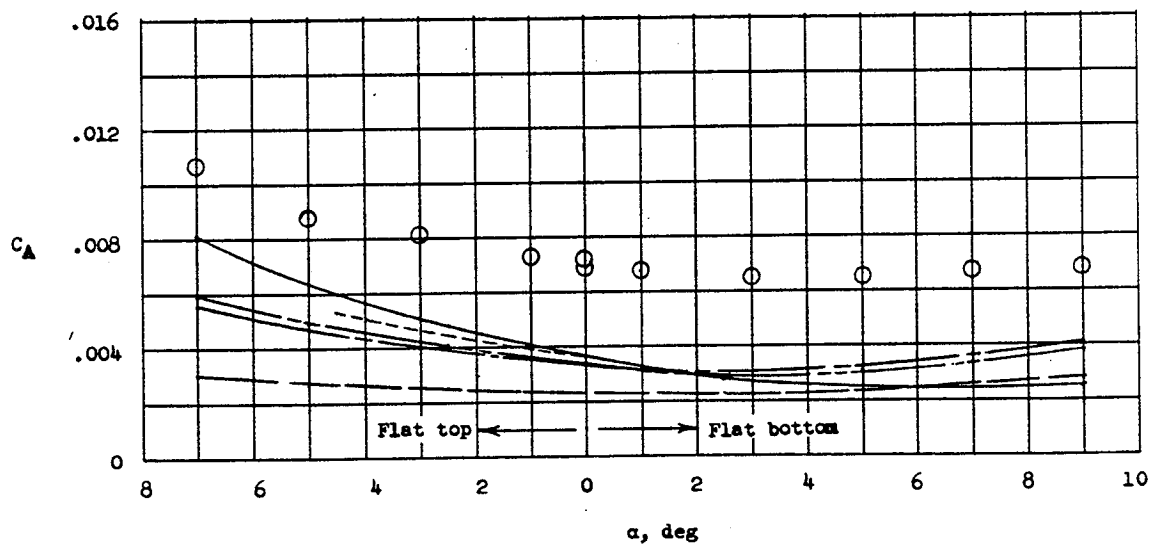
(b) Model 13 (semicone body, arrow wing). $M = 6.86$; $R = 3.0 \times 10^6$.

Figure 5.- Variation of experimental and theoretical axial-force coefficients with angle of attack.
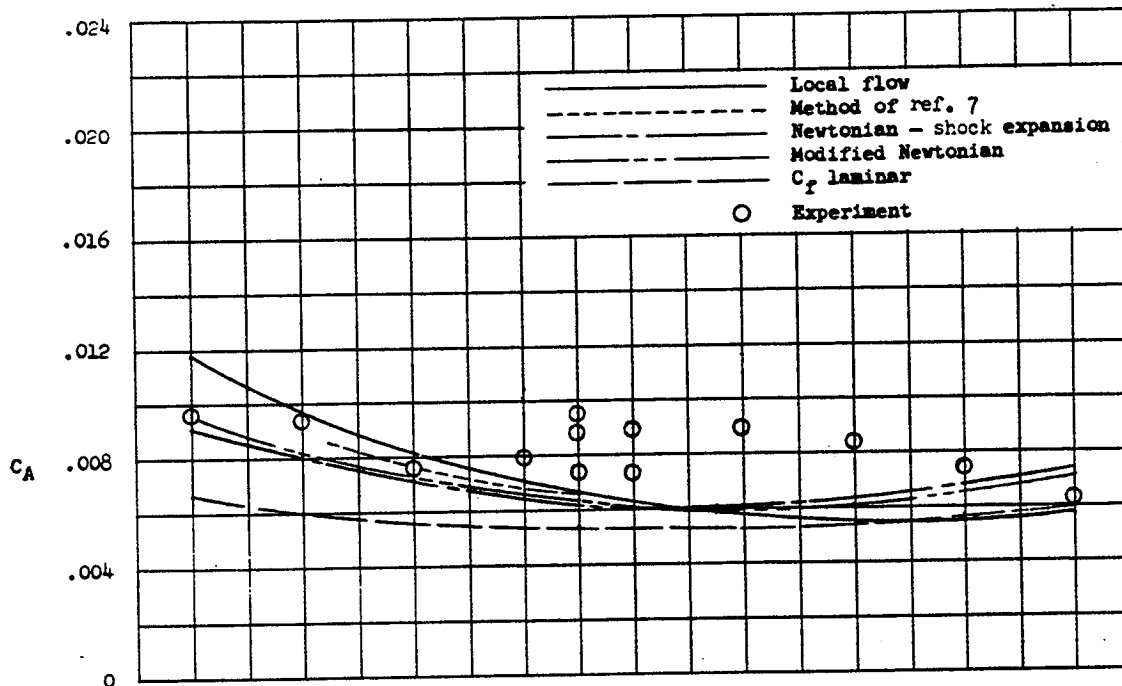
(c) Model 13 (semicone body, arrow wing). M = 6.86; R = 0.7 × 10^6.
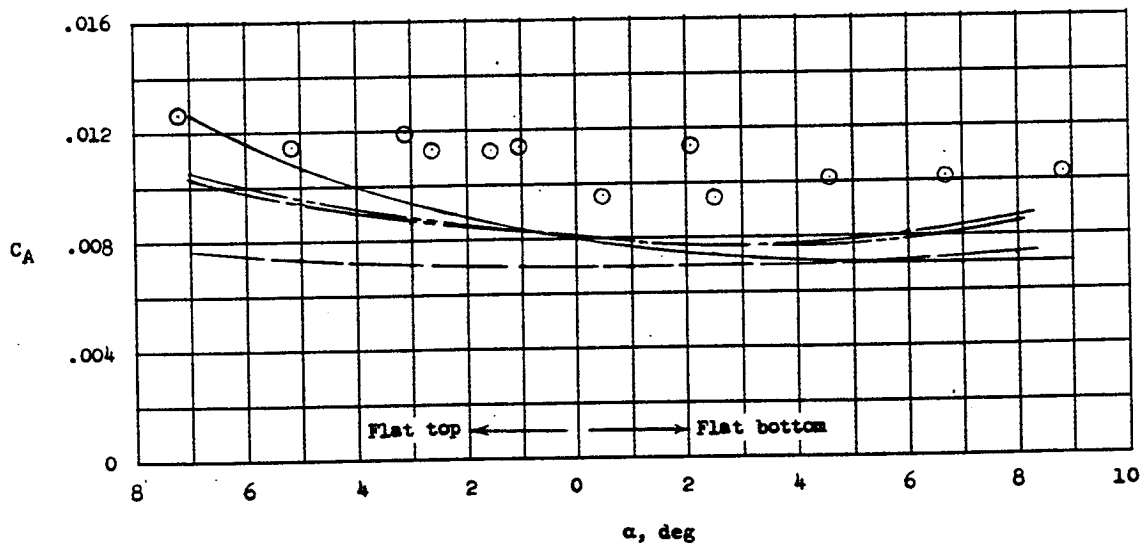
(d) Model 13 (semicone body, arrow wing). M = 9.6; R = 0.7 × 10^6.

Figure 5.- Continued.
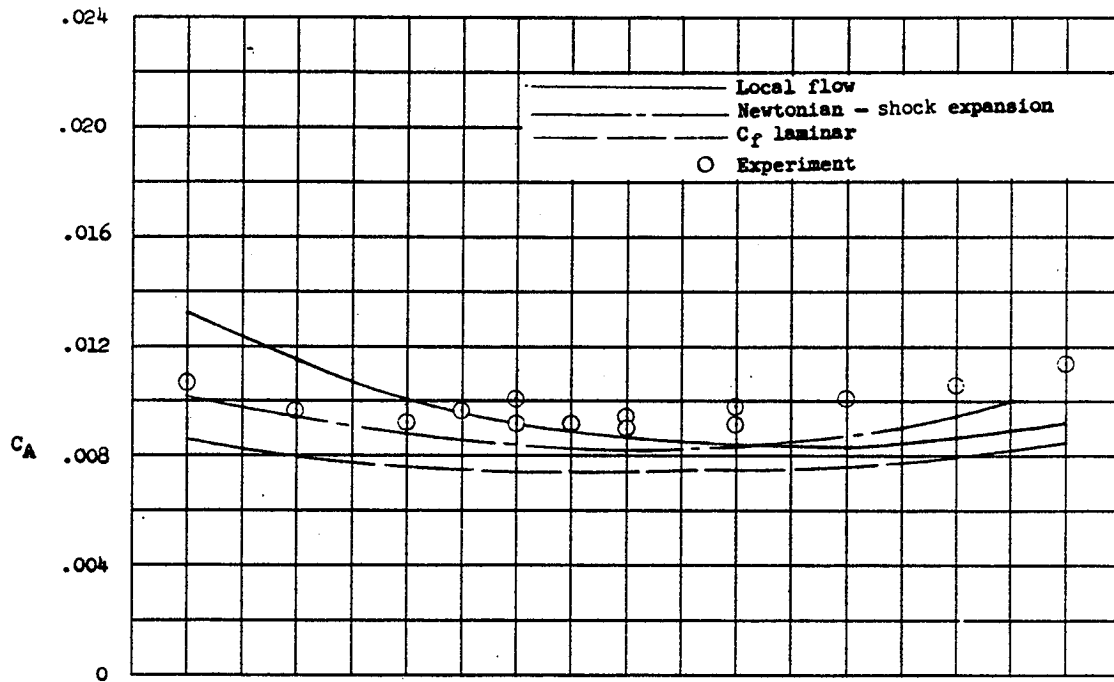
(e) Model 9 (semicone body, delta wing). M = 6.86; R = 0.36 × 10^6.
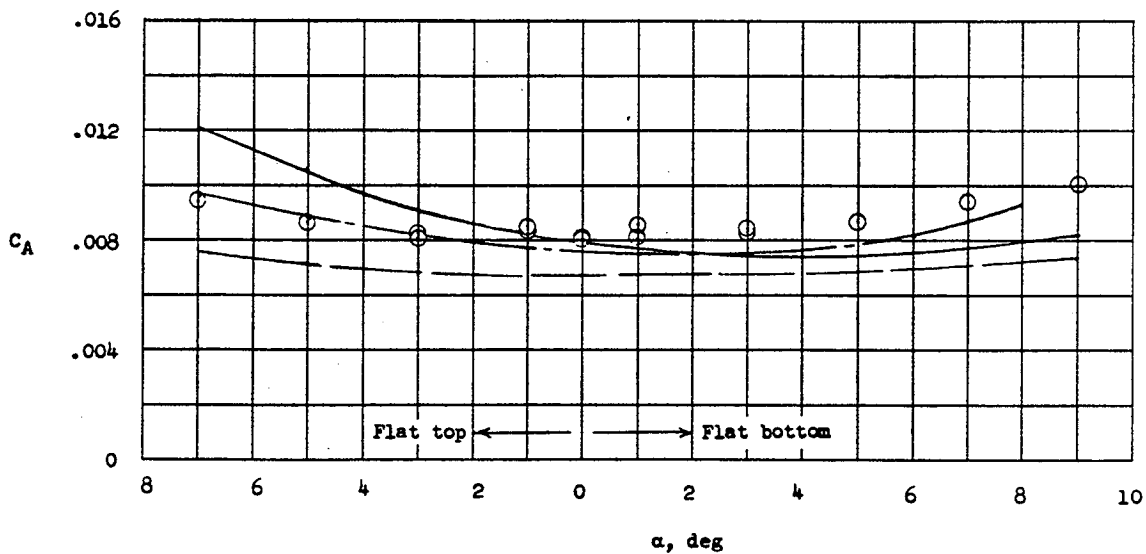
(f) Model 9 (semicone body, delta wing). M = 9.6; R = 0.7 × 10^6.

Figure 5.- Concluded.
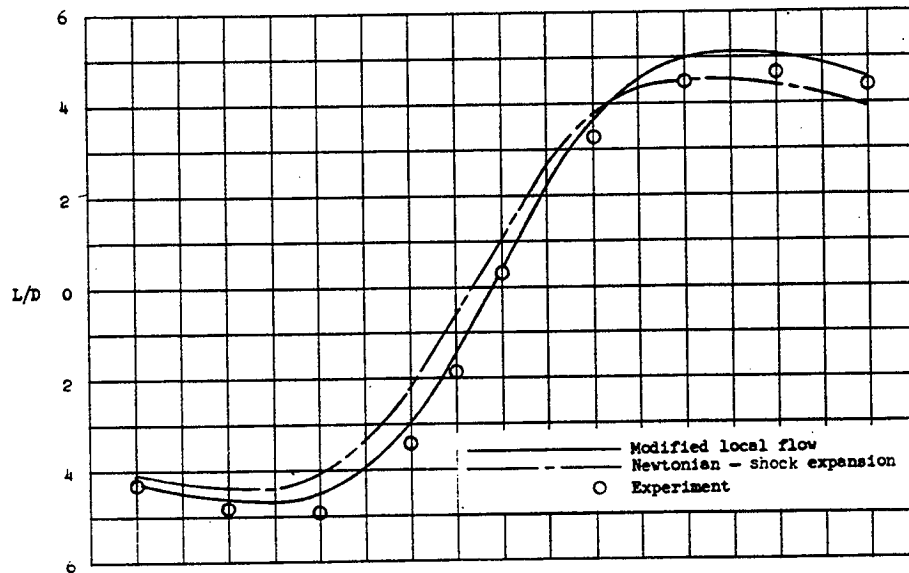
(a) Model 13 (semicone body, arrow wing). M = 6.86; R = 0.7 × 10⁶.
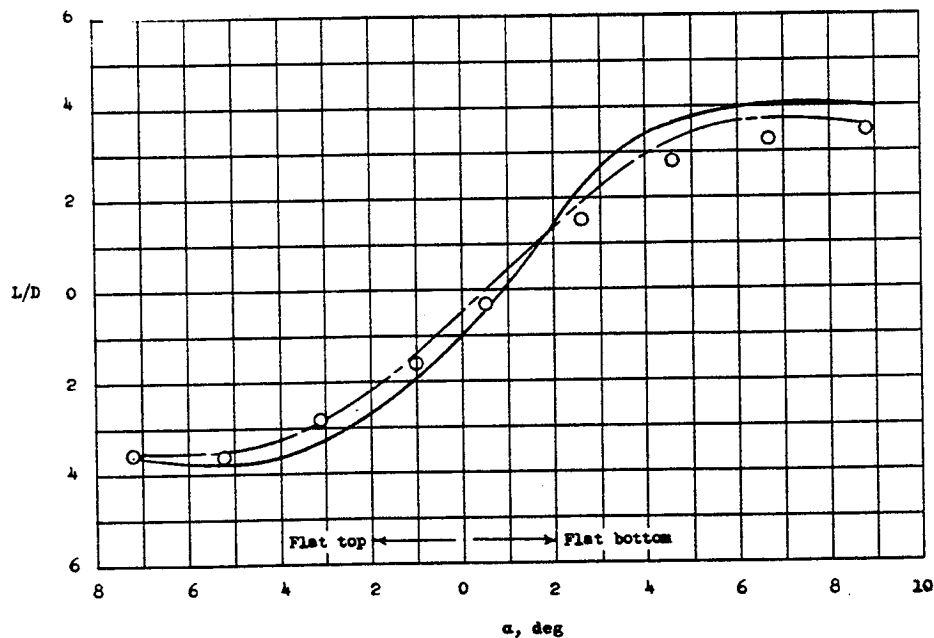
(b) Model 13 (semicone body, arrow wing). M = 9.6; R = 0.7 × 10⁶.

Figure 6.- Variation of experimental and theoretical lift-drag ratios with angle of attack.
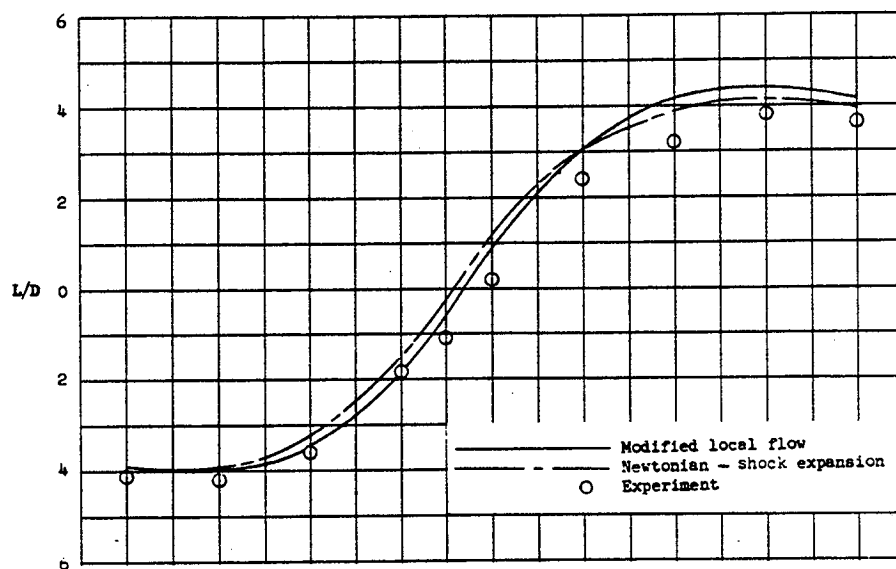
(c) Model 9 (semicone body, delta wing). M = 6.86; R = 0.36 × 10^6.
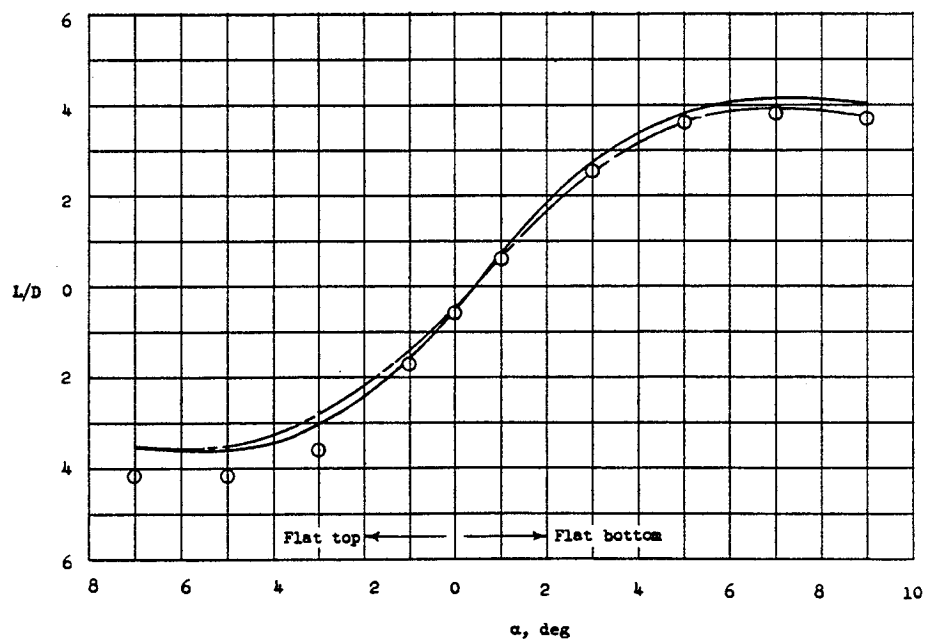
(d) Model 9 (semicone body, delta wing). M = 9.6; R = 0.7 × 10^6.

Figure 6.- Concluded.
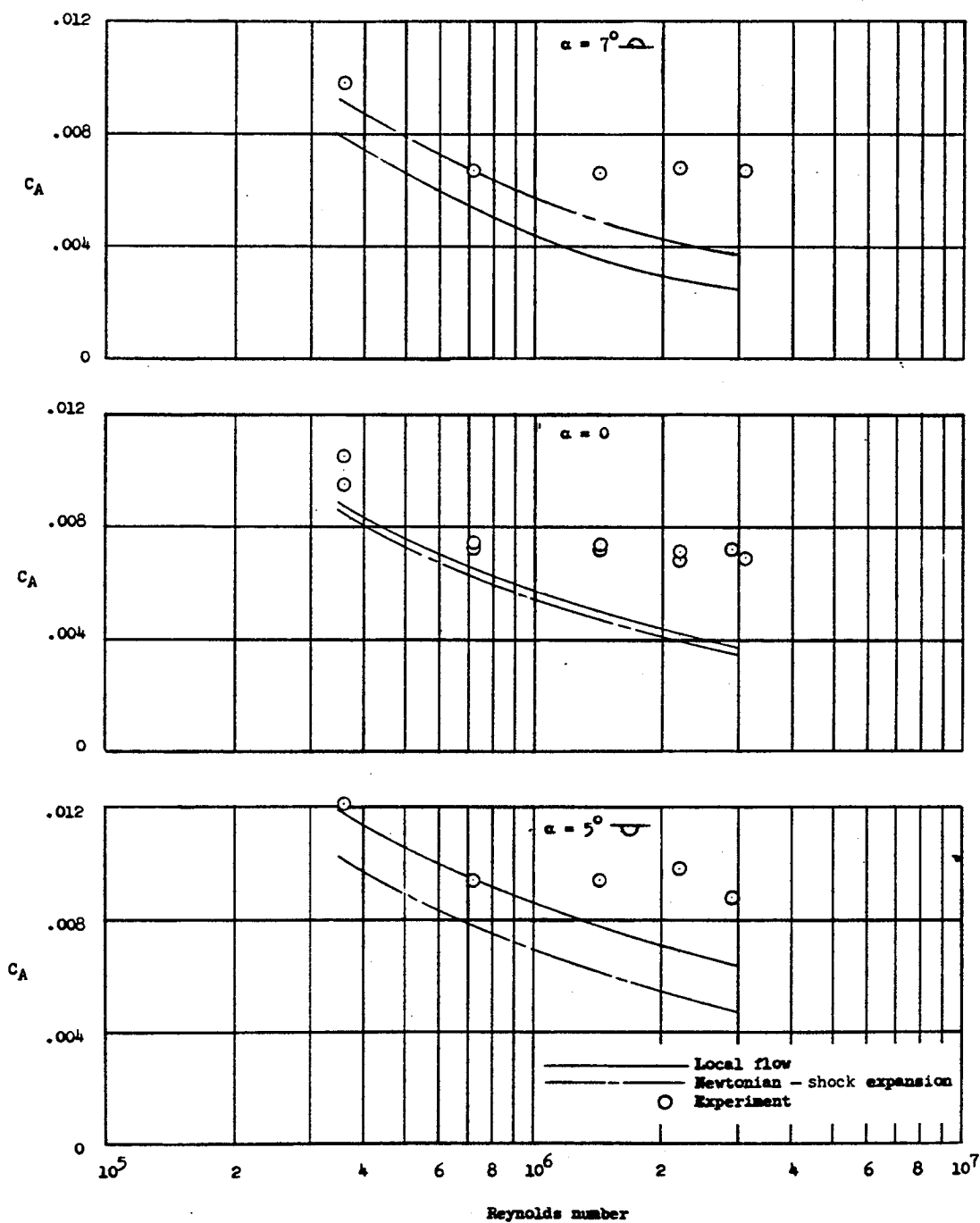
Figure 7.- Comparison of experimental and theoretical axial-force
coefficients assuming a fully laminar boundary layer for varying
Reynolds numbers. Model 13 (semicone body, arrow wing); M = 6.86.
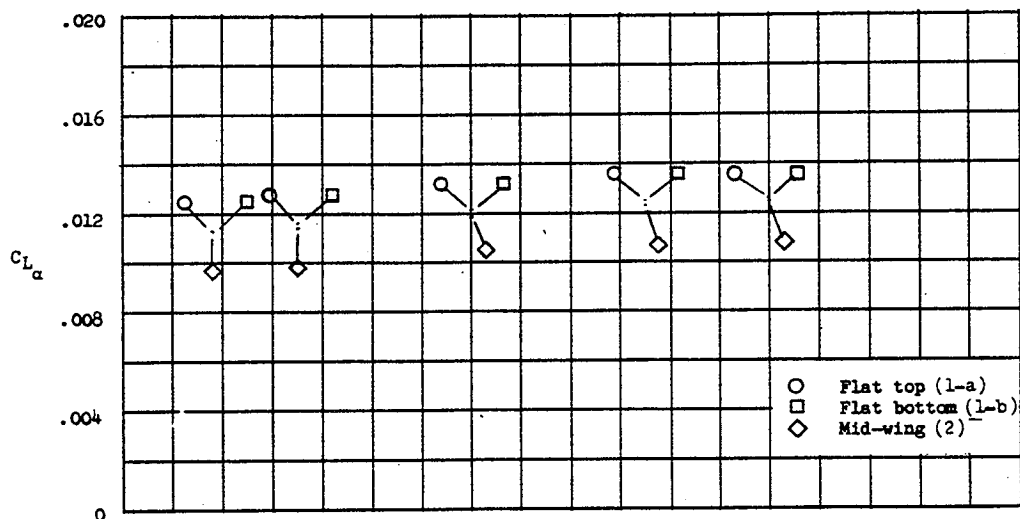
(a) C_{L_α} for models 1 and 2.
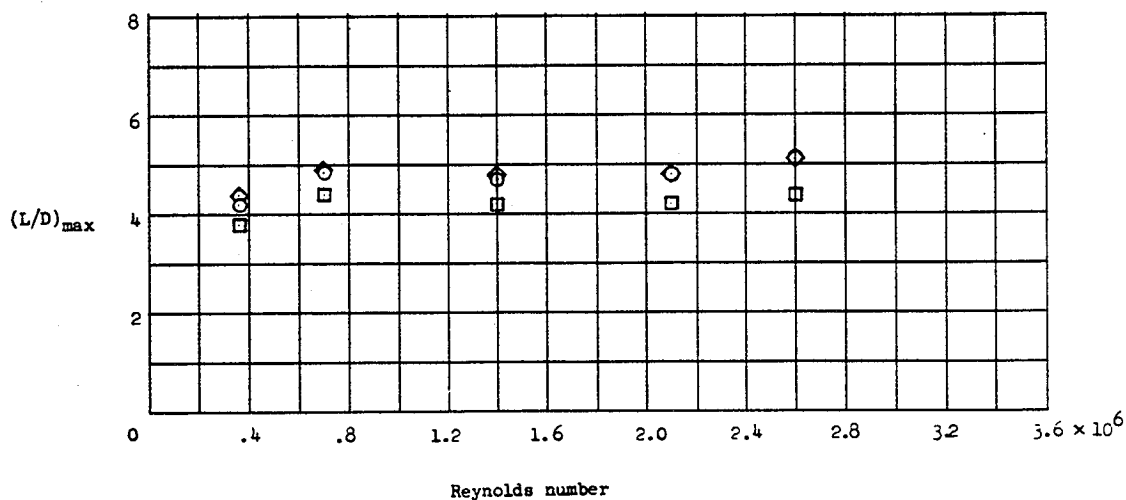
(b) $(L/D)_{max}$ for models 1 and 2.

Figure 8.- Variation of C_{L_α} and $(L/D)_{max}$ with Reynolds number for several wing-body combinations at a Mach number of 6.86.
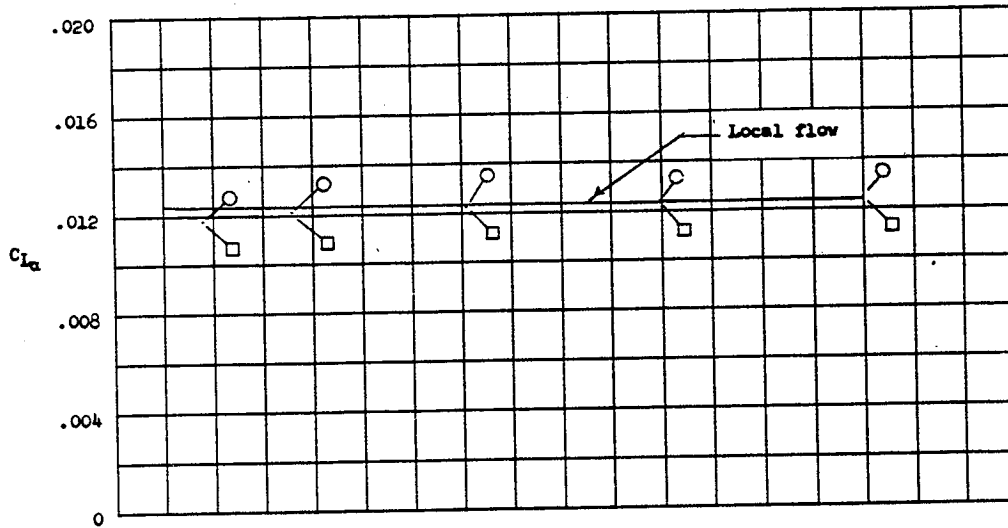
(c) C_{L_α} for model 13.
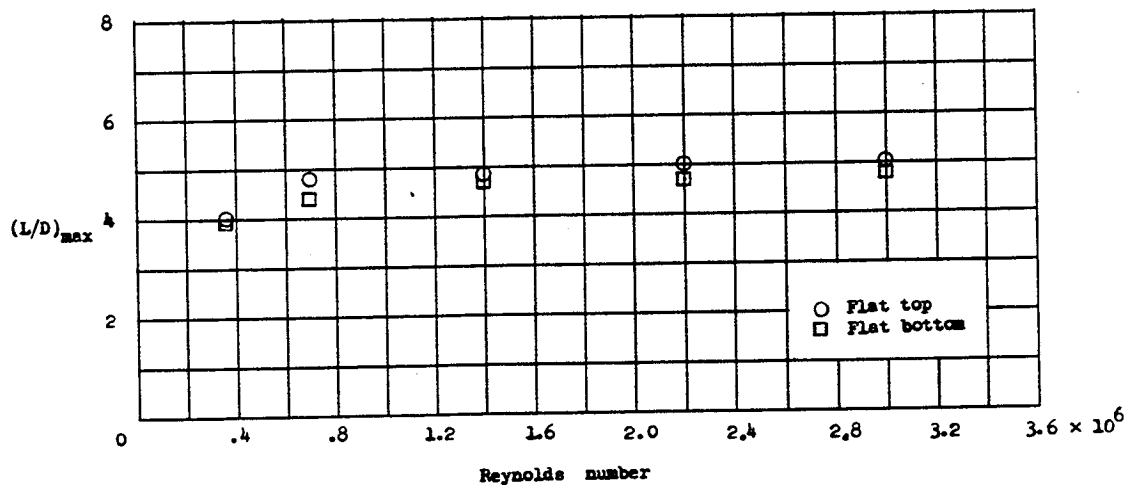
(d) $(L/D)_{max}$ for model 13.

Figure 8.- Concluded.

Flat top	Flat bottom	Mach number	Reynolds number	
♂		3.00	5.2 × 10⁶	Model 8 of ref. 6; Ames
♂		4.24	4.6	
♂		5.05	2.3	10 × 14 super- sonic tunnel
♂		6.28	1.0	
O	□	6.86	2.1	Langley 11-inch HT (air)
O	□	9.6	.7	Langley 11-inch
O	□	10.5	1.6	hypersonic
O	□	13.0	2.8	tunnel (helium)
O	□	17.8	3.4	

(a) Model 1 (3/4-power body, clipped arrow wing).

Flat top	Flat bottom	Mach number	Reynolds number	
O	□	2.91	0.7 × 10⁶	Langley 9-inch supersonic tunnel
●	■	2.91	5.6	
♂		3.00	5.6	Plan form A of ref. 4; Ames
♂		4.24	5.1	
♂		5.05	2.5	10 × 14 super- sonic tunnel
♂		6.28	1.1	
O	□	6.86	0.7	Langley 11-inch hypersonic tunnel
O	□	9.60	0.7	

Modified local flow
Modified local flow
Newtonian — Shock expansion

Mach number

(b) Model 13 (semicone body, arrow wing).

Figure 9.- Variation of $(L/D)_{max}$ with Mach number.
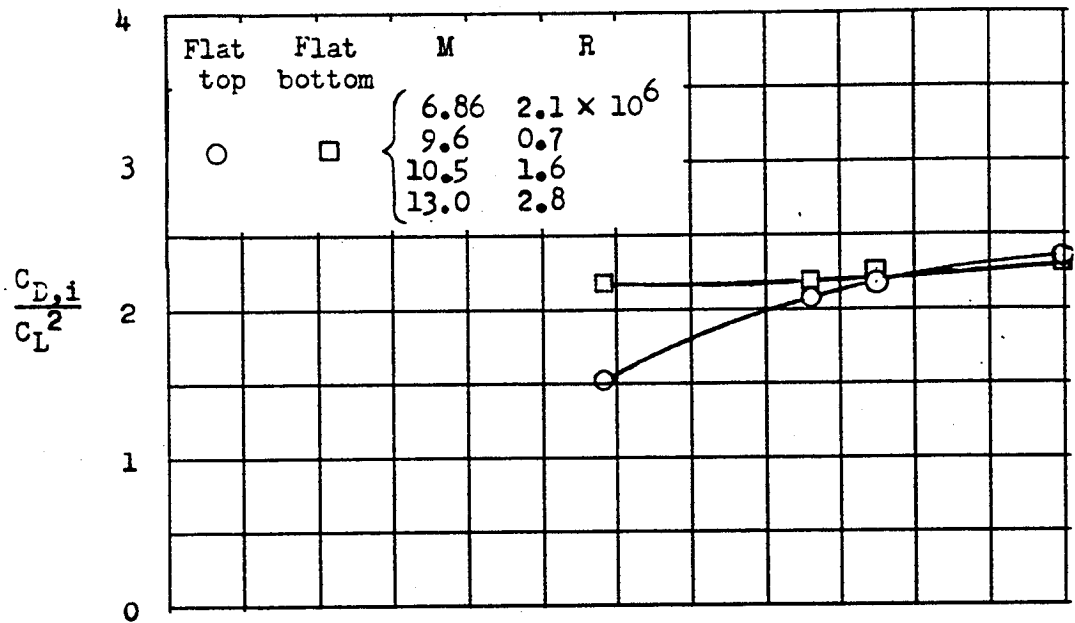
(a) Model 1 (3/4-power body, clipped arrow wing). $C_L = 0.06$.
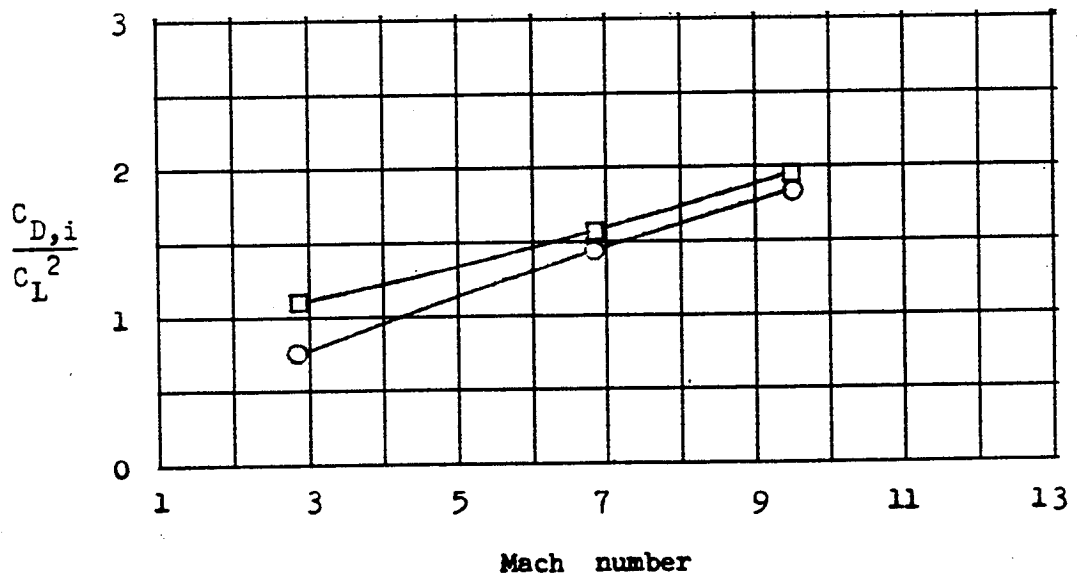
Mach number

(b) Model 13 (semicone, arrow wing). $R = 0.7 \times 10^6$; $C_L = 0.08$.

Figure 10.- Variation of the faired experimental value of $C_{D,i}/C_L^2$ with Mach number for $(L/D)_{max}$.
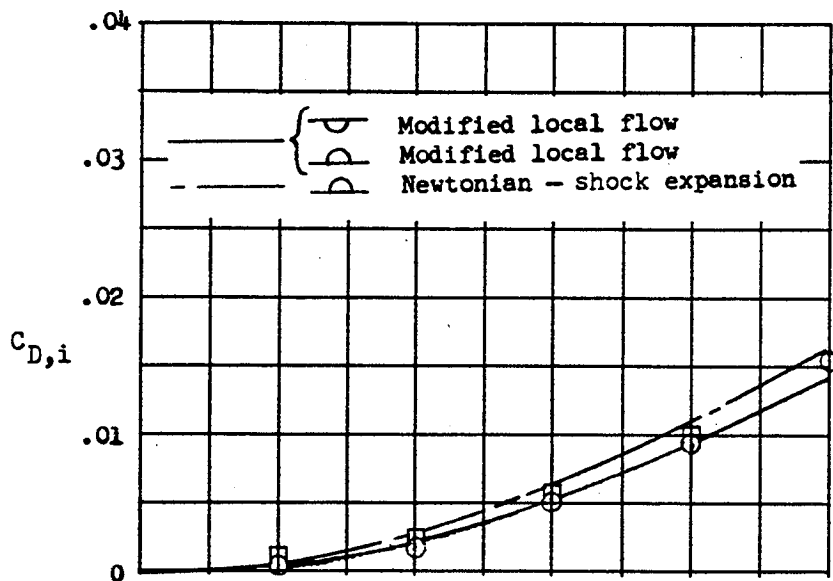
(a) M = 6.86.
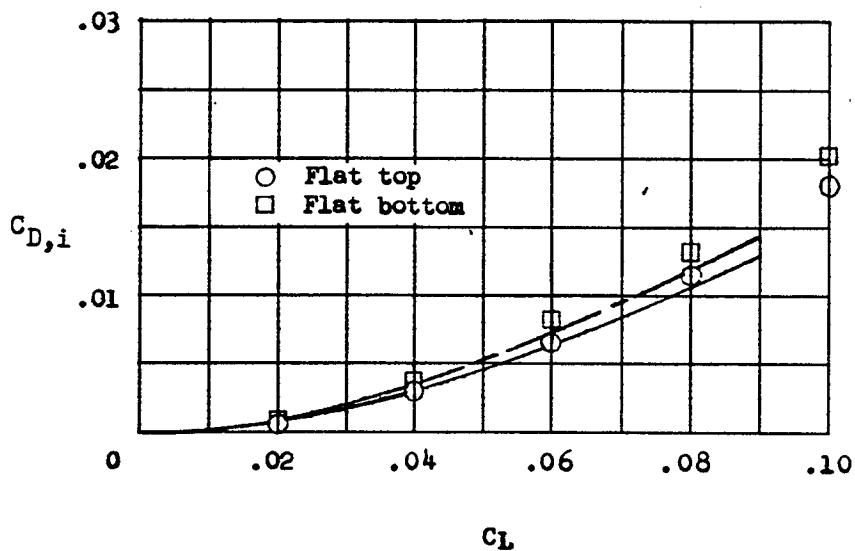
(b) M = 9.6.

Figure 11.- Comparison of the faired experimental values of $C_{D,i}$ with those calculated theoretically from the expression $C_{D,i} = C_L \tan \alpha_e$ for model 13 (semicone body, arrow wing). R = 0.7 × 10^6.
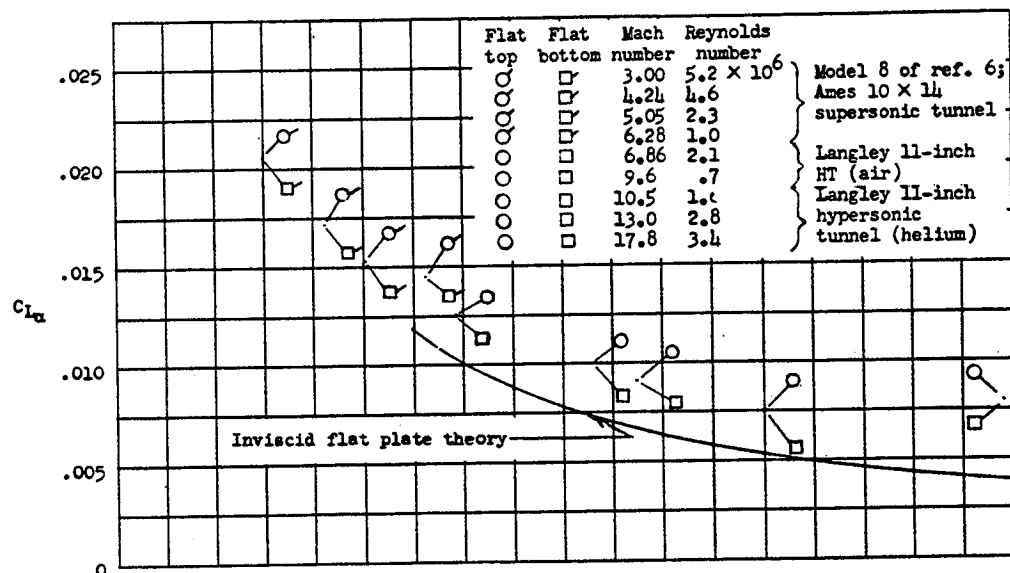
(a) Model 1 (3/4-power body, clipped arrow wing).
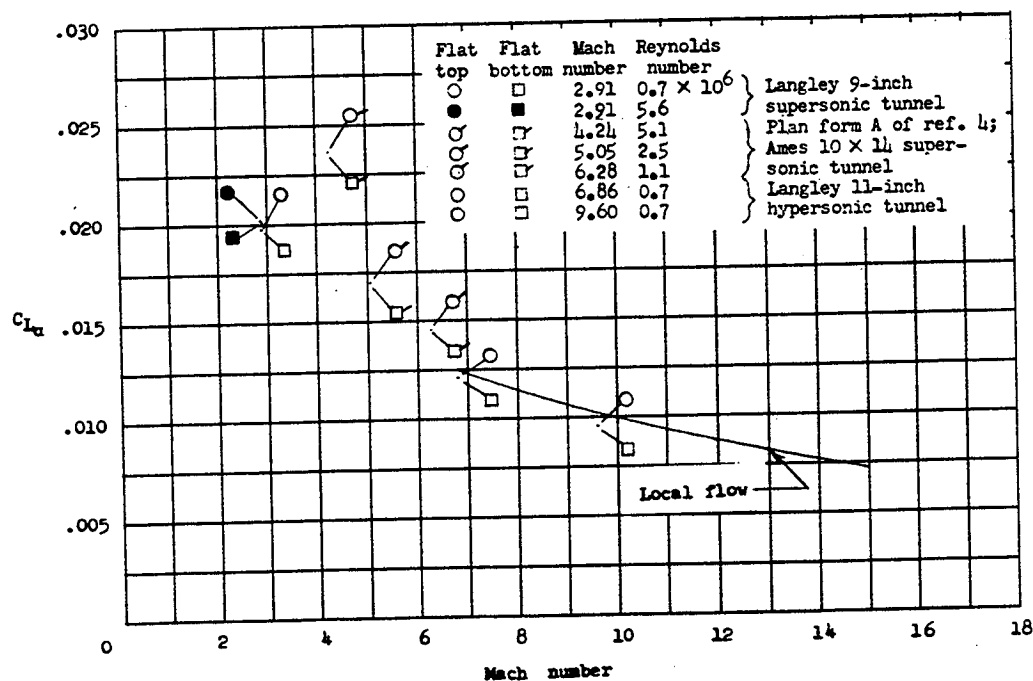
(b) Model 13 (semicone body, arrow wing).

Figure 12.- Variation of C_{L_α} with Mach number.

Model sketch	Body position	No.	$R \times 10^{-6}$	$(L/D)_{max}$	C_{L_α}
		1-a	0.7	4.8	0.0116
			2.1	4.8	.0125
		2	0.7	4.9	.0114
			2.1	4.8	.0123
		1-b	0.7	4.4	.0116
			2.1	4.2	.0125
		3-a	0.7	4.2	.0115
			2.1	4.6	.0118
		4	0.7	4.3	.0104
			2.1	4.5	.0120
		3-b	0.7	3.9	.0115
			2.1	4.1	.0112
		5-a	0.7	4.0	.0107
			2.1	4.5	.0112
		6	0.7	4.4	.0105
			2.1	4.4	.0120
		5-b	0.7	3.6	.0107
			2.1	3.8	.0118
		10-a	1.3	4.8	.0114
		10-b	1.3	4.3	.0114
		14-a	1.3	5.4	.0105
		14-b	1.3	5.2	.0105

Figure 13.- Effect of body orientation on $(L/D)_{max}$ and C_{L_α} for several wing-body combinations at a Mach number of 6.86.

.04

.02

$C_{L,\alpha=0}$ 0

Local flow

-.02

-.04
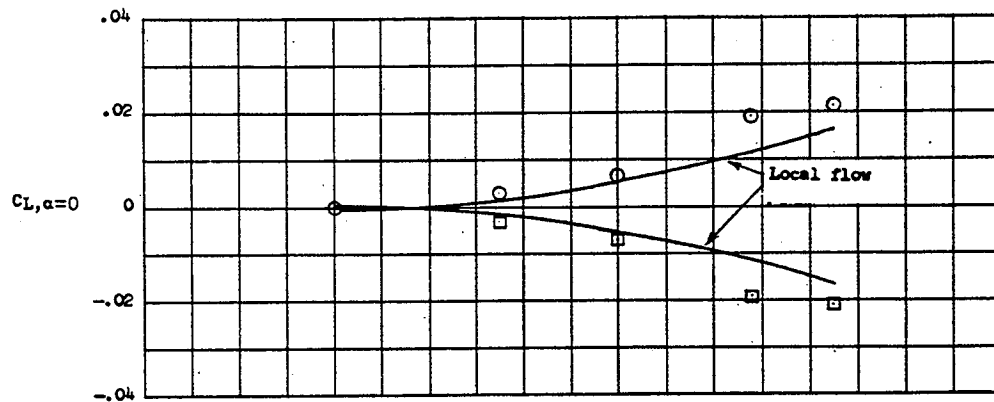
(a) Variation in C_L at $\alpha = 0$ with wing sweep.

.016

c_{L_α} .012

Local flow

.008
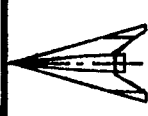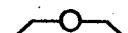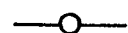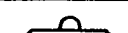
(b) Variation in C_{L_α} with wing sweep.

6

4

$(L/D)_{max}$

2

O Flat top
□ Flat bottom

0

52   56   60   64   68   72   76   80   84   88

$\wedge$, deg
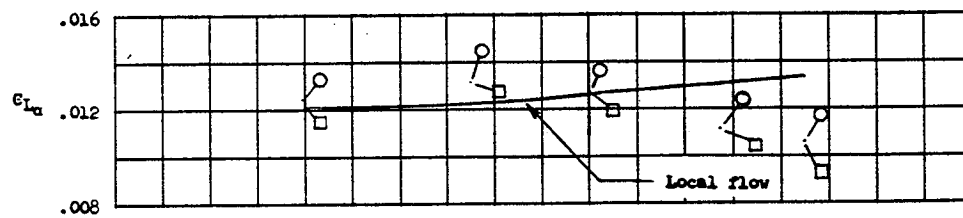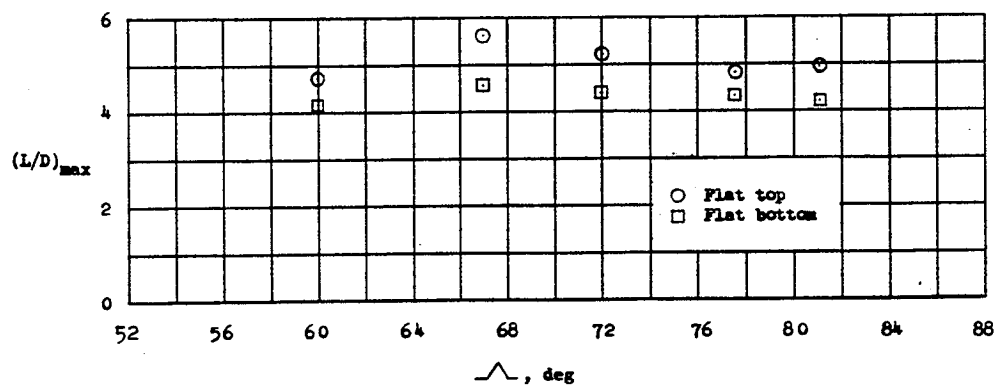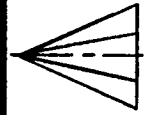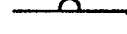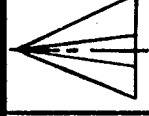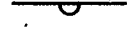
(c) Variation in $(L/D)_{max}$ with wing sweep.

Figure 14.- Effects of variation in wing leading-edge sweep on the lift-
drag characteristics for a given body in combination with a series of
delta wings (models 7 to 11). $M = 6.86$; $R = 1.3 \times 10^6$.

Figure 15.- Variation in axial-force coefficient with angle of attack for two flat-top and flat-bottom configurations with different wing leading-edge sweep. $M = 6.86$; $R = 1.3 \times 10^6$.

Model sketch	Body position	No.	$R \times 10^{-6}$	$(L/D)_{max}$	C_{L_α}
		3-a	0.7	4.2	0.0115
			2.1	4.6	.0118
		1-a	0.7	4.8	.0116
			2.1	4.8	.0125
		5-a	0.7	4.0	.0107
			2.1	4.5	.0112
		4	0.7	4.3	.0104
			2.1	4.5	.0120
		2	0.7	4.9	.0114
			2.1	4.8	.0123
		6	0.7	4.4	.0105
			2.1	4.4	.0120
		3-b	0.7	3.9	.0115
			2.1	4.1	.0112
		1-b	0.7	4.4	.0116
			2.1	4.2	.0125
		5-b	0.7	3.6	.0107
			2.1	3.8	.0118

(a) Effects of wingtip deflection.

Model sketch	Body position	No.	$(L/D)_{max}$	C_{L_α}
		12-a	3.8	0.0133
		12-b	3.9	.0133
		9-a	5.1	.0123
		9-b	4.4	.0123
		10-a	4.8	.0114
		10-b	4.3	.0114
		14-a	5.4	.0105
		14-b	5.2	.0105
		15-a	5.8	.0098
		15-b	5.2	.0098

(b) Effects of model geometry.
$R = 1.3 \times 10^6$.

Figure 16.- Effects of wingtip deflection and model geometry on $(L/D)_{max}$ and C_{L_α} for several wing-body combinations at a Mach number of 6.86.
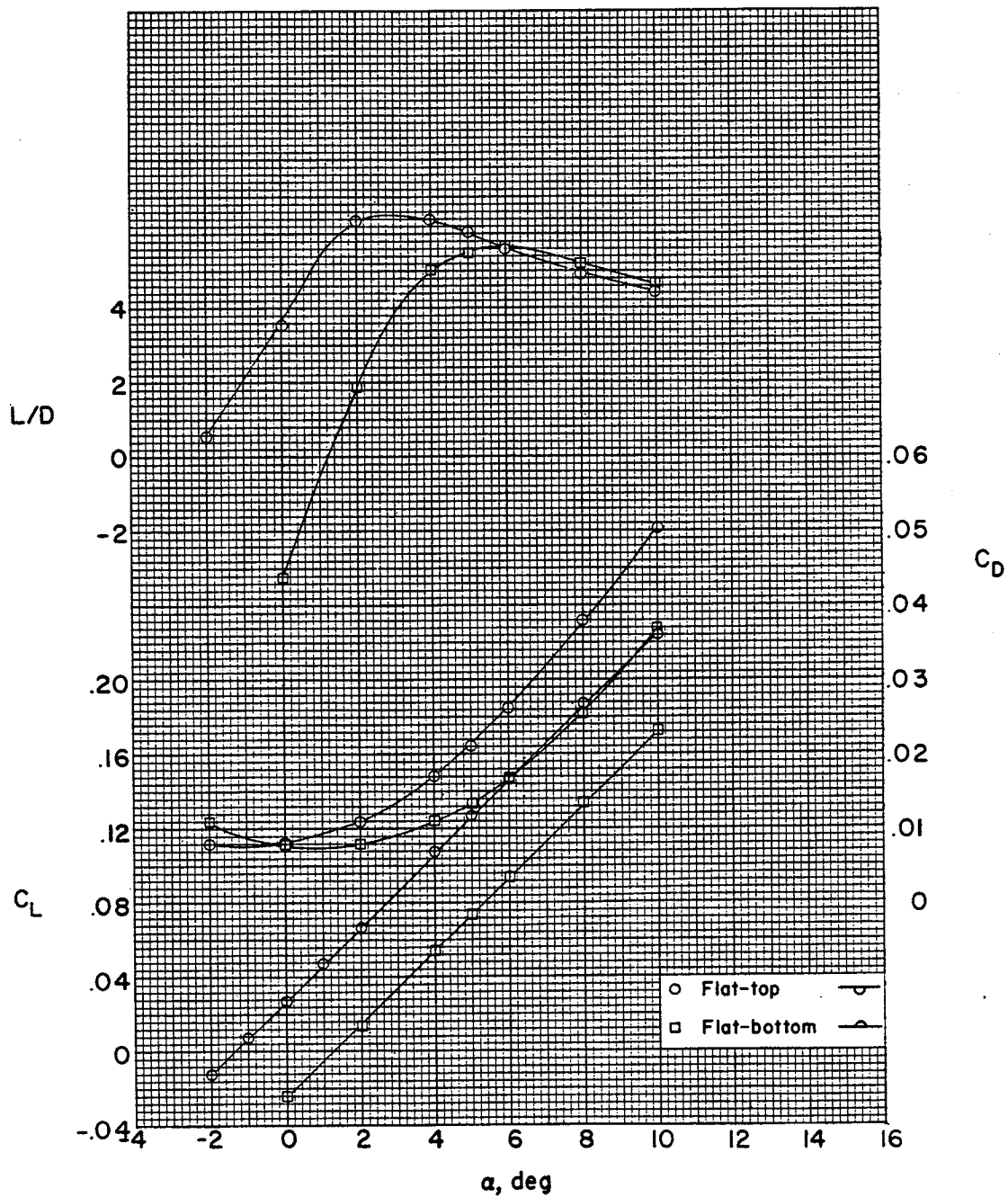
(a) R = 0.7 × 10^6.

Figure 17.- Longitudinal aerodynamic characteristics of model 13.
M = 2.91 in air.
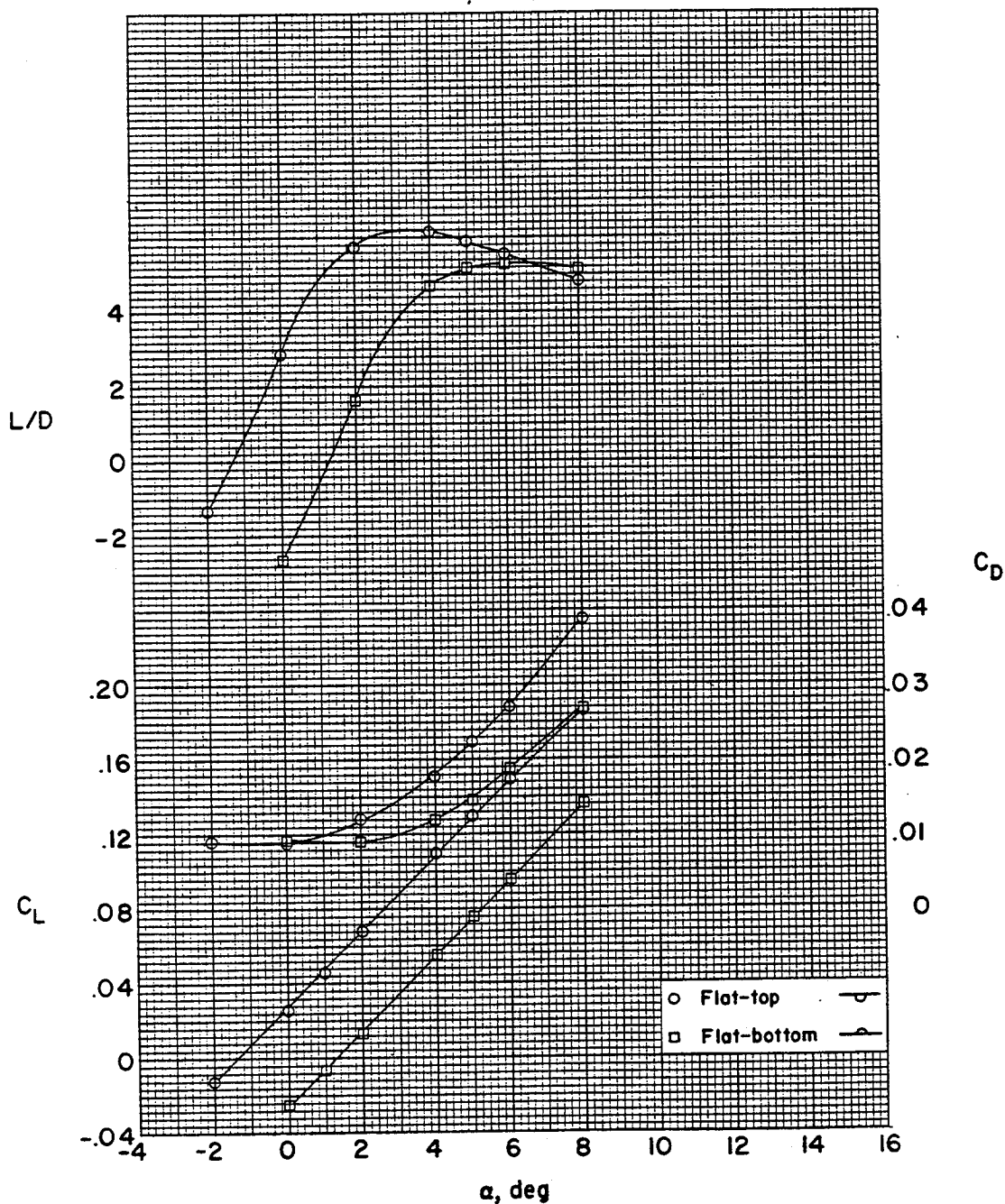
(b) $R = 5.6 \times 10^6$.
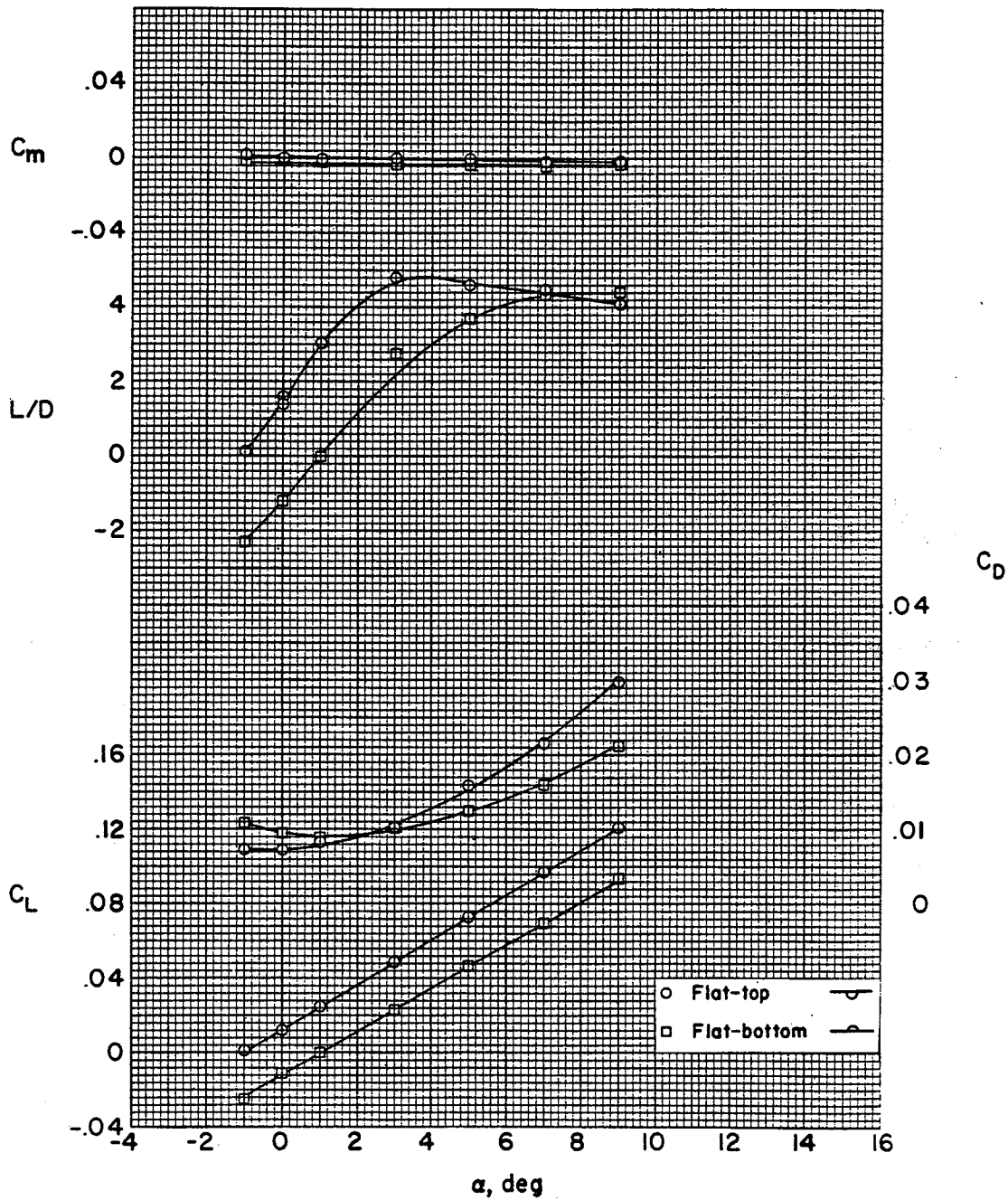
Figure 17.- Concluded.
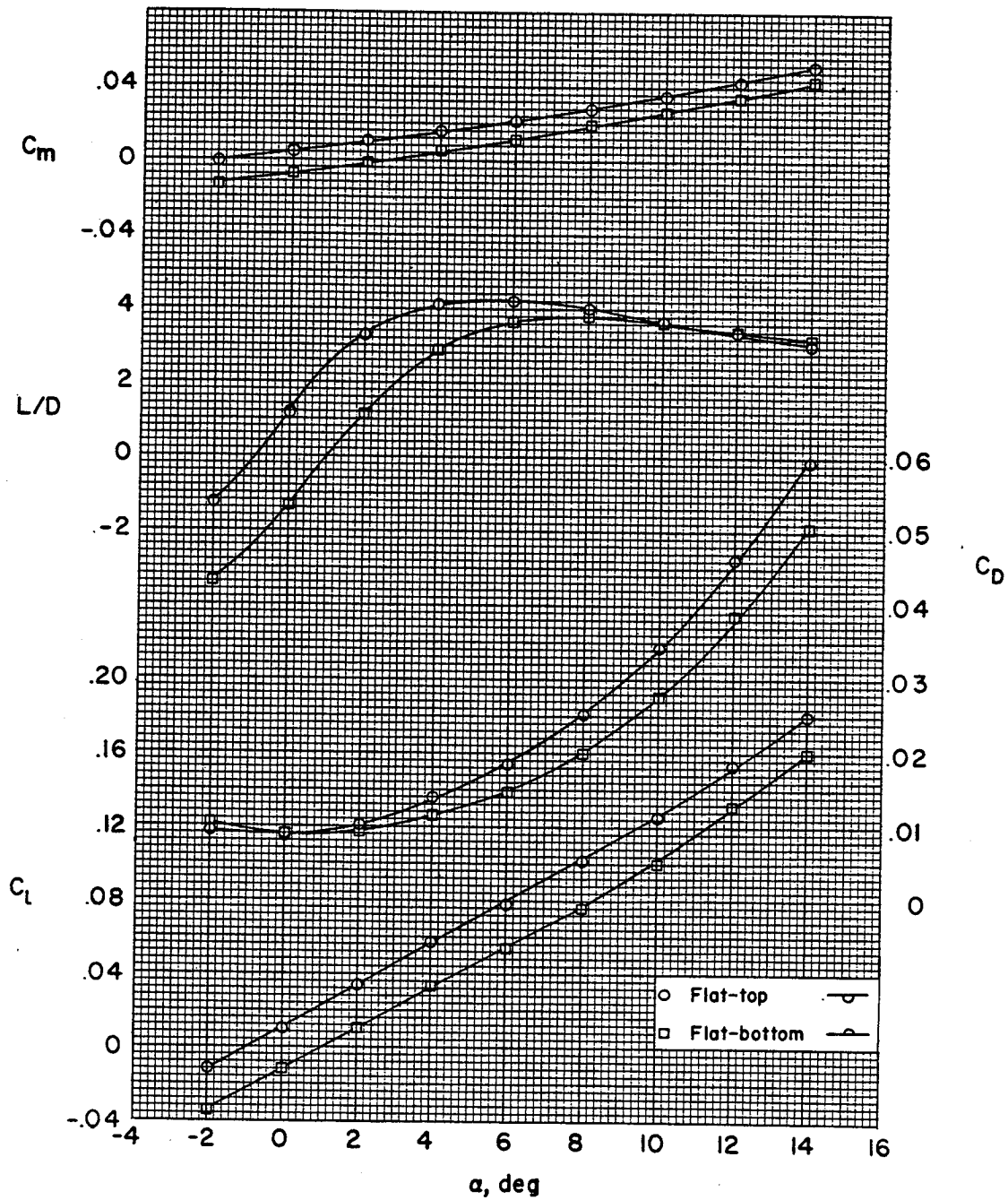
(a)   R = 0.36 × 10^6.

Figure 18.- Longitudinal aerodynamic characteristics of model 1.
M = 6.86   in air.
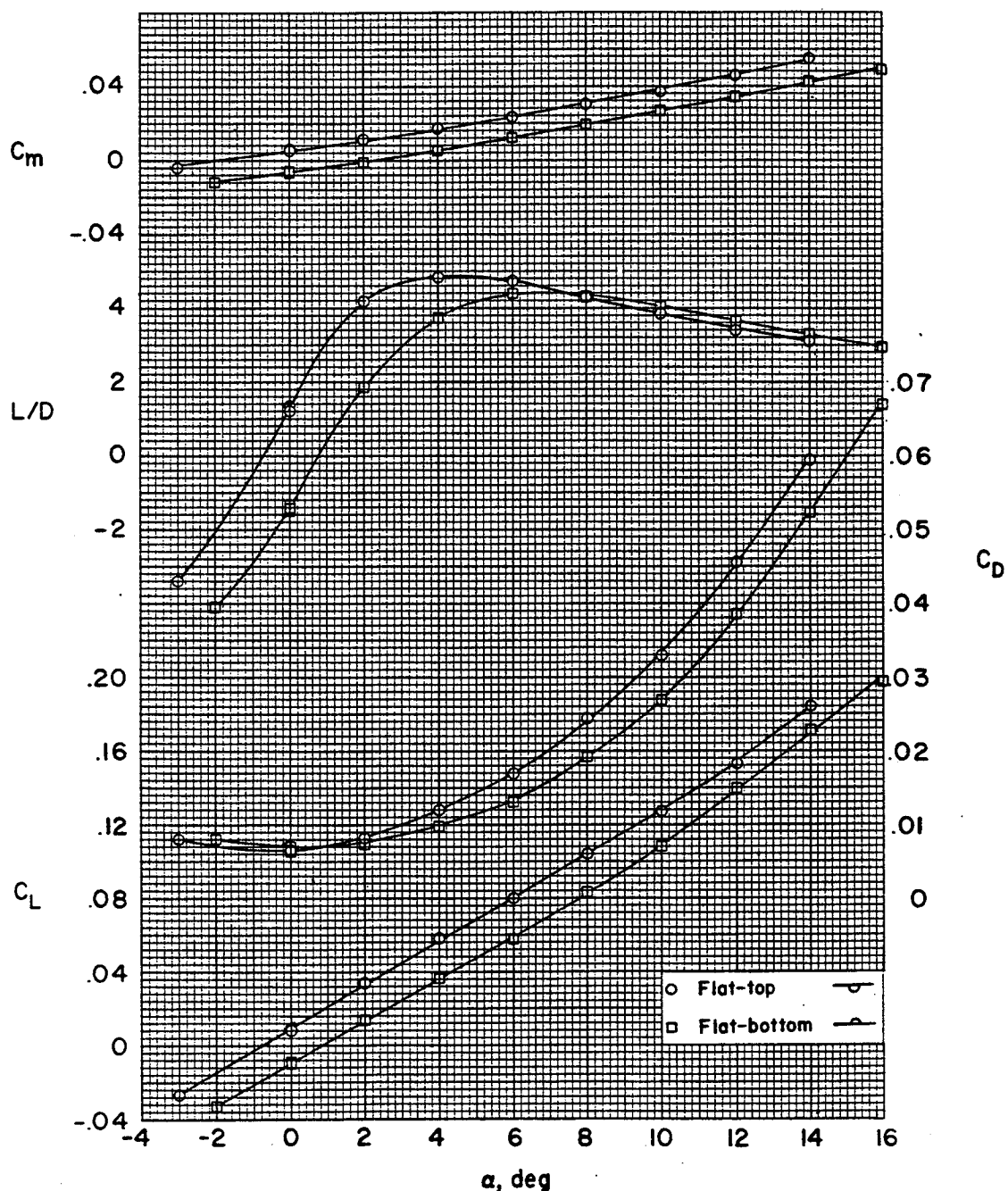
(b) R = 0.7 × 10^6.
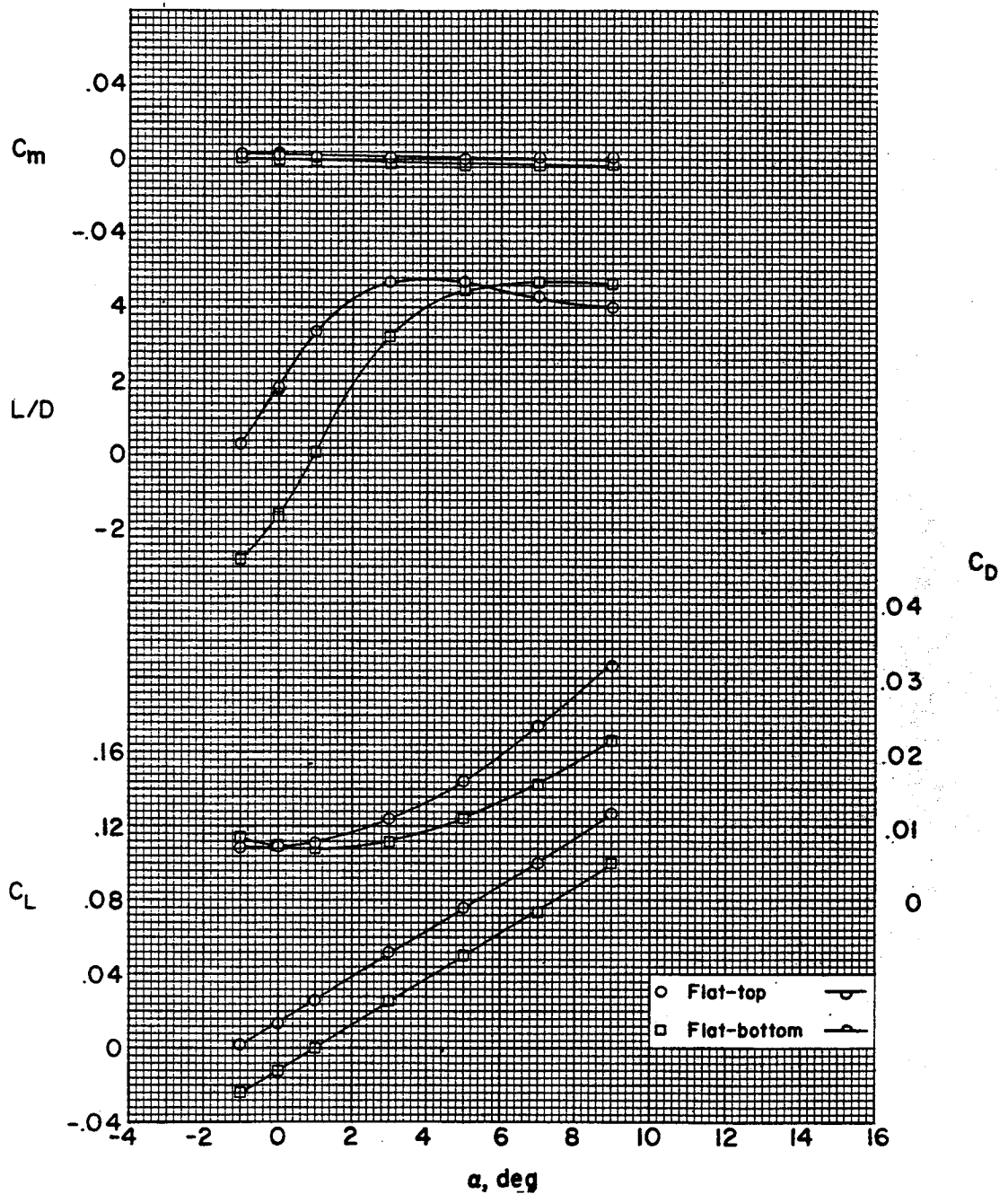
Figure 18.- Continued.
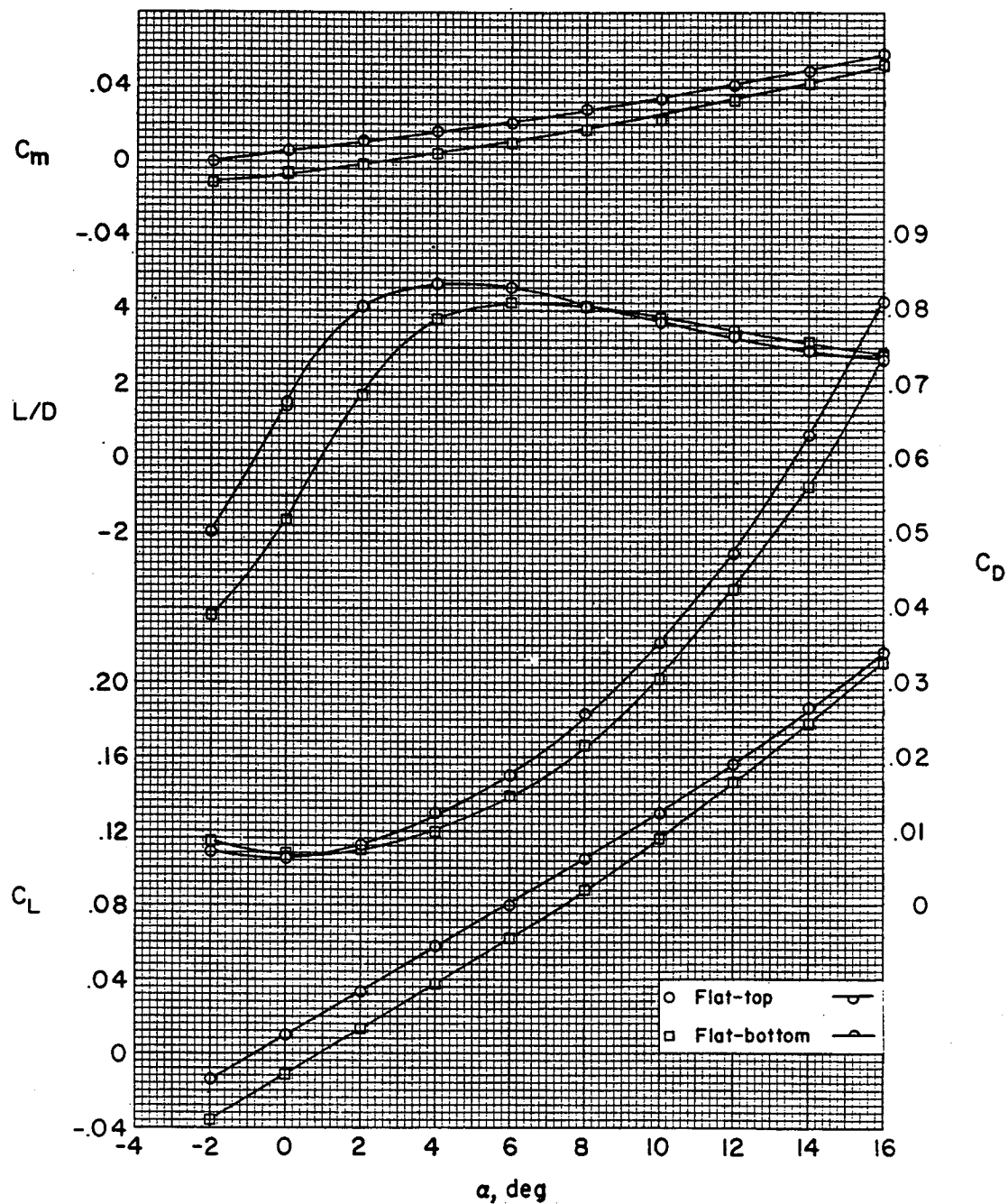
(c) R = 1.4 × 10⁶.

Figure 18.- Continued.

(d) $R = 2.1 \times 10^6$.

Figure 18.- Continued.

L-747
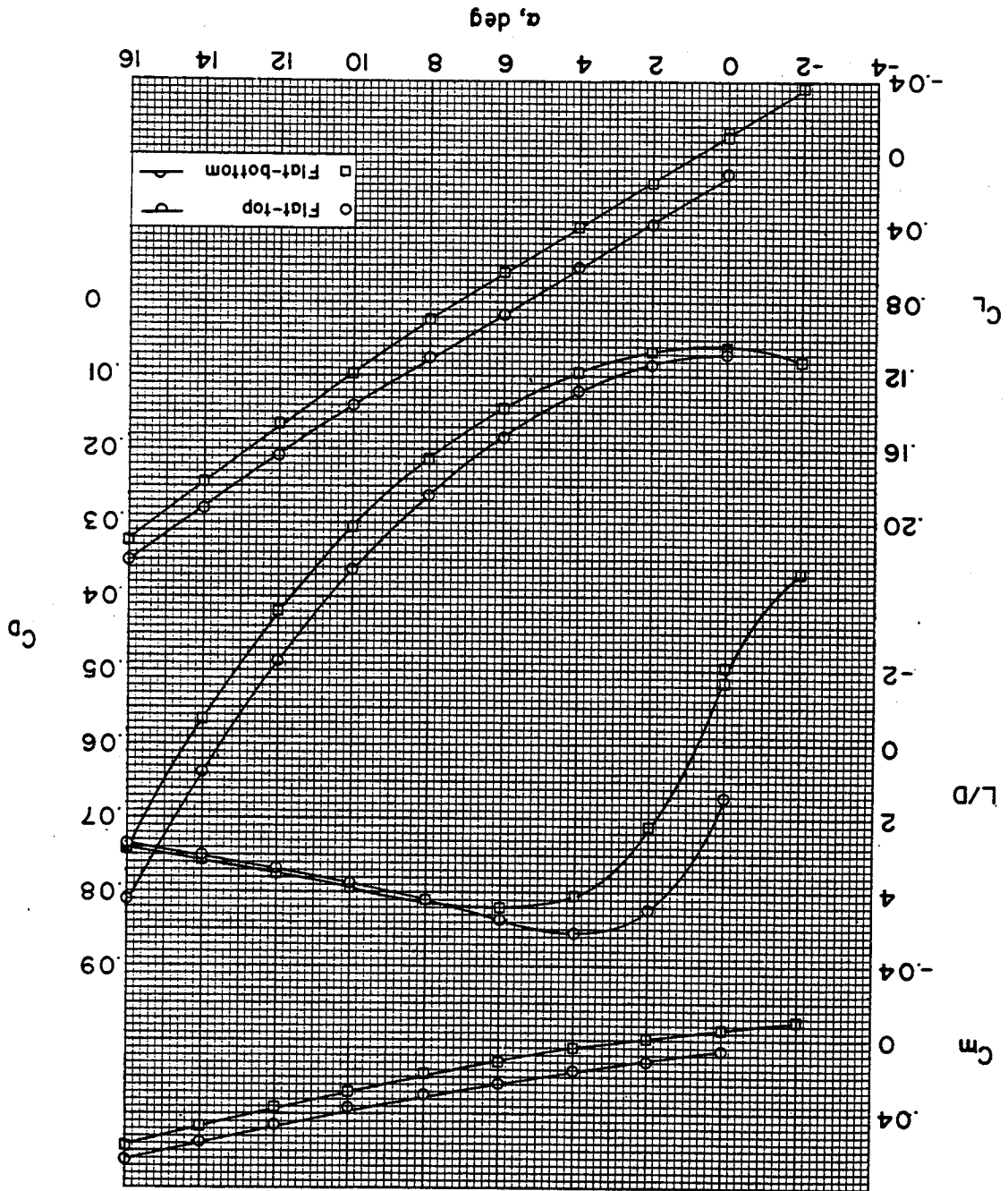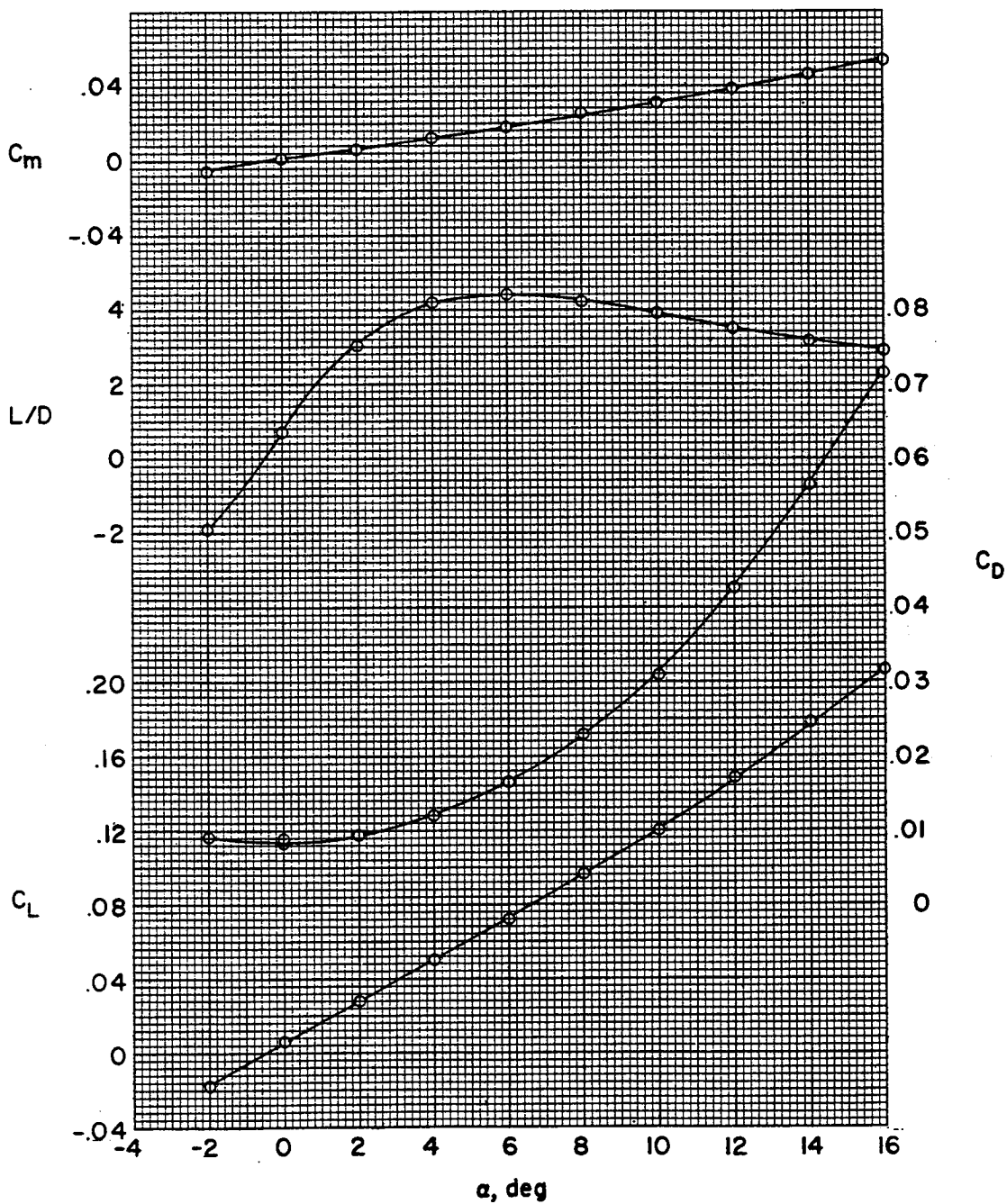
(a) R = 0.36 x 10⁶.

Figure 19.- Longitudinal aerodynamic characteristics of model 2.
M = 6.86 in air.
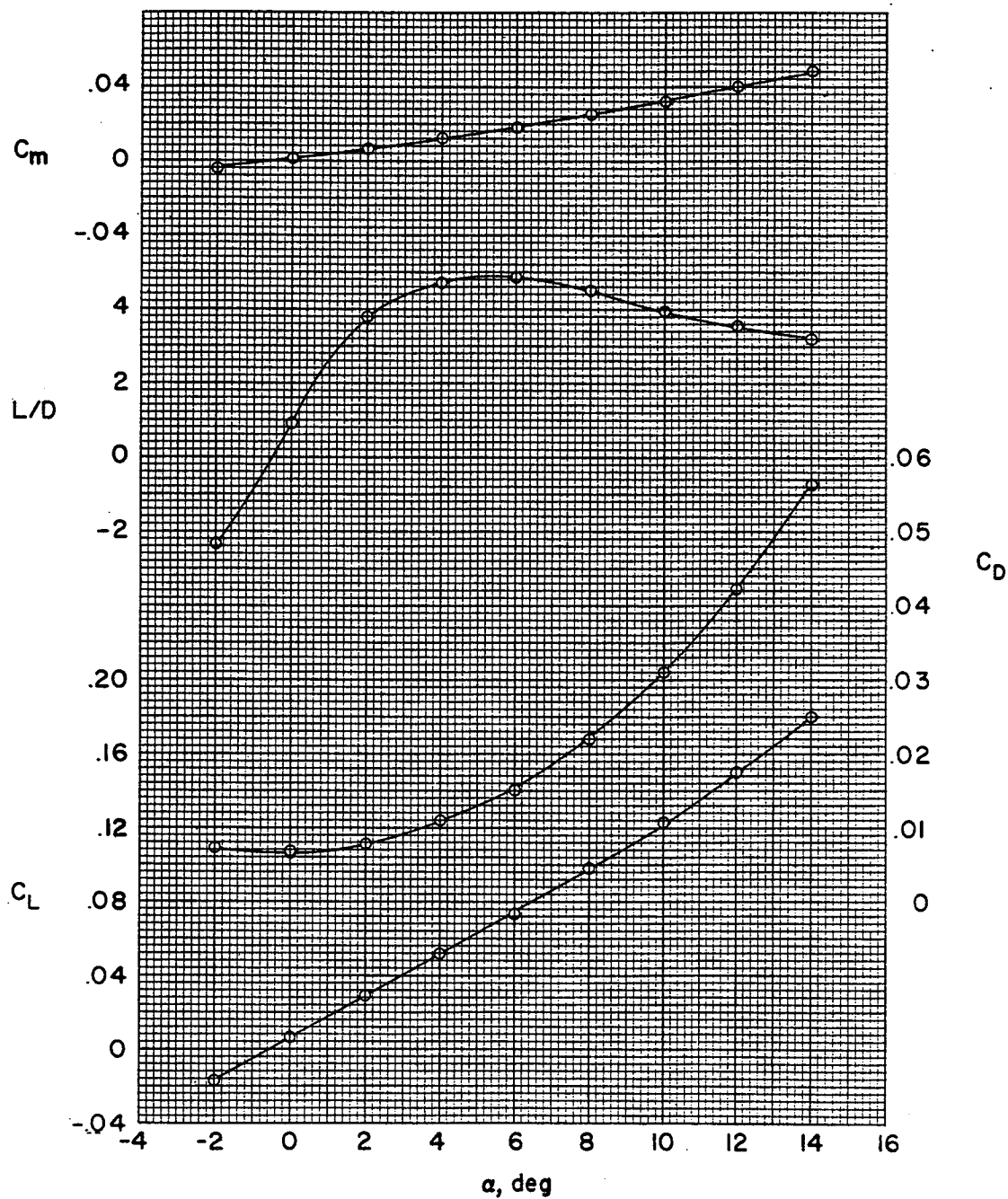
(b) R = 0.7 × 10^6.

Figure 19.- Continued.
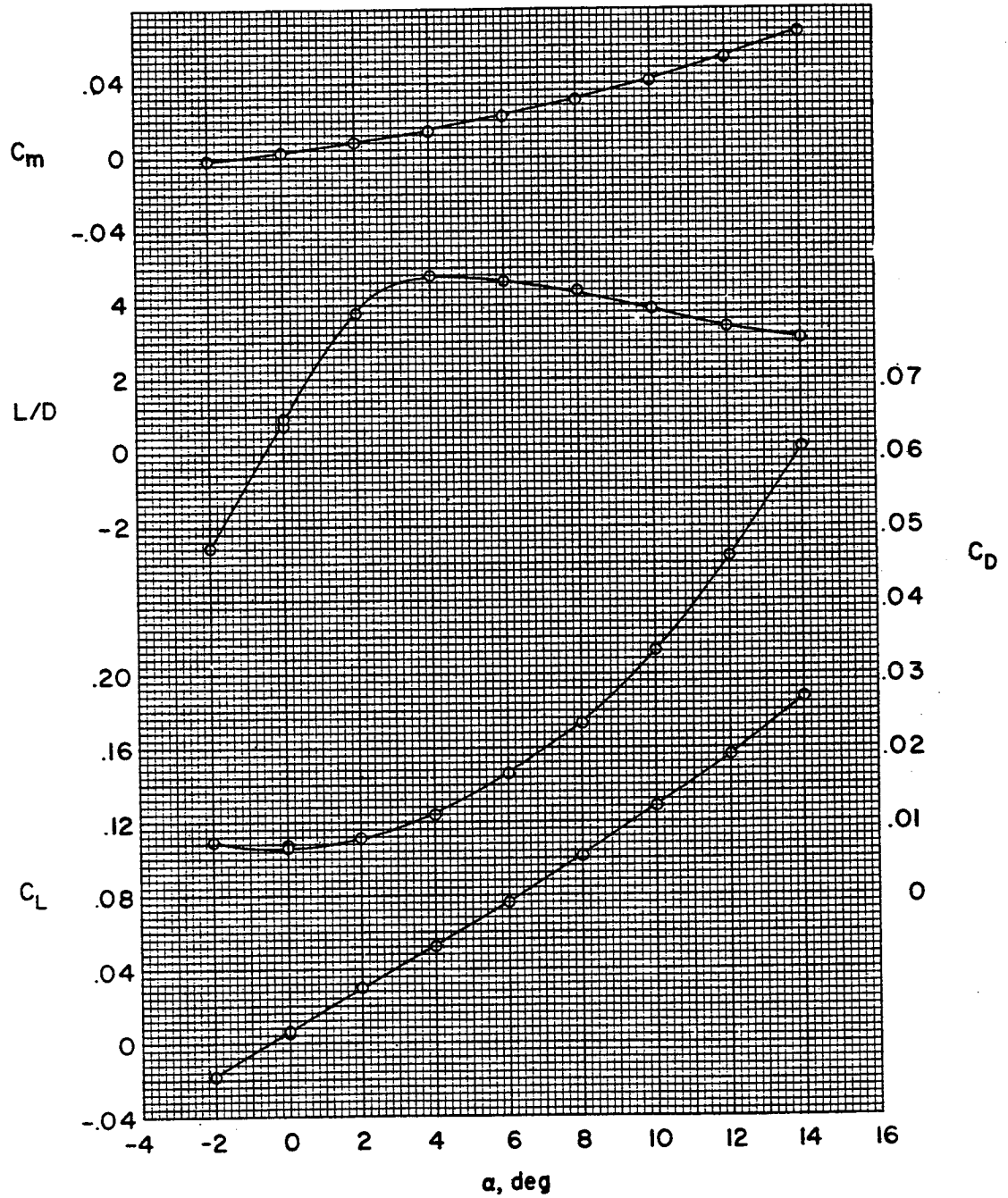
(c) R = 1.4 × 10^6.

Figure 19.- Continued.
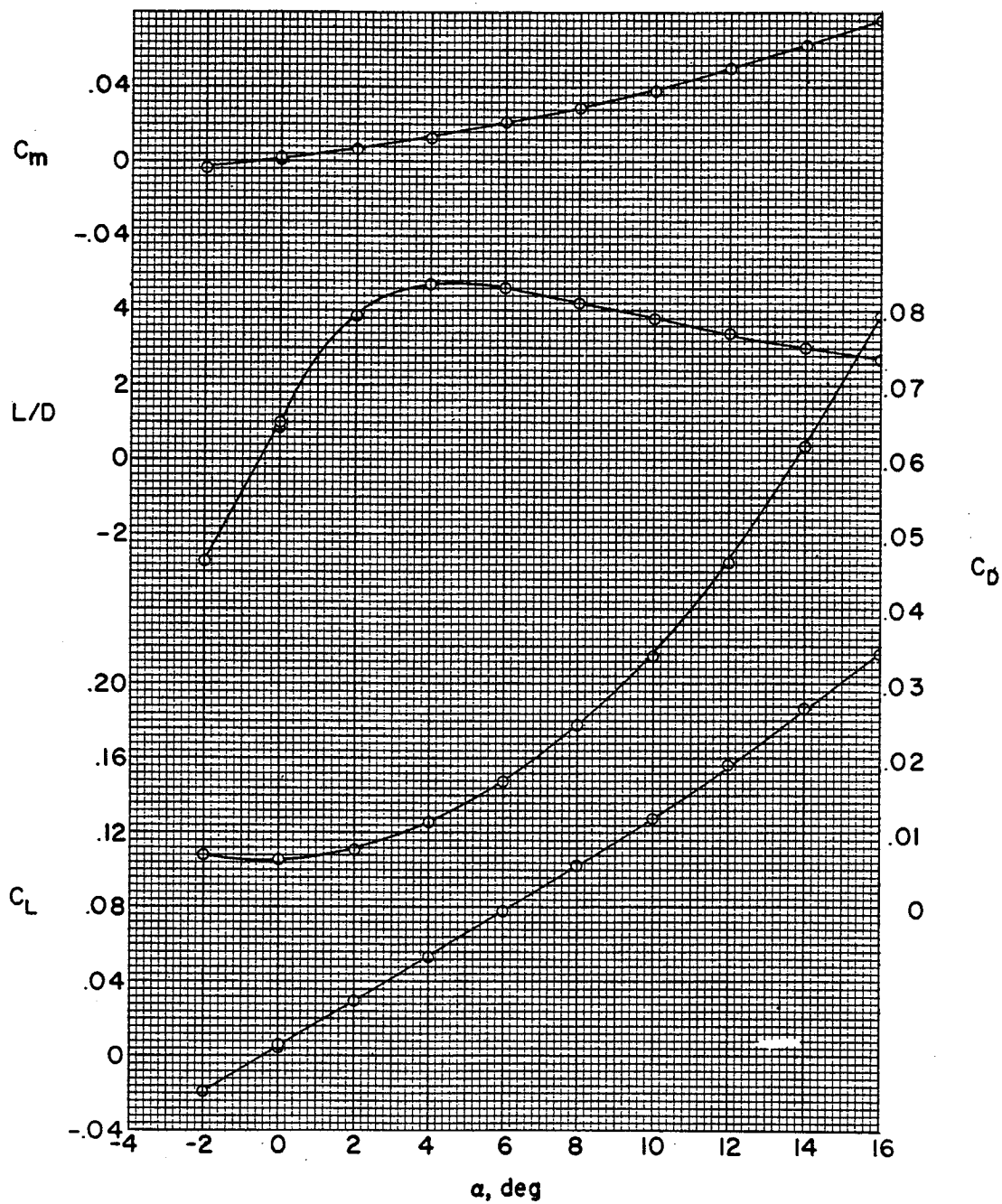
(d) $R = 2.1 \times 10^6$.

Figure 19.- Continued.
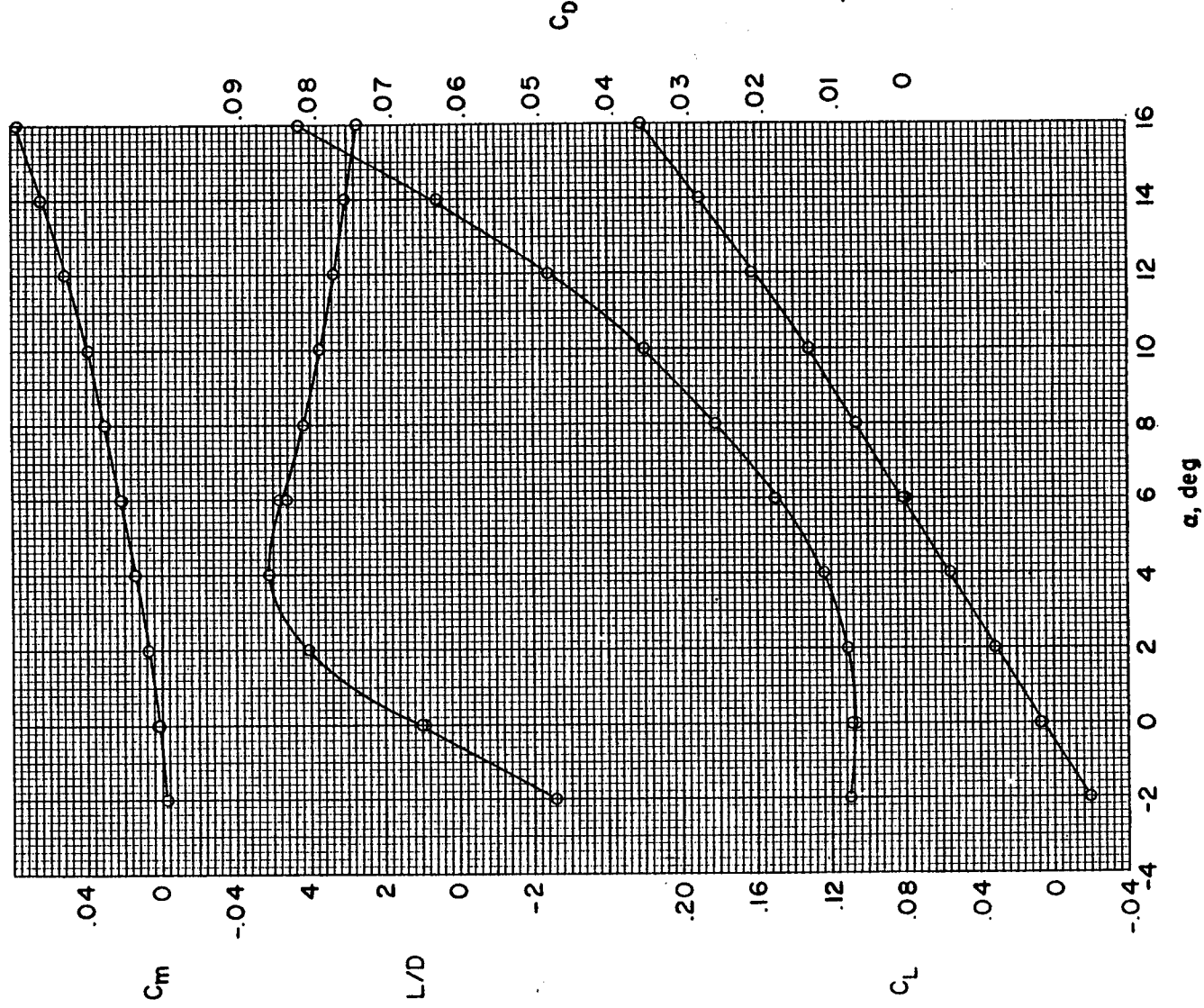
(e) $R = 2.6 \times 10^6$.

Figure 19.- Concluded.
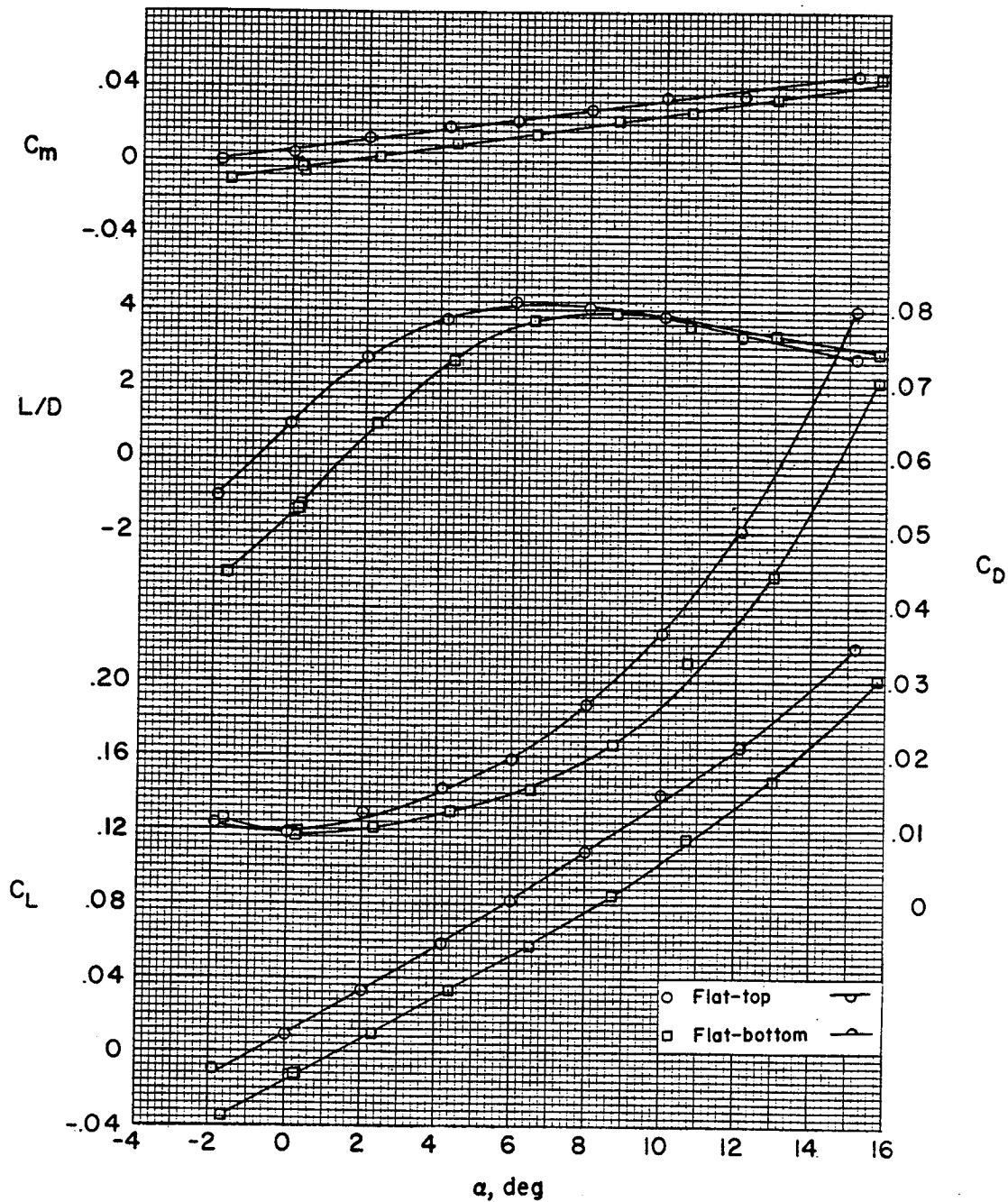
(a) Model 3.

Figure 20.- Longitudinal aerodynamic characteristics of models 3 to 6. M = 6.86 in air; R = 0.7 × 10^6.
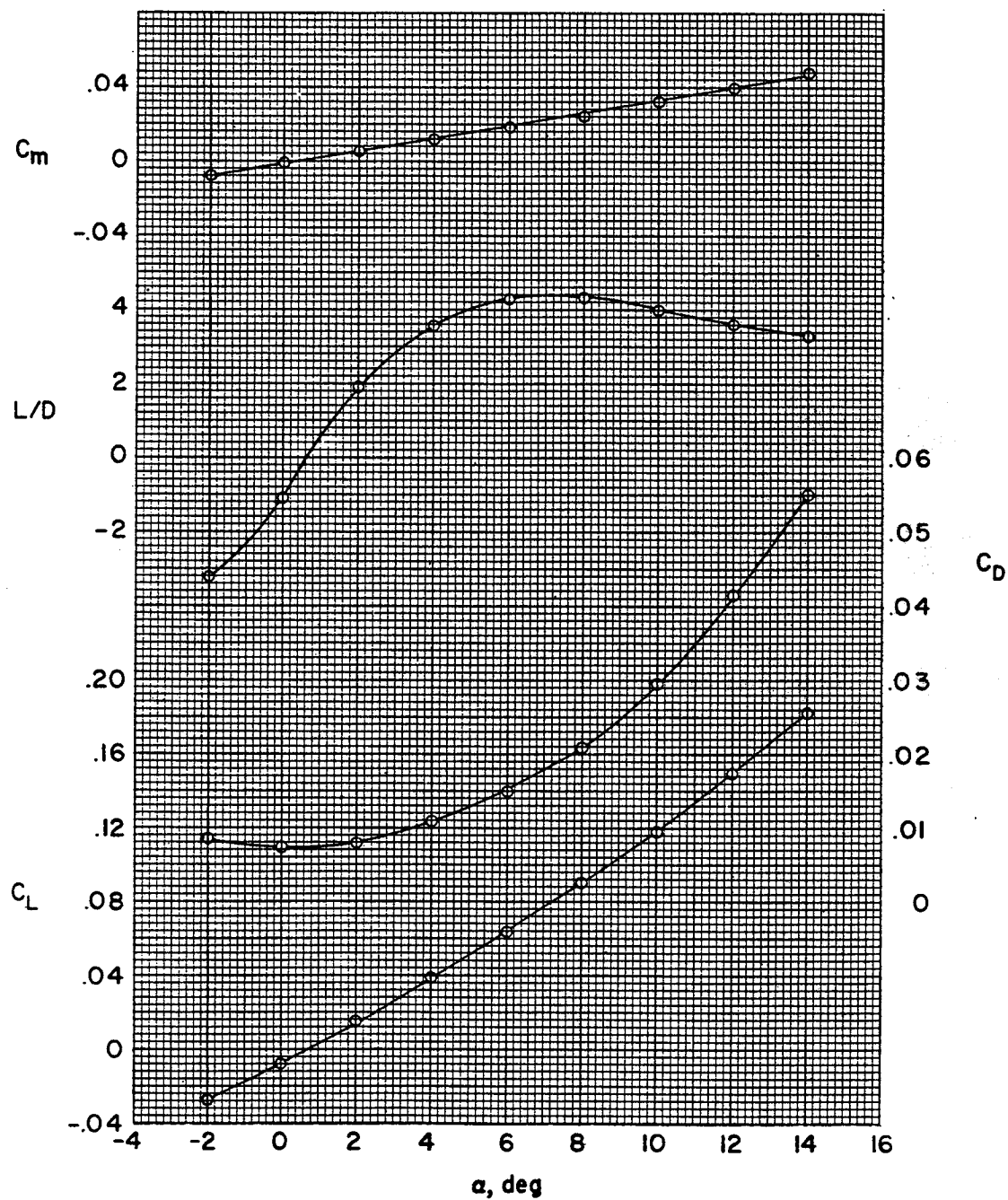
(b) Model 4.

Figure 20.- Continued.
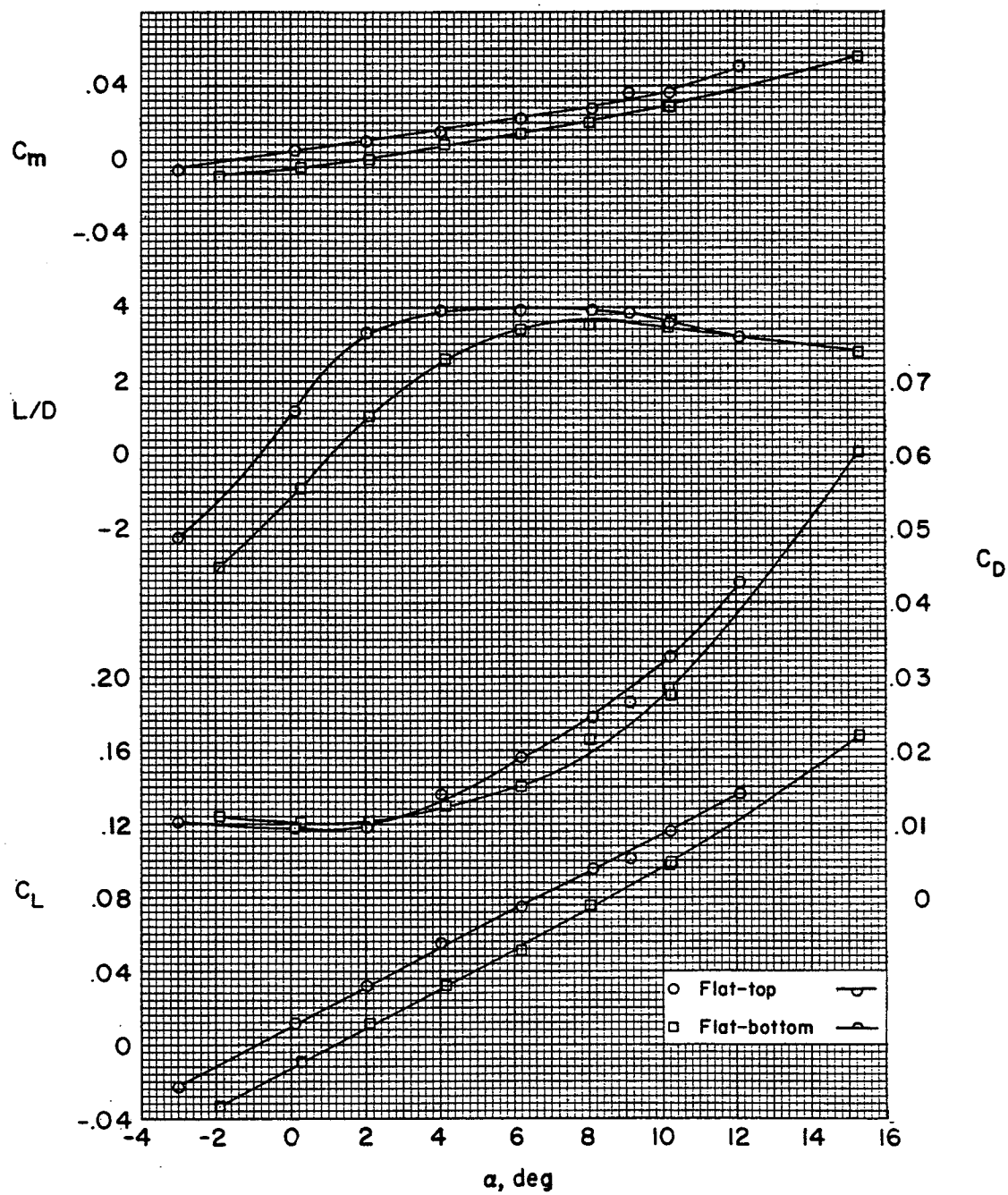
(c) Model 5.

Figure 20.- Continued.
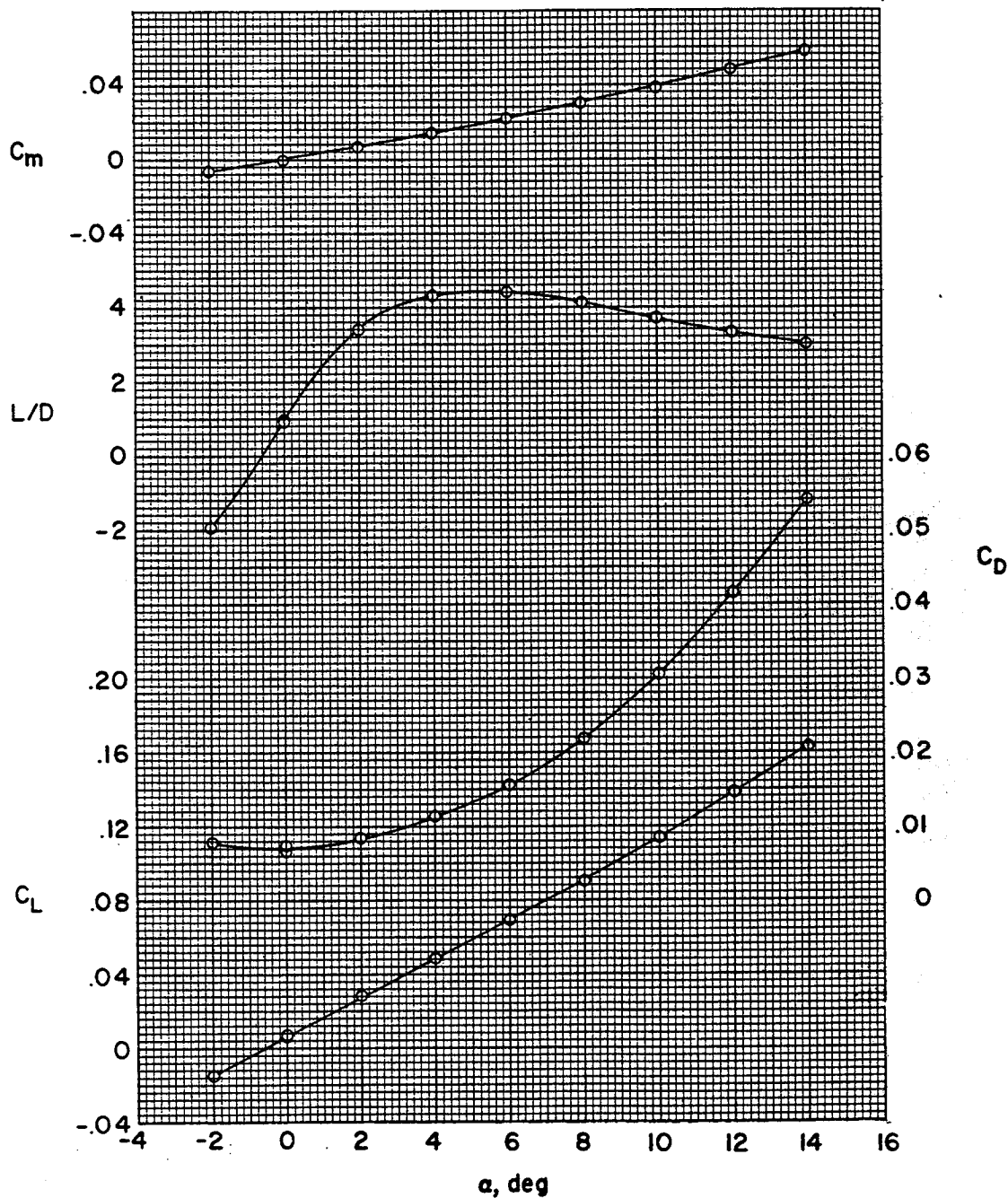
(d) Model 6.

Figure 20.- Concluded.
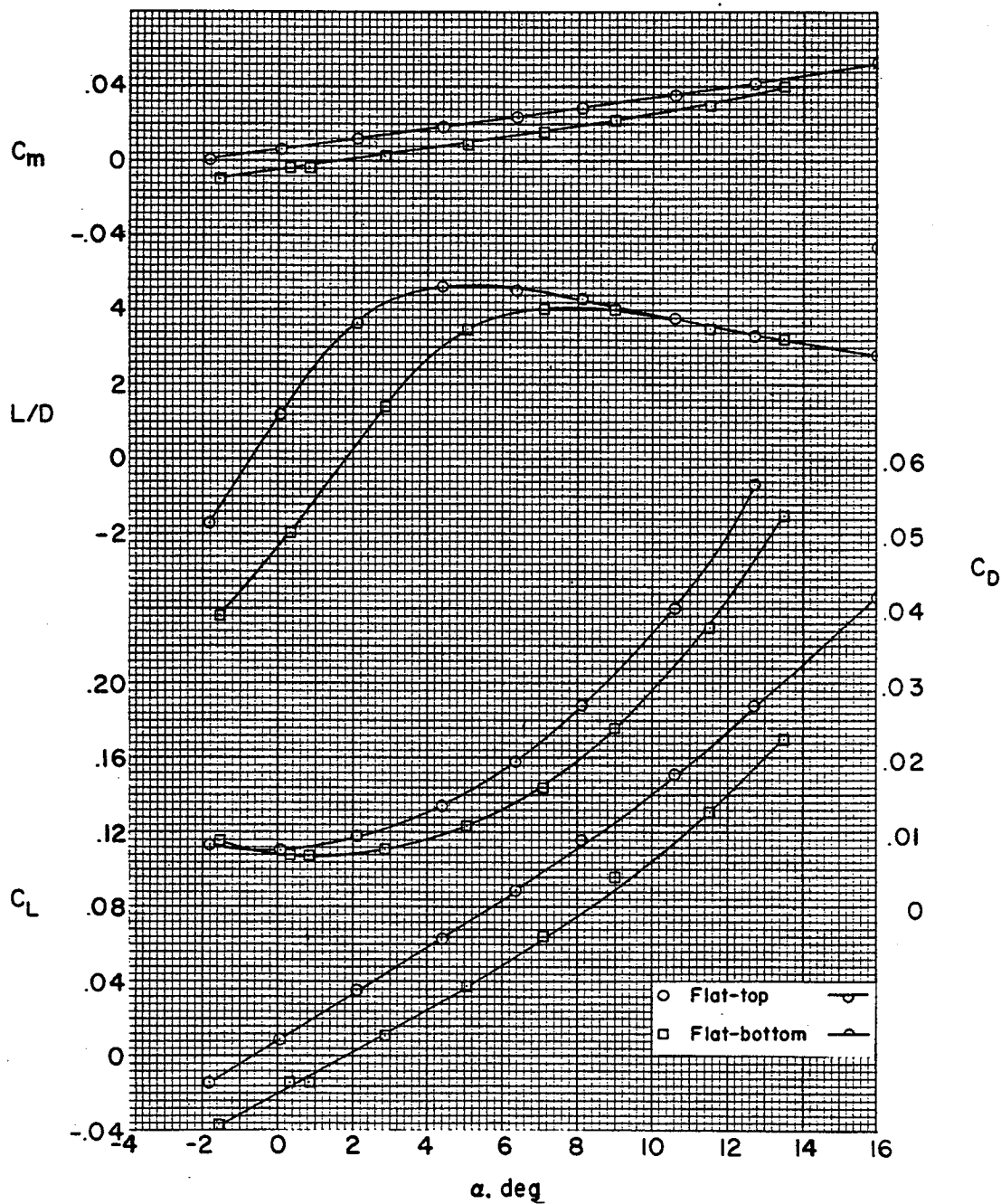
(a) Model 3.

Figure 21.- Longitudinal aerodynamic characteristics of models 3 to 6.
M = 6.86 in air; R = 2.1 x 10^6.
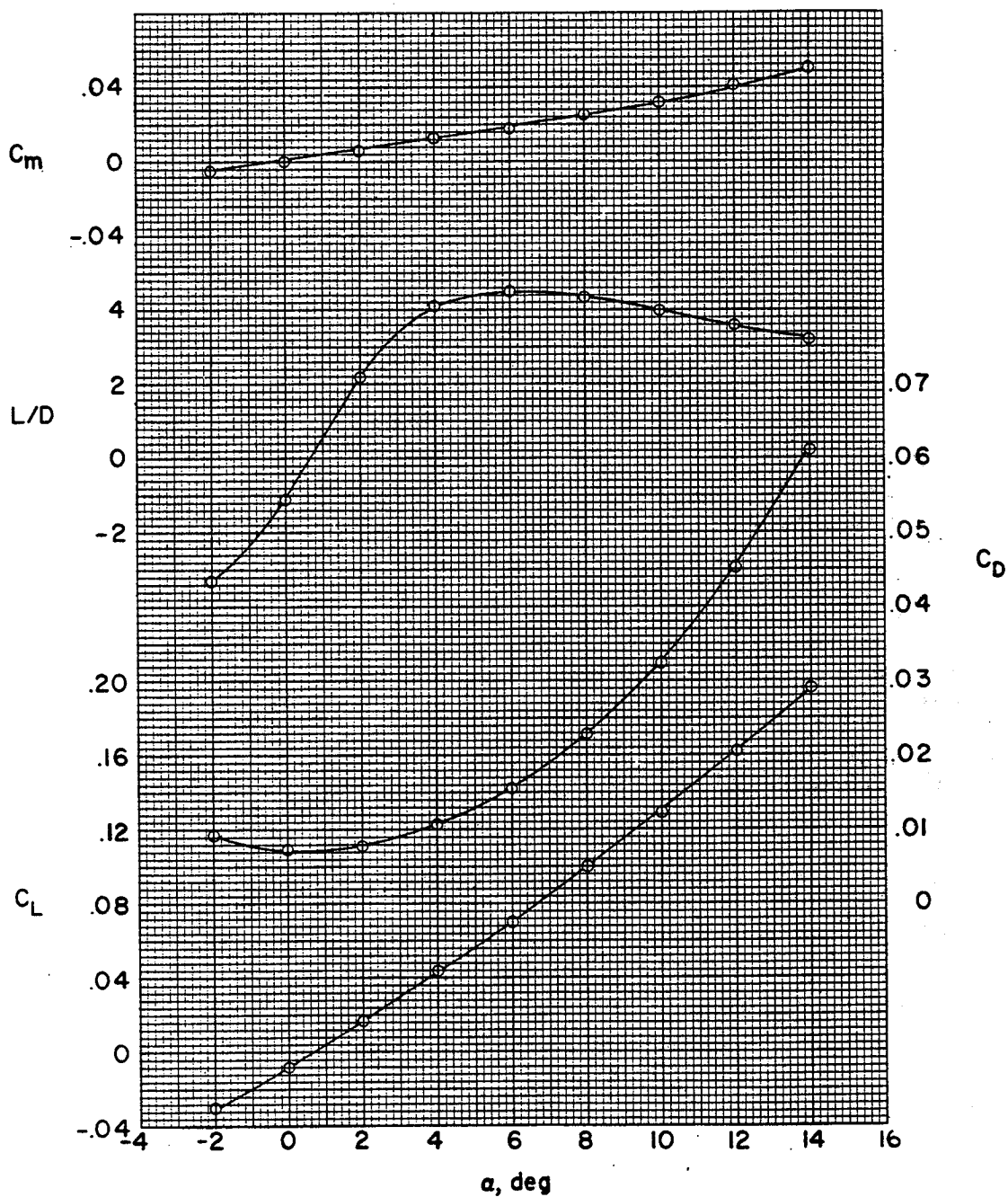
(b) Model 4.

Figure 21.- Continued.
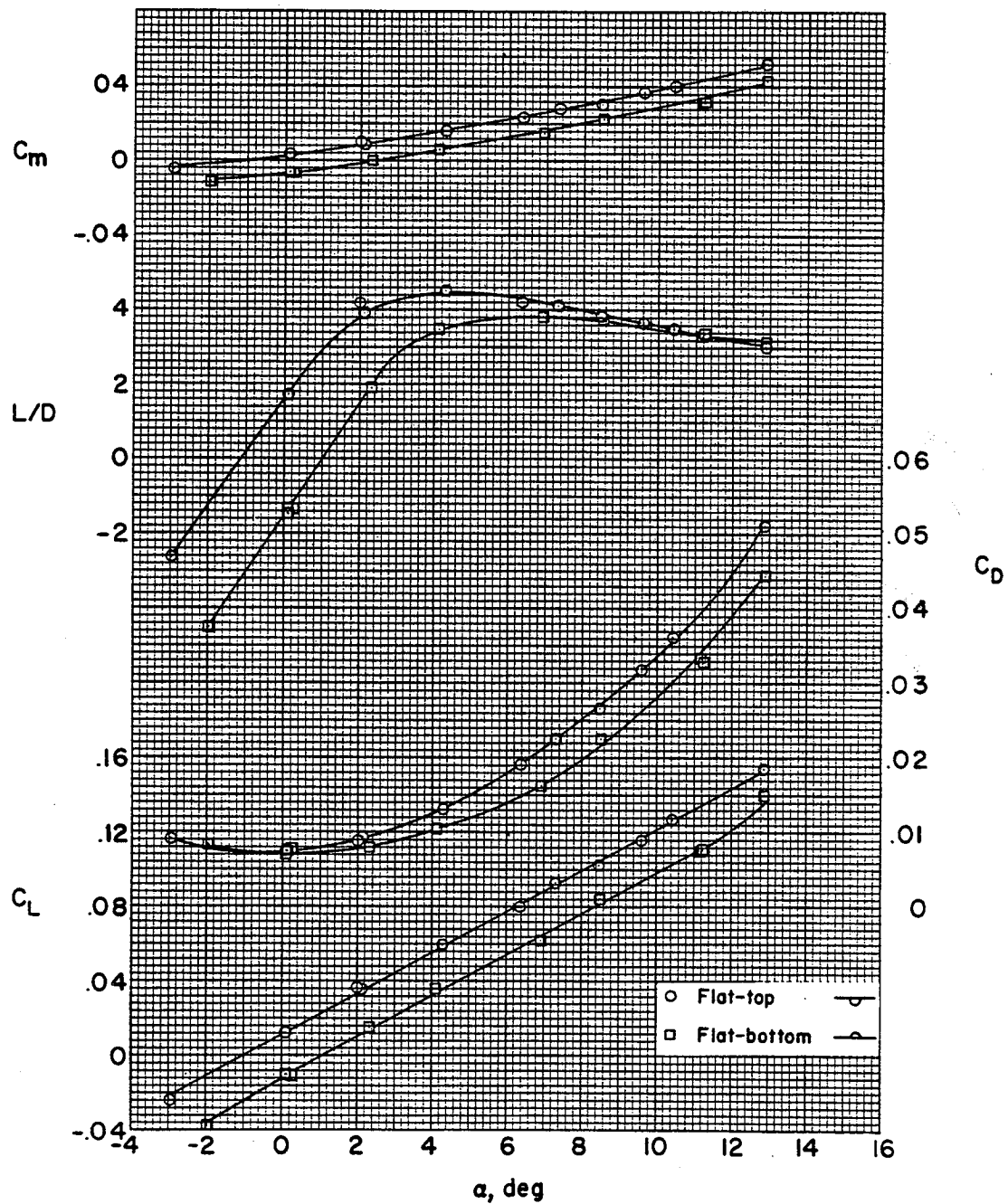
(c) Model 5.

Figure 21.- Continued.
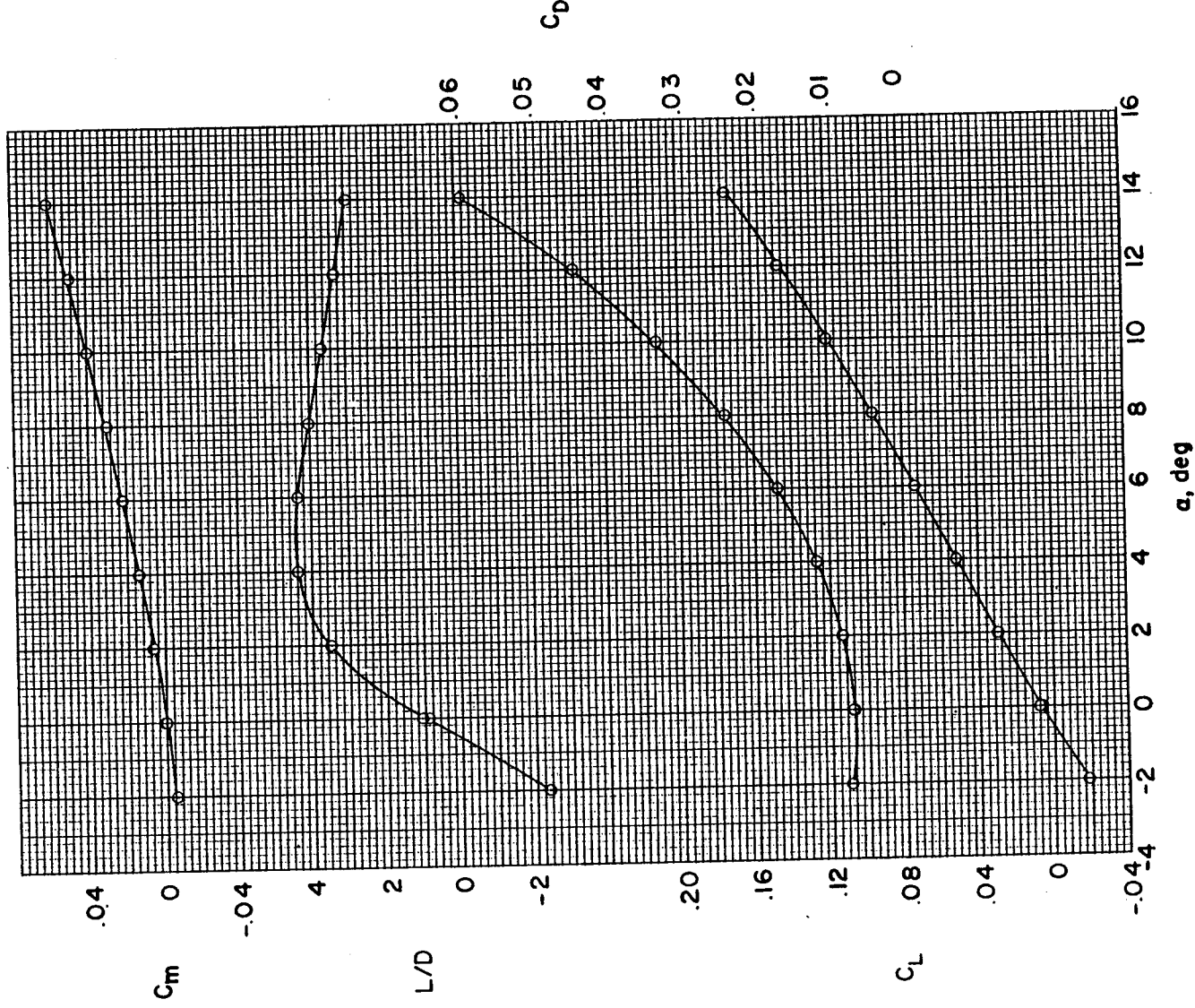
(d) Model 6.

Figure 21.- Concluded.
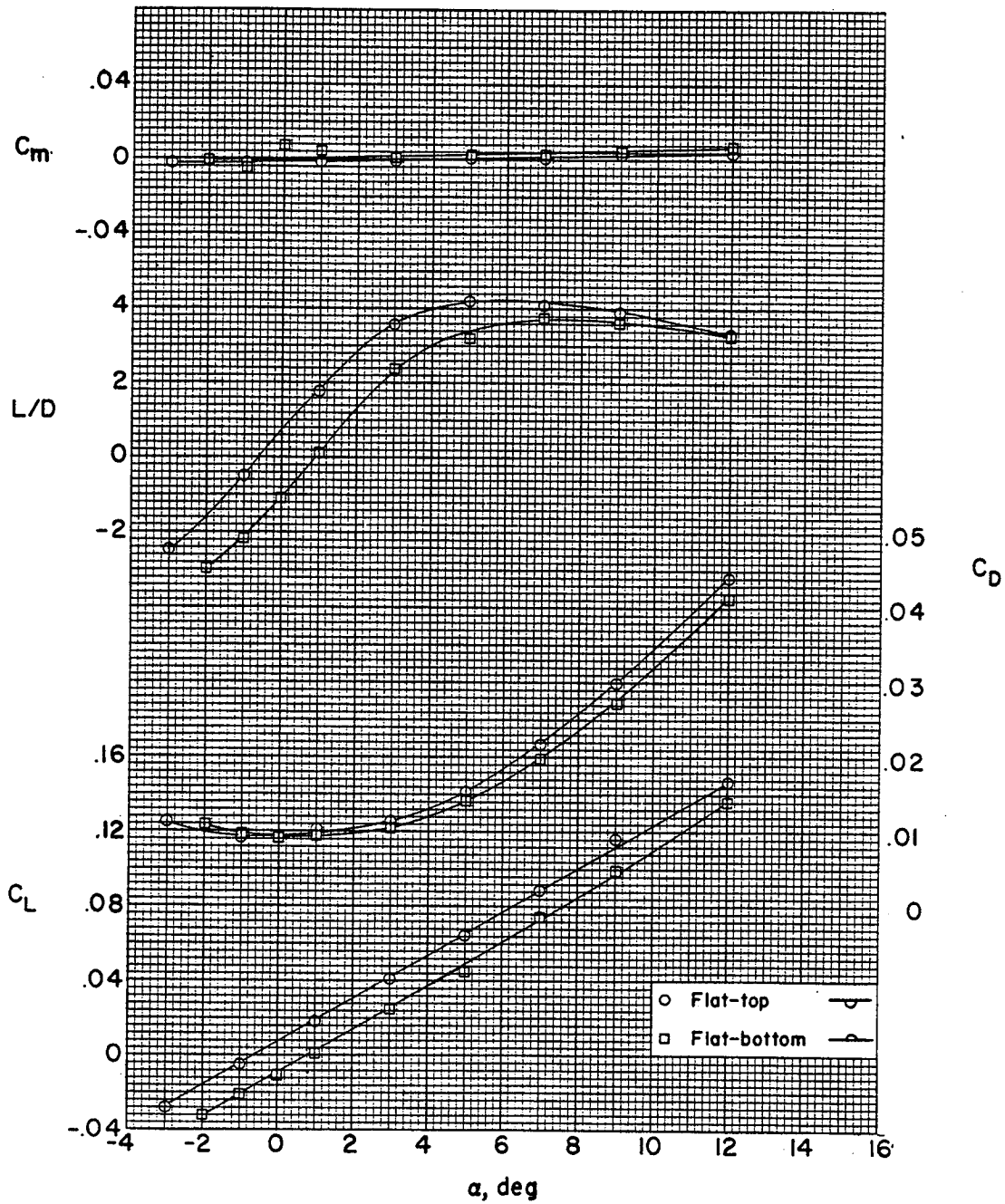
Figure 22.- Longitudinal aerodynamic characteristics of model 9.
M = 6.86 in air; R = 0.36 x 10⁶.
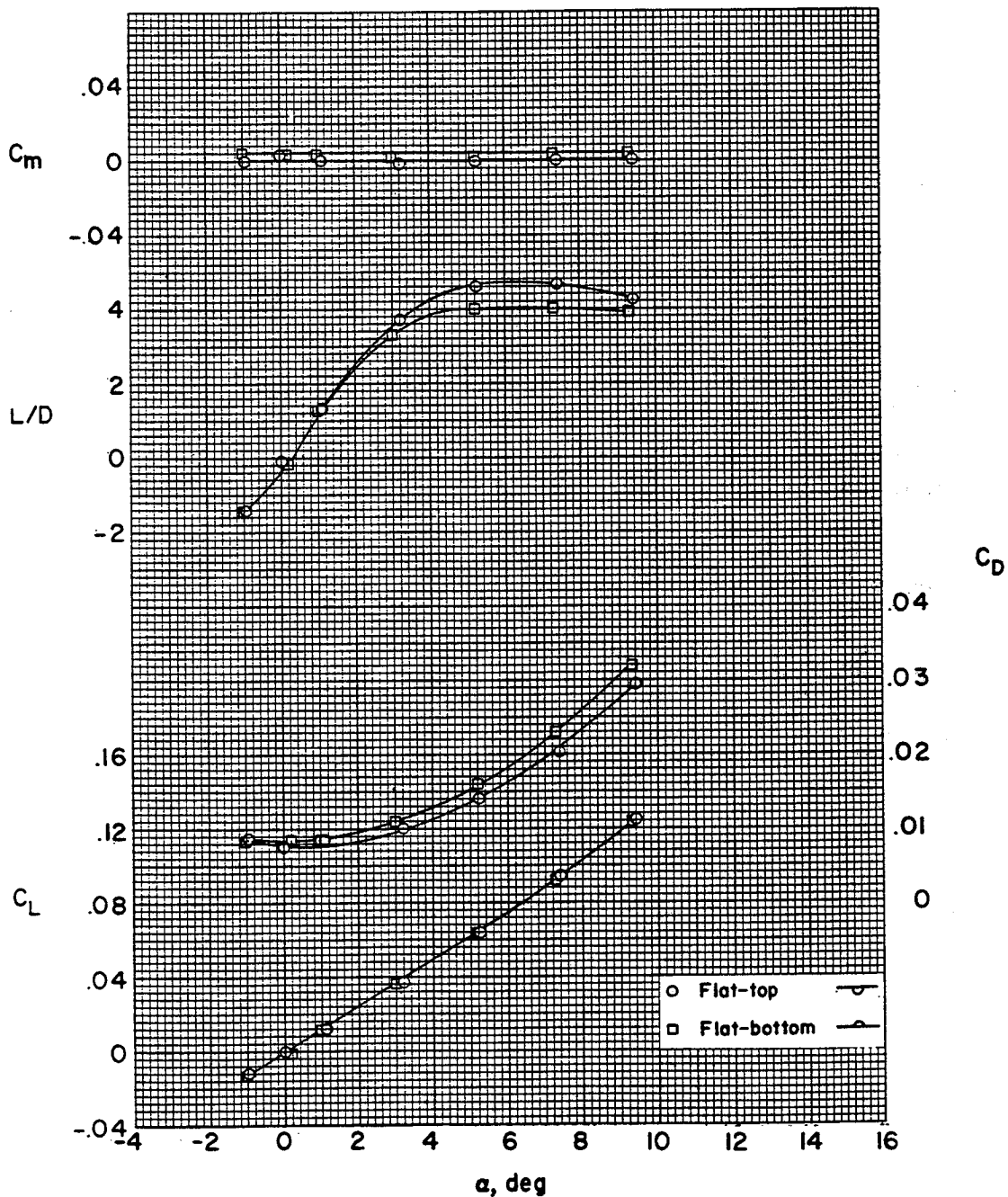
L-247

(a) Model 7.

Figure 23.- Longitudinal aerodynamic characteristics of a series of wing-body combinations. M = 6.86 in air; R = 1.3 × 10^6.
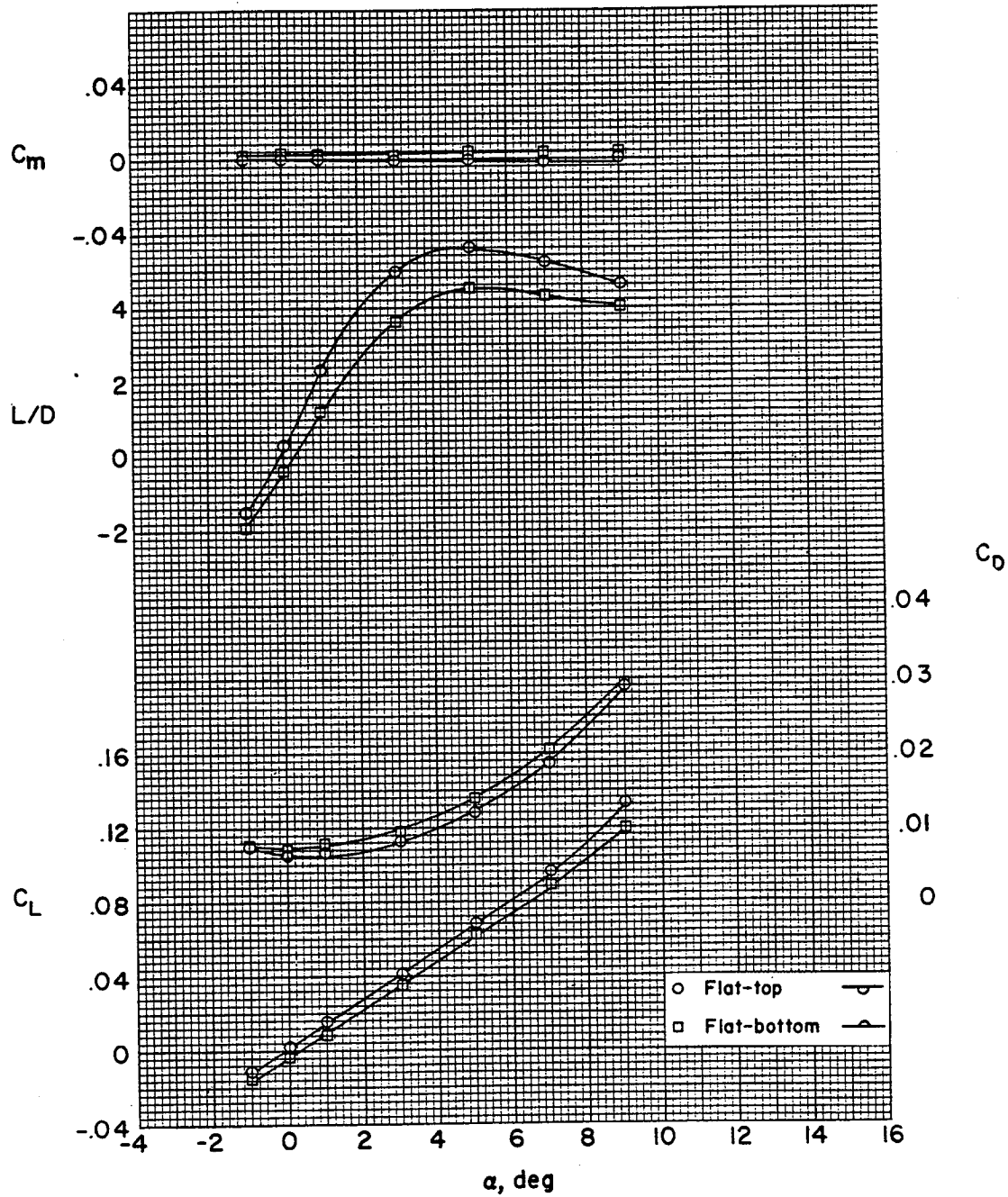
(b) Model 8.

Figure 23.- Continued.
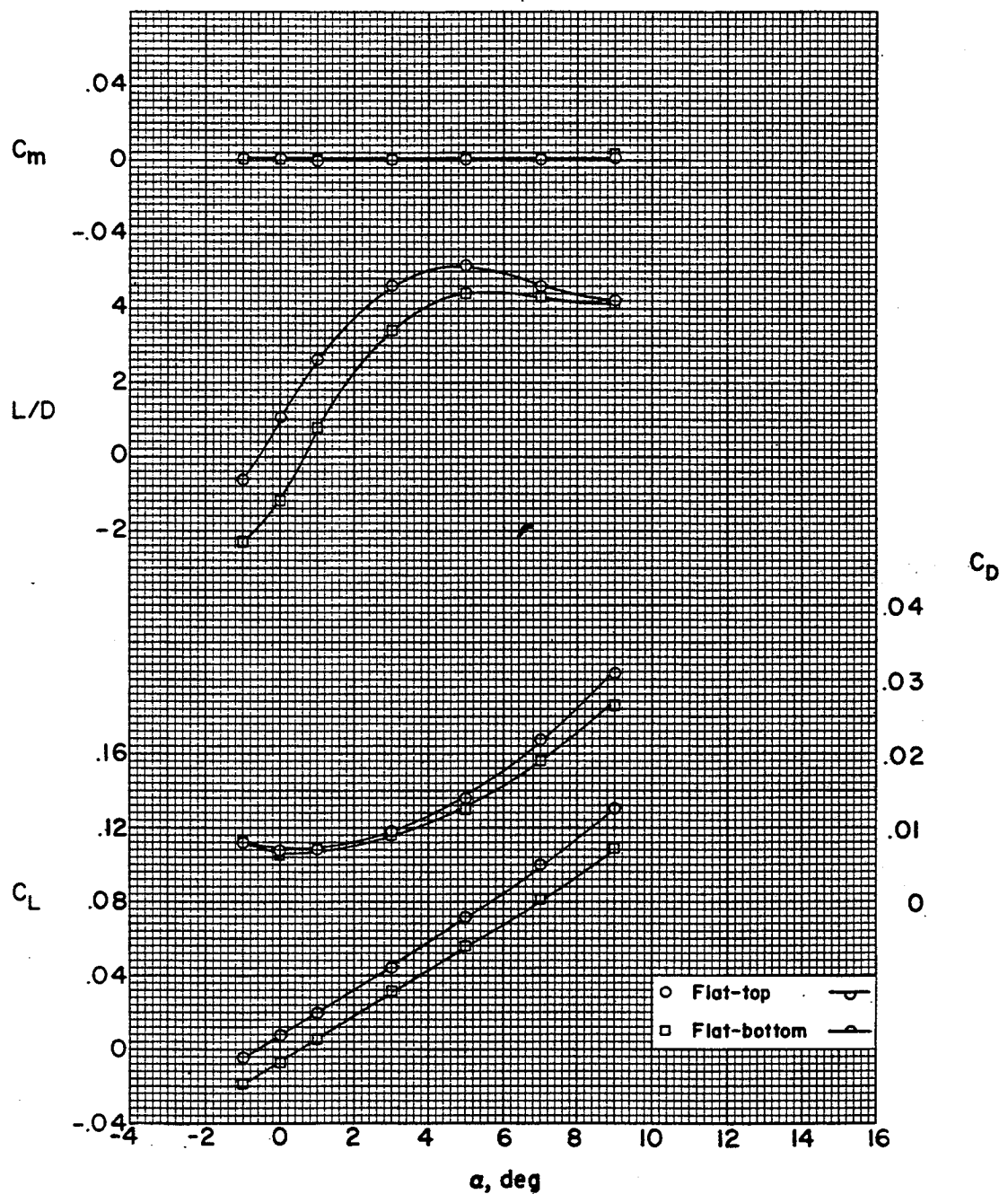
(c) Model 9.

Figure 23.- Continued.
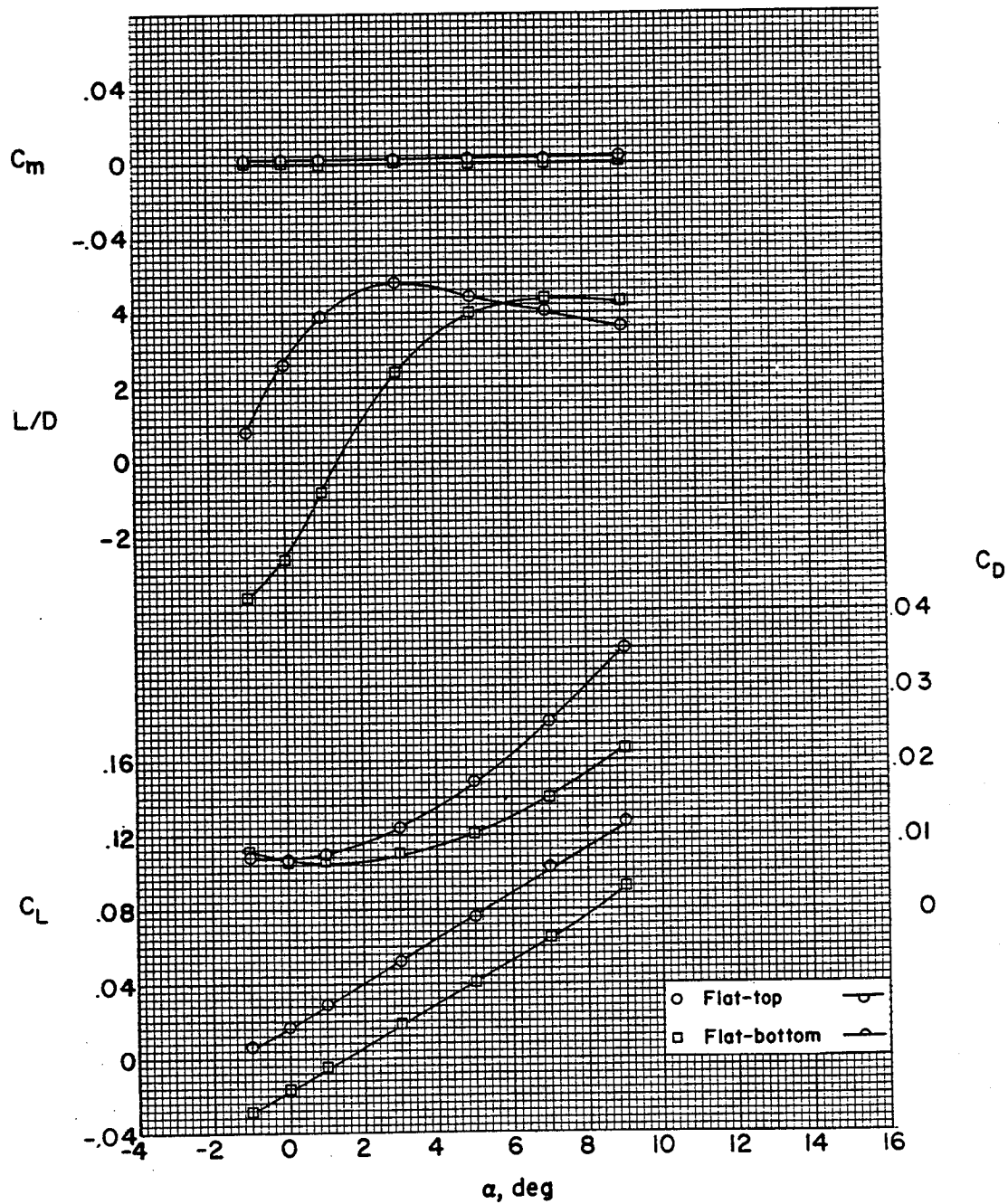
(d) Model 10.

Figure 23.- Continued.
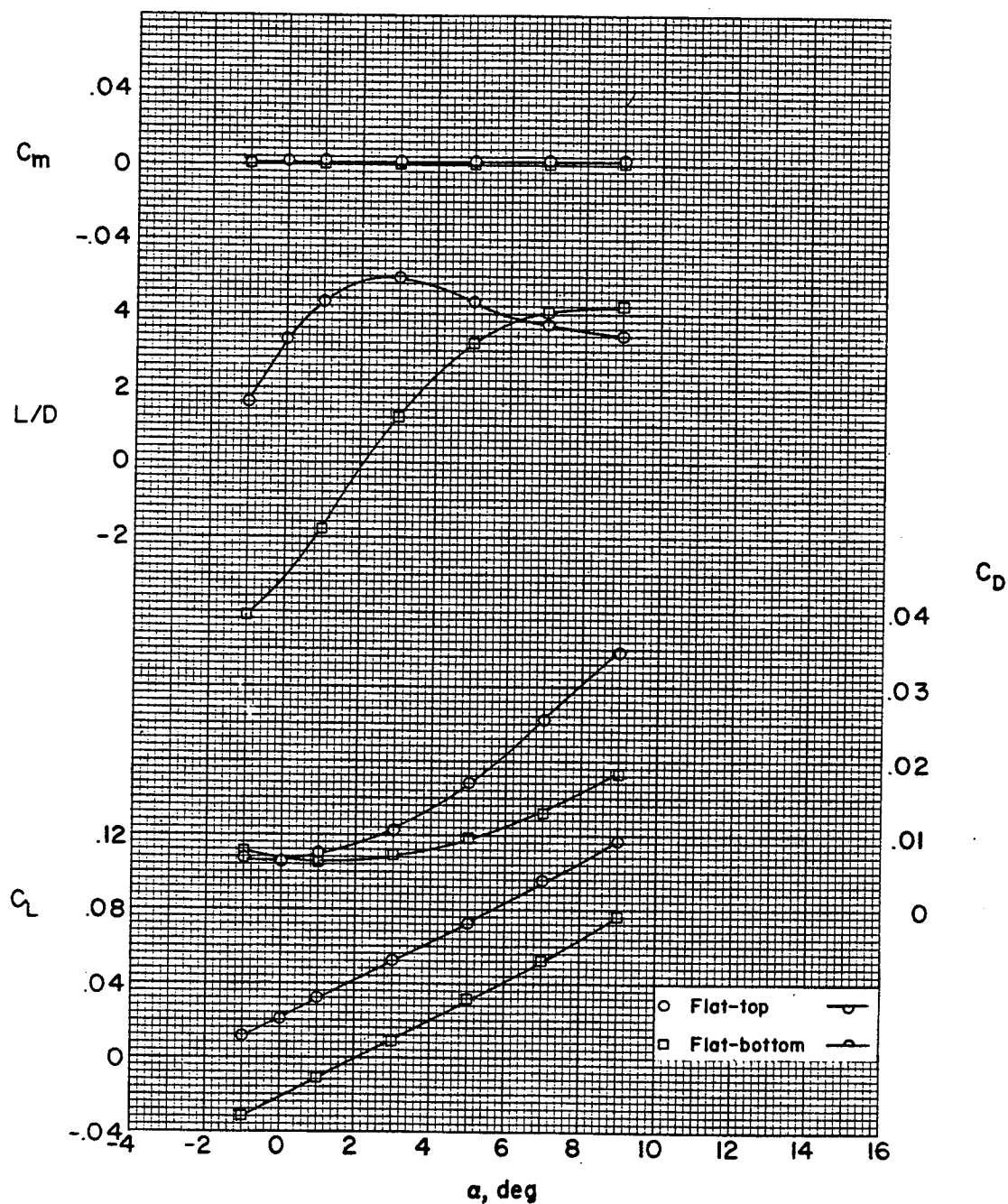
L-247

(e) Model 11.

Figure 23.- Continued.
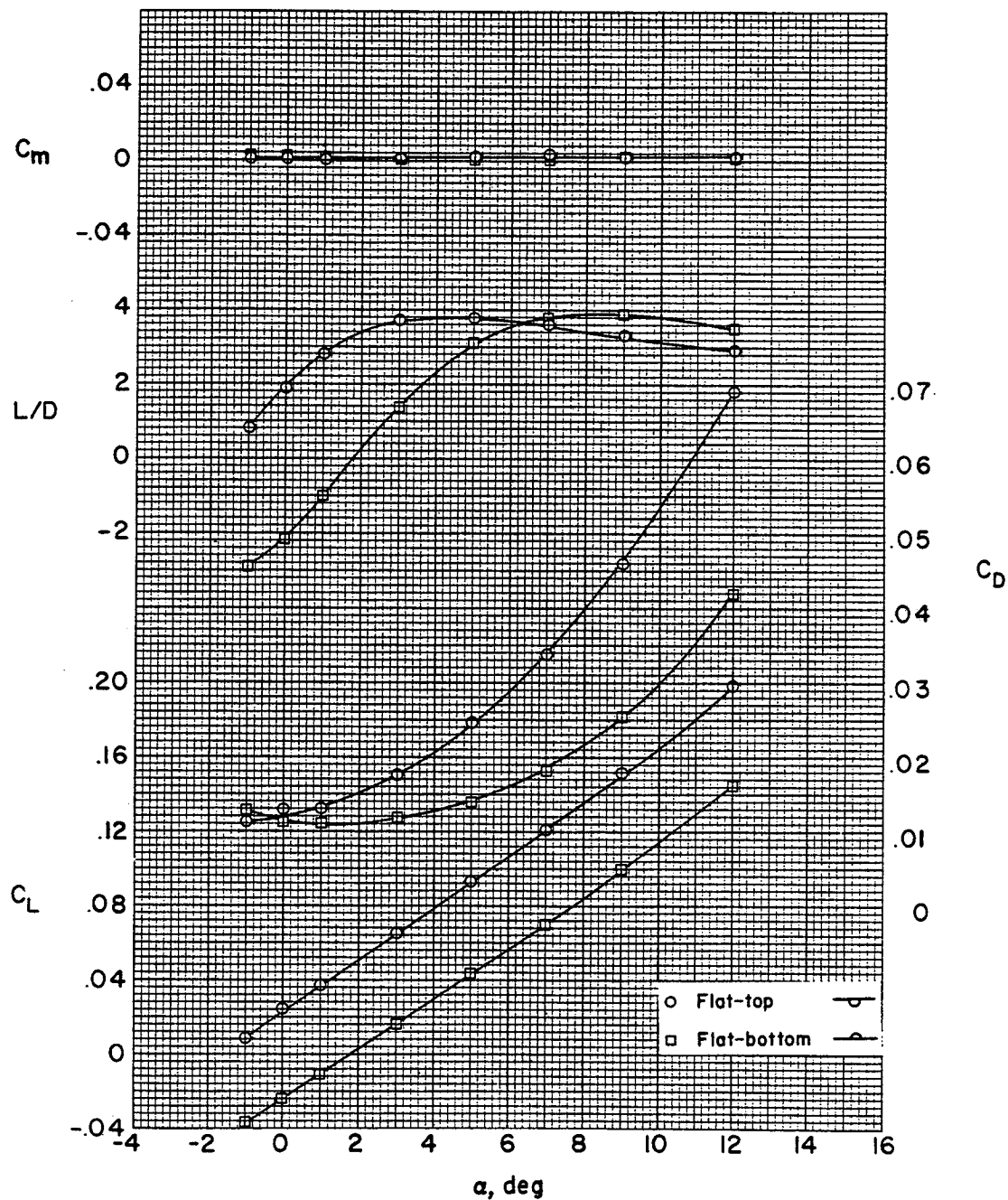
(f) Model 12.

Figure 23.- Continued.
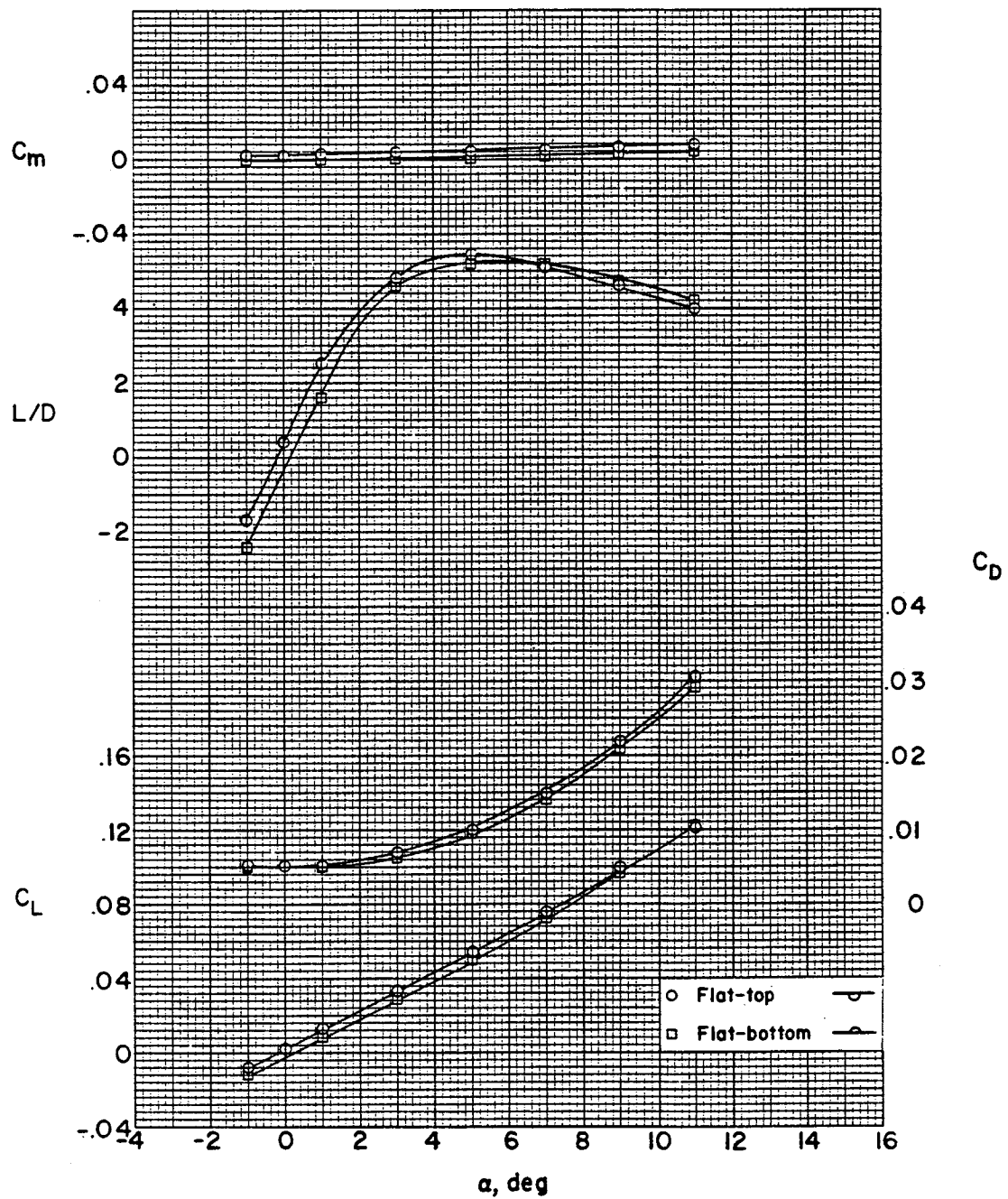
(g) Model 14.

Figure 23.- Continued.
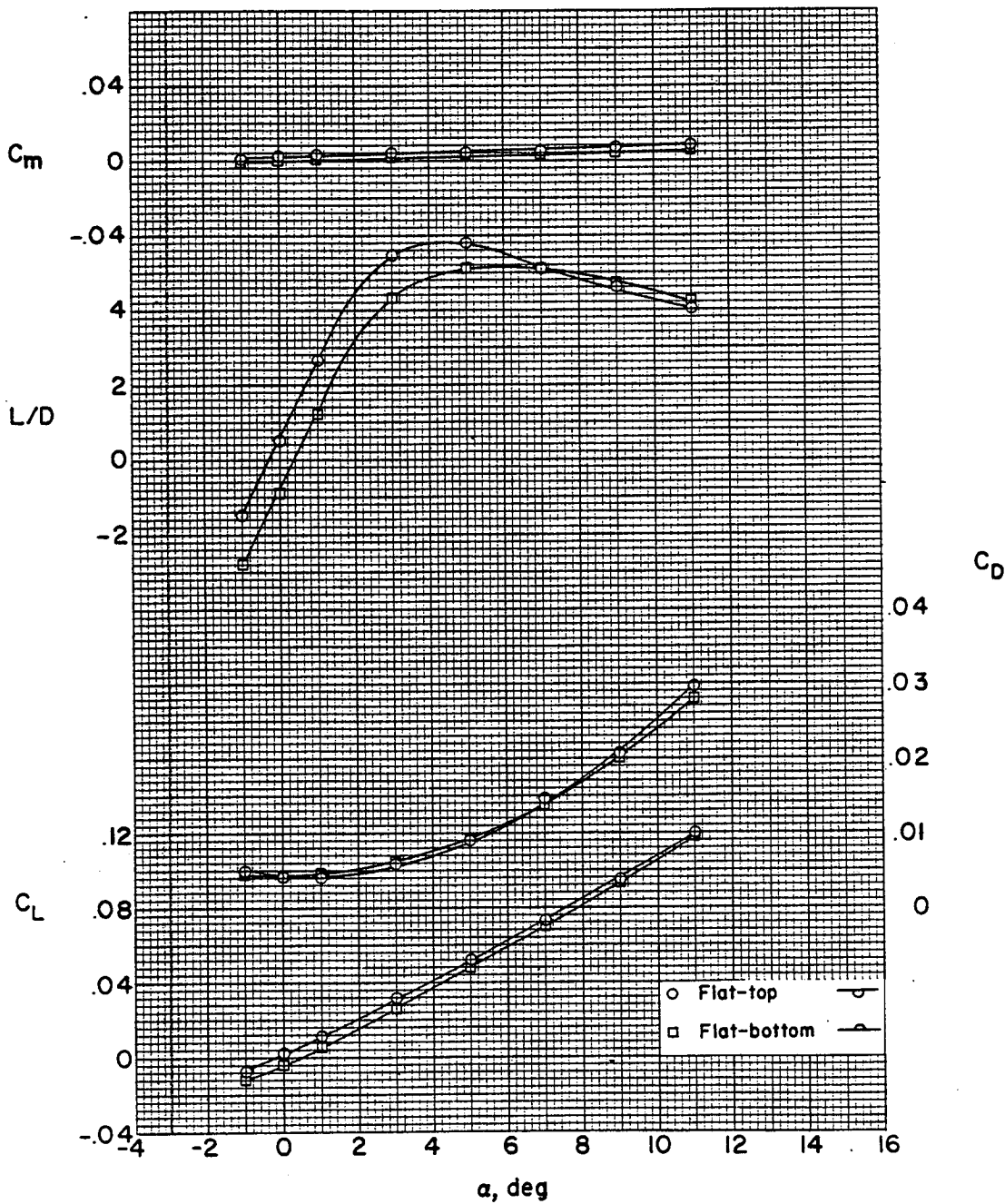
(h) Model 15.

Figure 23.- Concluded.
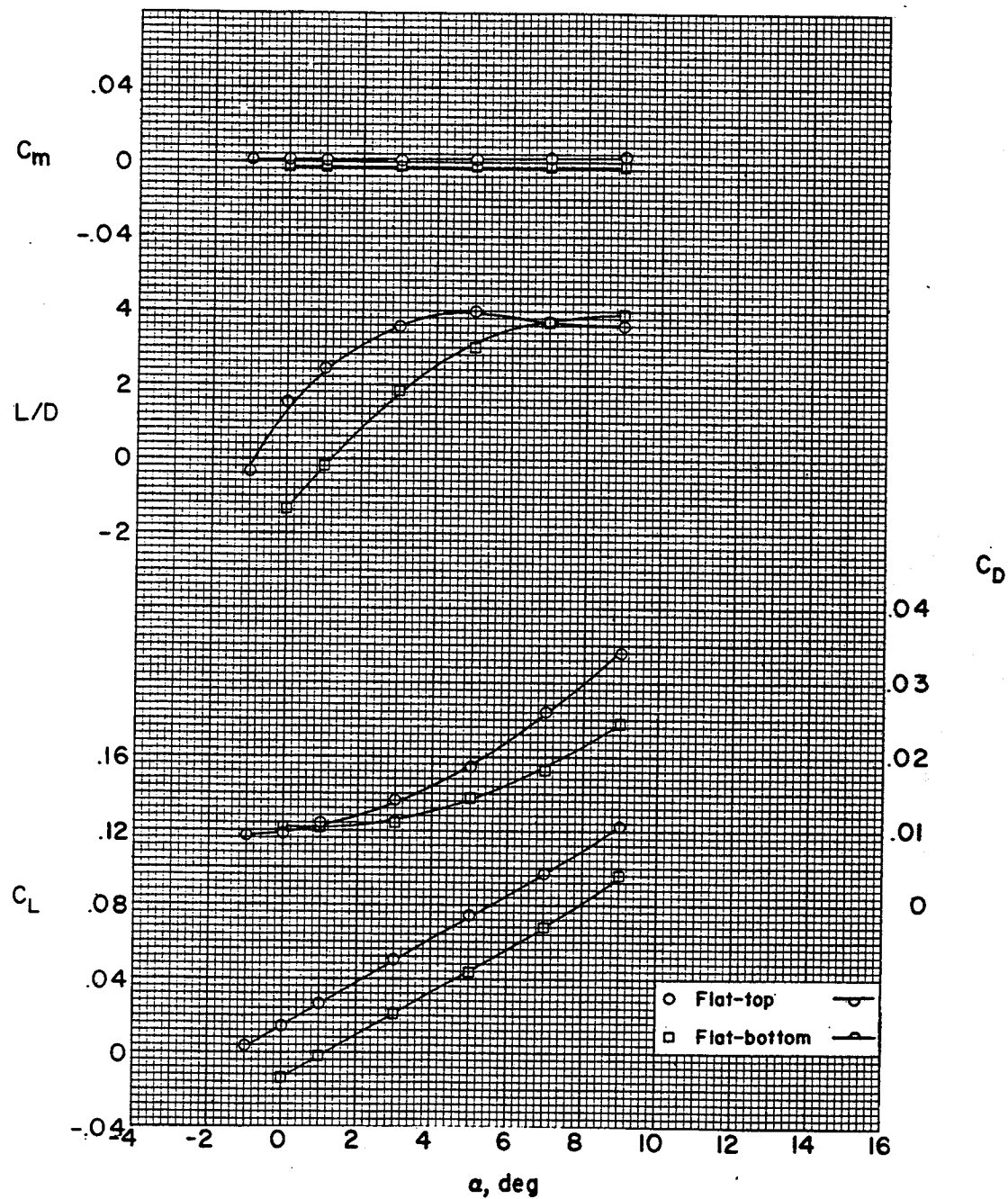
(a) R = 0.36 × 10^6.

Figure 24.- Longitudinal aerodynamic characteristics of model 13.
M = 6.86 in air.

(b) R = 0.7 × 10⁶.

Figure 24.- Continued.

(c) R = 1.4 × 10^6.

Figure 24.- Continued.
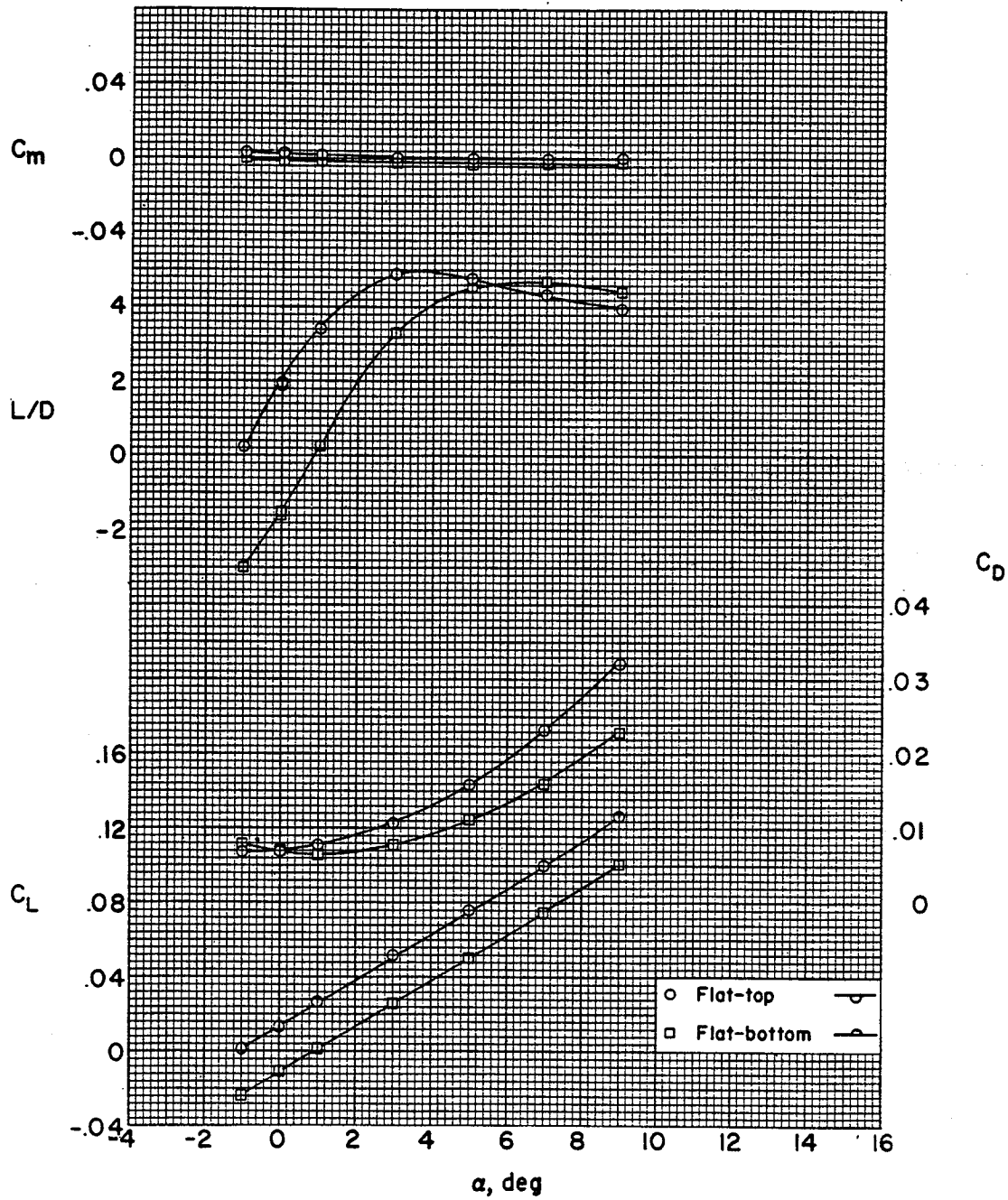
(d) R = 2.2 × 10^6.

Figure 24.- Continued.
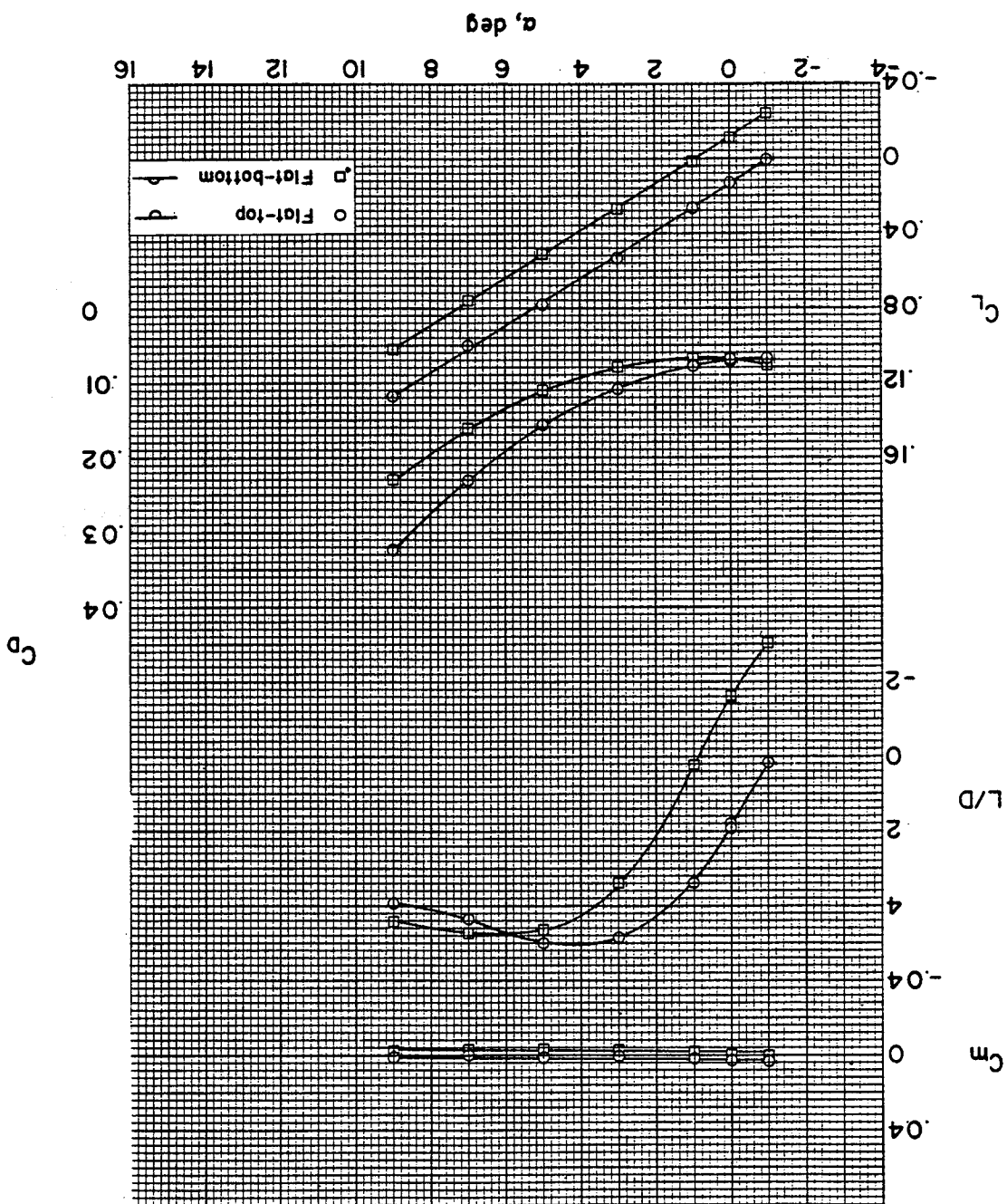
(e) $R = 3.0 \times 10^6$.

Figure 24.- Concluded.

L-247
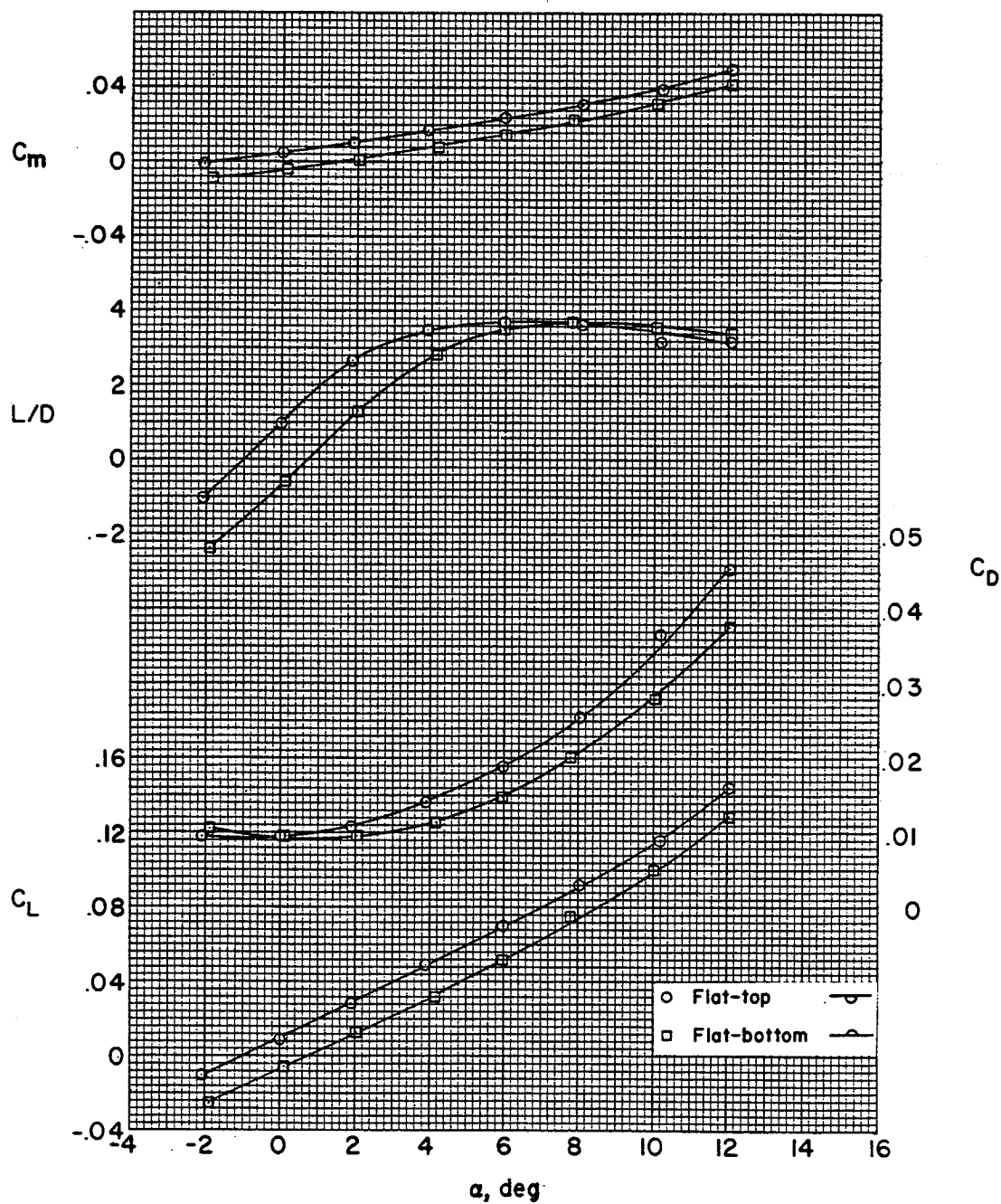
(a) Model 1.

Figure 25.- Longitudinal aerodynamic characteristics of several wing-body combinations. $M = 9.6$ in air; $R = 0.7 \times 10^6$.
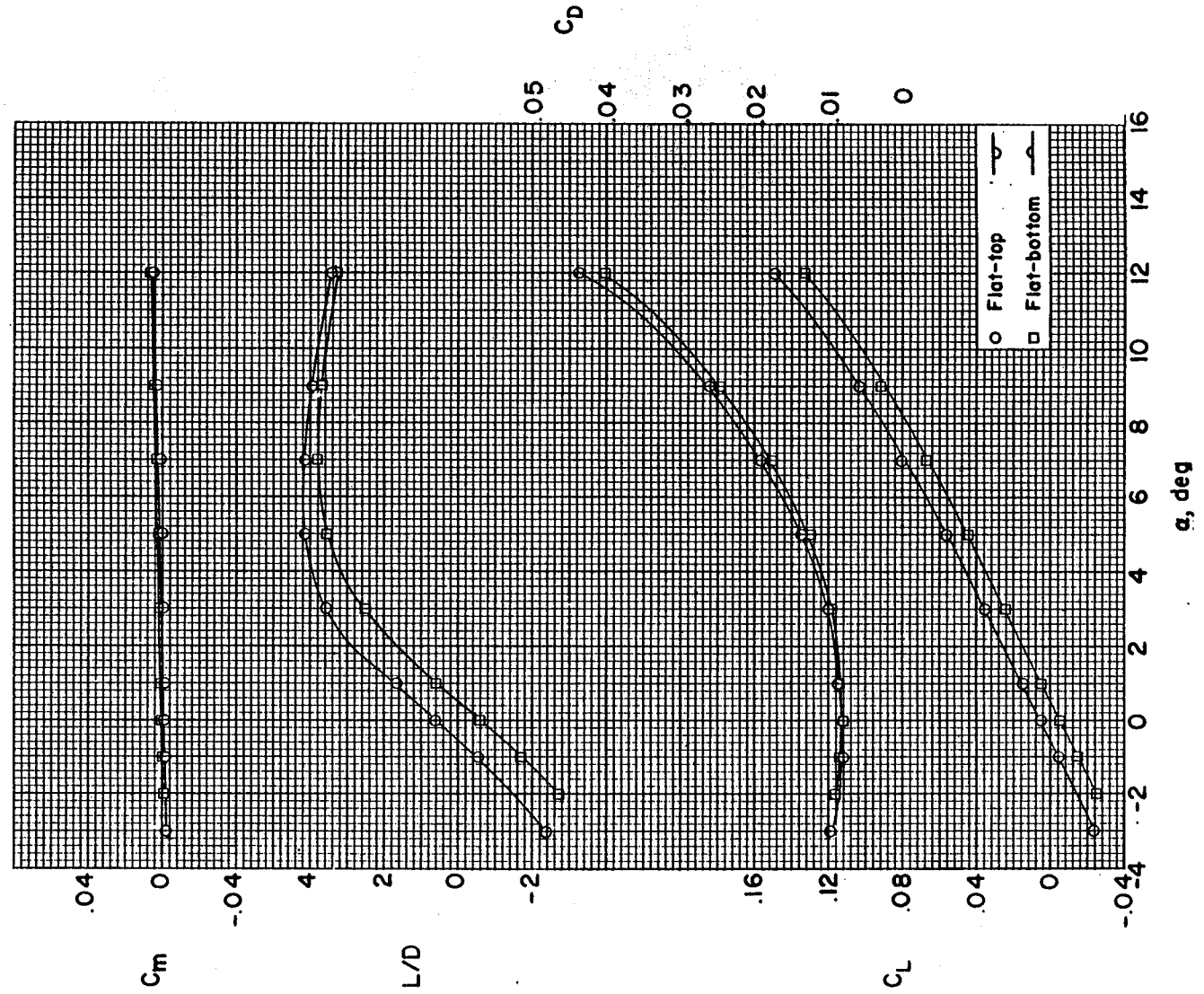
(b) Model 9.

Figure 25.- Continued.
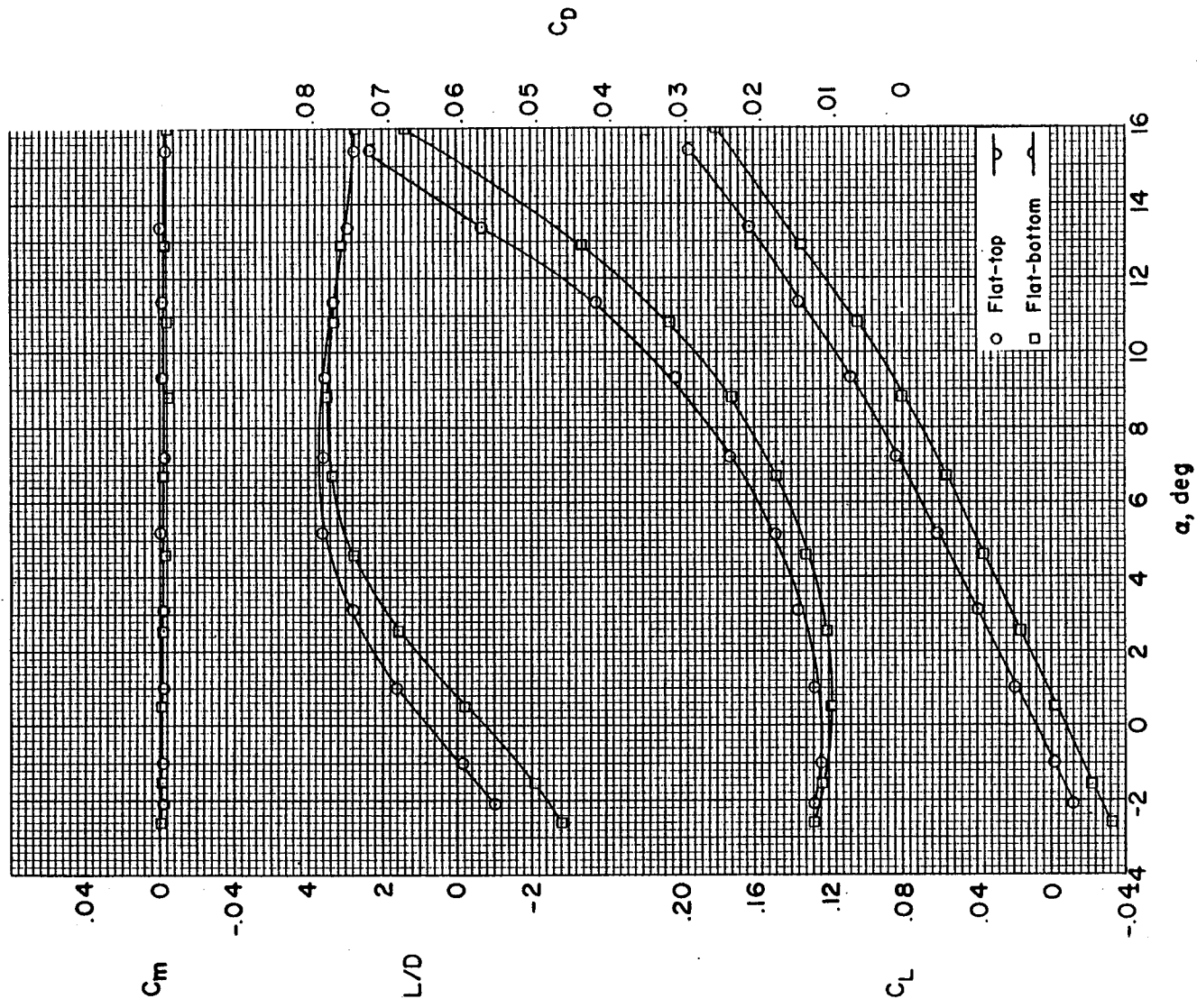
(c) Model 13.

Figure 25.- Concluded.
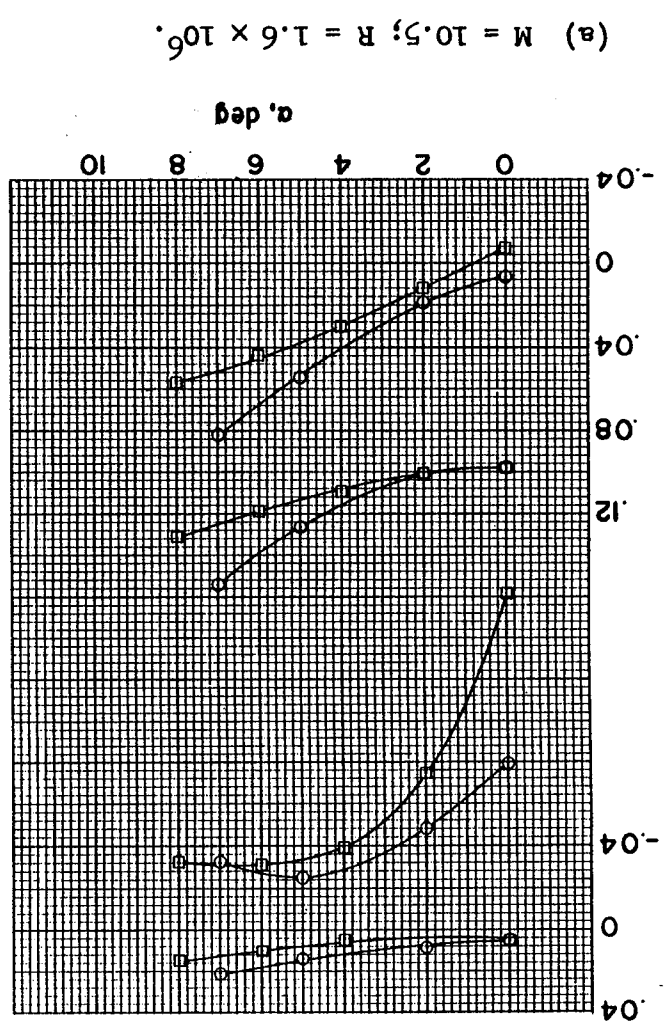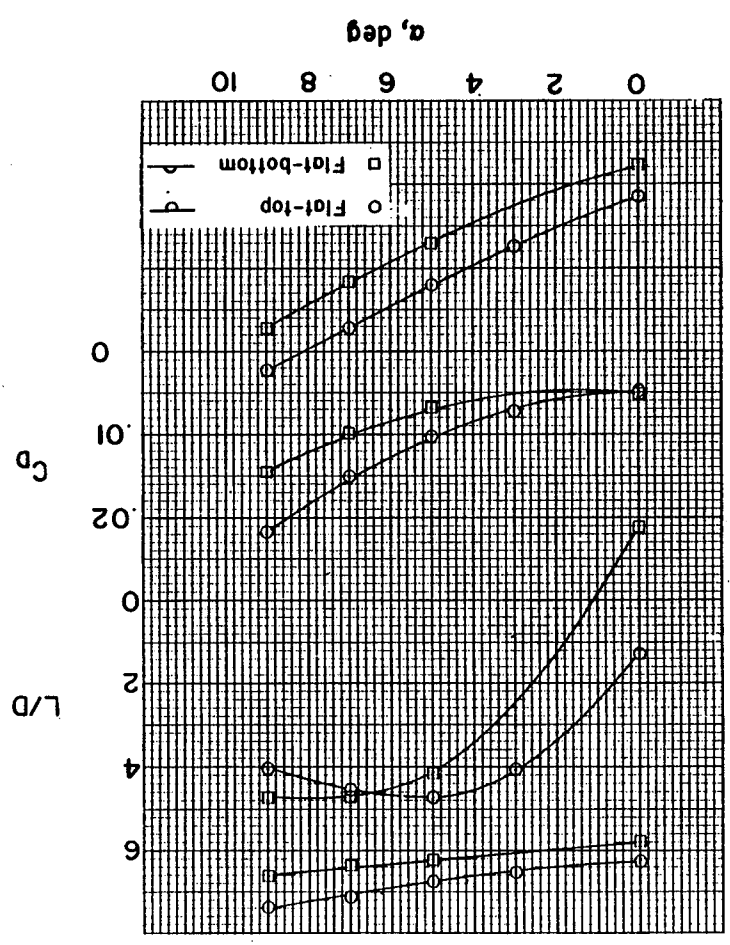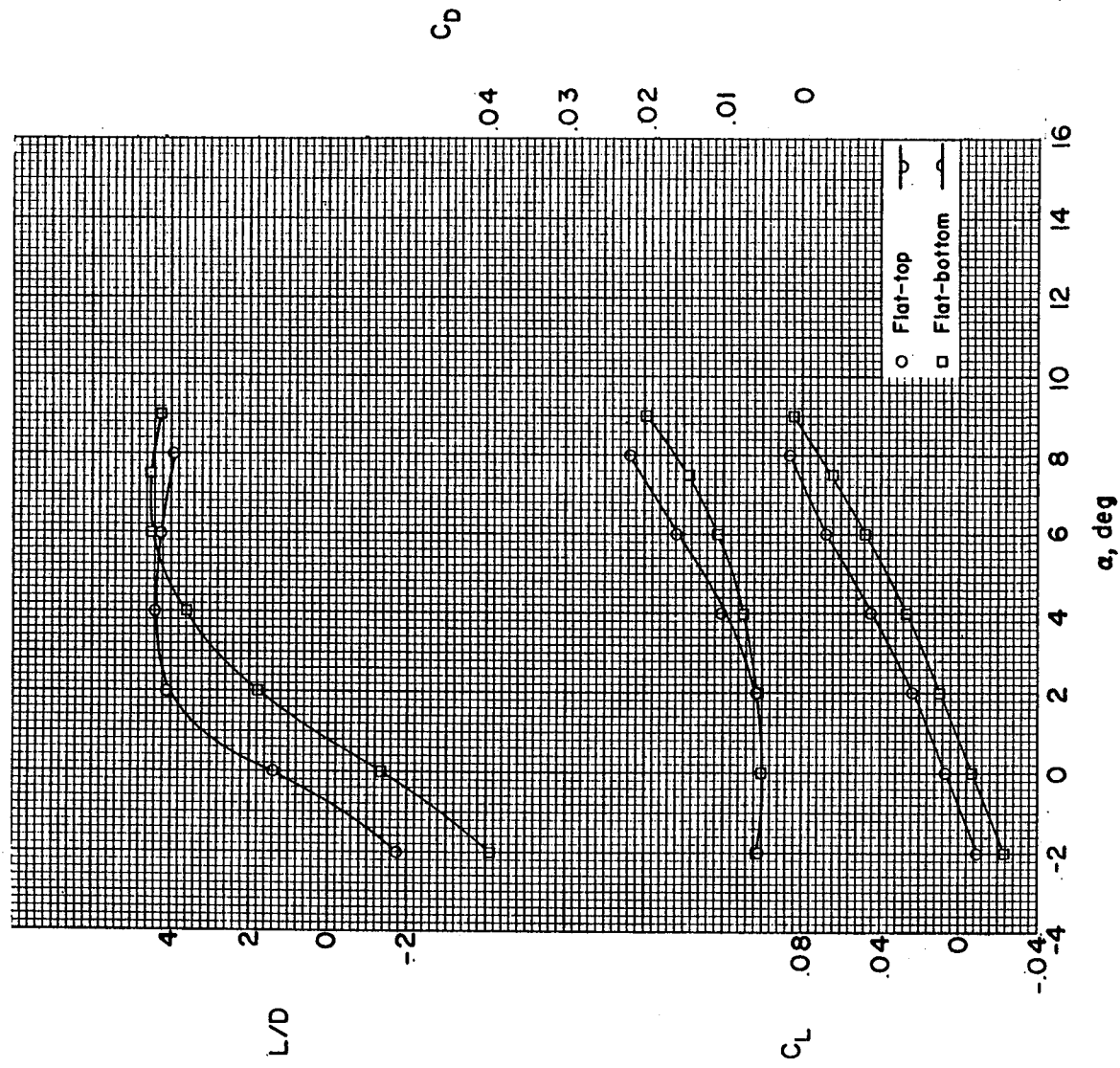
(c) M = 17.8; R = 3.4 × 10⁶.

Figure 26.- Concluded.
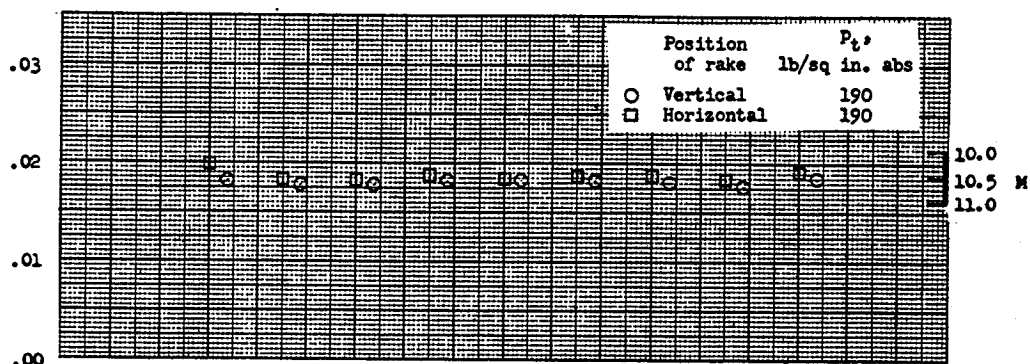
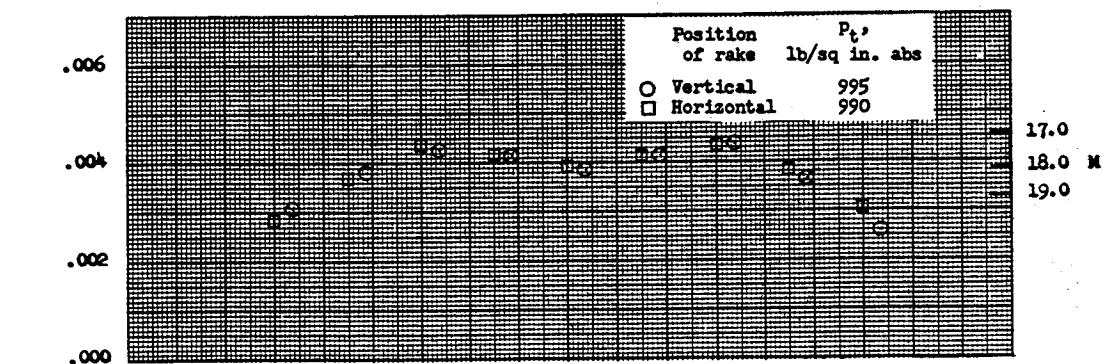(a) Rake 4 inches upstream of center line of test section.
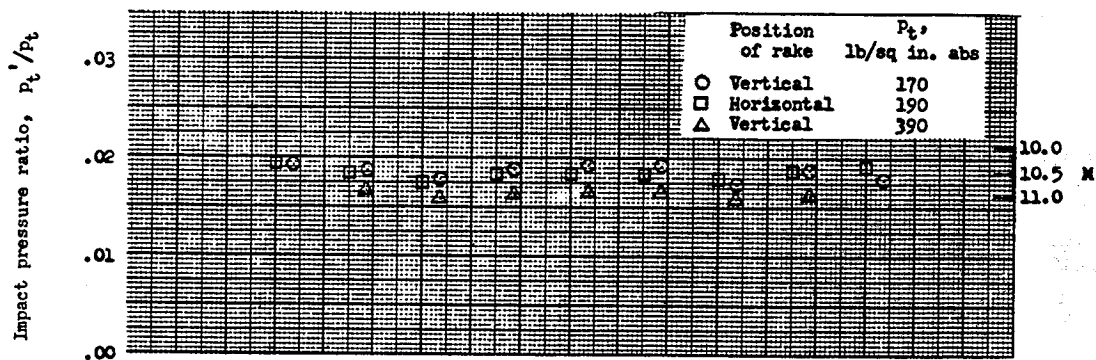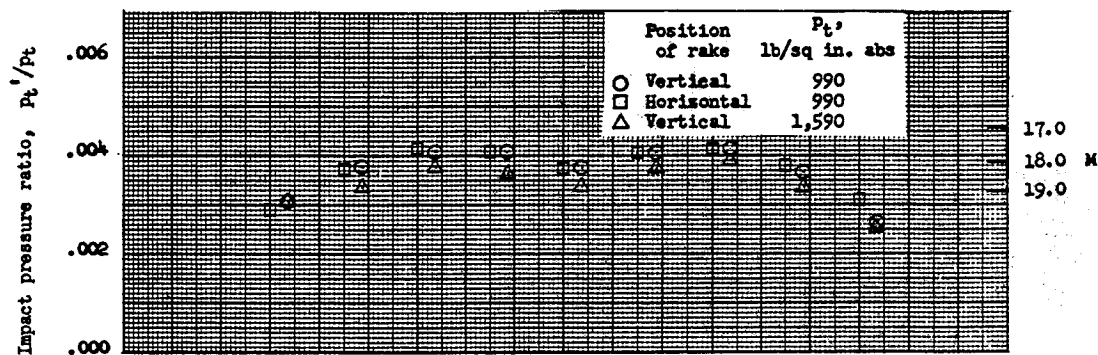
(b) Rake on center line of test section.
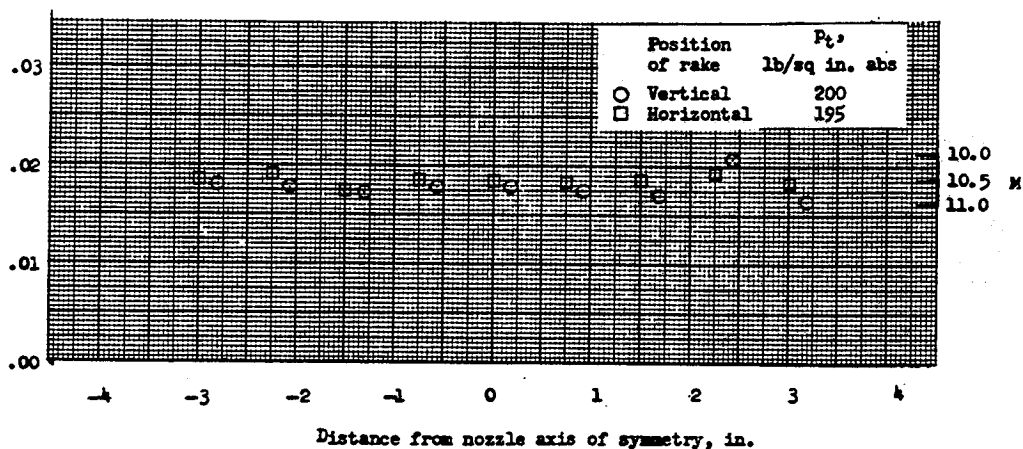
(c) Rake 4 inches downstream of center line of test section.

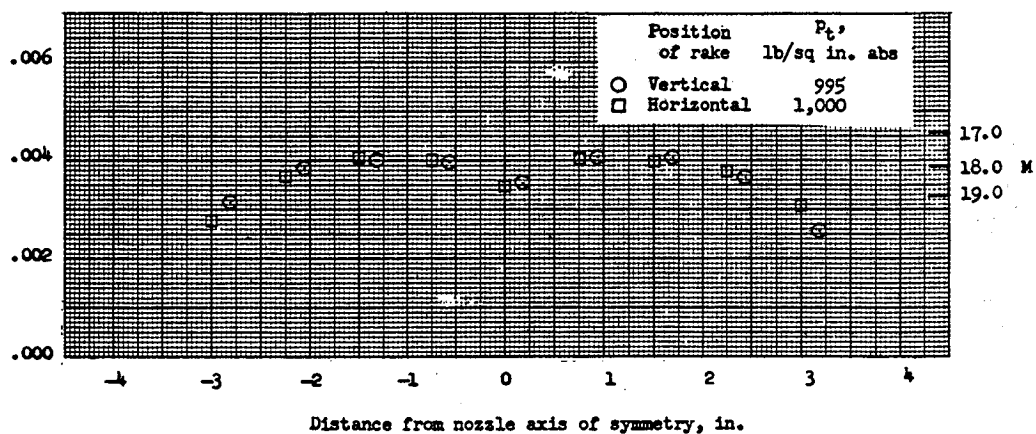Figure 27.- Results of impact-pressure survey in the Mach 10.5 axisymmetric helium nozzle.

L-247

(a) Rake 4 inches upstream of center line of test section.

(b) Rake on center line of test section.

(c) Rake 4 inches downstream of center line of test section.

Figure 28.- Results of impact-pressure survey in the Mach 18 axisymmetric helium nozzle.